Università degli Studi di Firenze
Scuola di Scienze Matematiche Fisiche e Naturali
Corso di Laurea Magistrale in Scienze Fisiche e Astrofisiche
Fisica Nucleare e Subnucleare

Fermi National Accelerator Laboratory
LArIAT - Neutrino Division

Study of charged particles interaction processes on Ar in the 0.2 - 2.0 GeV energy range through combined information from ionization free charge and scintillation light

Supervisor:
Flavio Cavanna

Co-supervisor:
Oscar Adriani

Candidate:
Irene Nutini

Firenze, 21 Luglio 2015

Contents

Introduction

The Thesis paper will report an overview on the commissioning and MC studies for the LArIAT experiment.

The LArIAT experiment is part of the LArTPC Neutrino program at Fermilab. Main purpose of the experiment is to perform a precise "calibration" of the Liquid Argon TPC detector. The main goal is the optimization of the offline algorithms for Particle IDentification and calorimetric reconstruction for Liquid Argon detector technology, both TPC wires signals and LAr scintillation light collection. LArIAT experiment aims to study of all the particle types emerging from (ν,Ar) interaction, for neutrino energies E_ν of few GeV, typical of the SBN and LBN programs, by means of charged particles of defined species (mainly pions $\pi^\pm$, protons p, muons $\mu^\pm$, electrons $e^\pm$, kaons $K^\pm$...), momentum (0.2 - 2.0 GeV/c range) and sign provided by a dedicated TestBeam line.

One of the goals of the LArIAT experiment will be the experimental measurement of charged pion cross section on Ar in the 0.2 to 2.0 GeV energy range. Actually there aren't any experimental measurements for pions Ar in this energy range. Current MC simulation codes, like Geant4, use interaction models for Ar based on extrapolations from data with lighter or heavier elements. The goal of a dedicated pion run with LArIAT is to develop pion identification algorithms based on their interaction modes in Argon and to exploit direct and precise measurement of the pion-nucleus cross-sections to reduce the uncertainty on the hadron interaction models adapted in MC simulations for Ar target.

A study of charged pion interactions in Liquid Argon target and the development of a routine to evaluate the total interaction cross section, that could be later applied to real data from the TPC, will be the first and software oriented topic of my Thesis. From a Monte Carlo "thin target" simulation, I will provide a prediction of the total hadronic interaction (π,Ar) cross section. Since the LArIAT TPC active volume consists in a "thick target" for charged pion interactions we will need to develop a new analysis method to estimate the charged pion cross section on Ar from the experimental data that will be collected in LArIAT.

Another goal for the LArIAT experiment will be the development, test and characterization of dedicated devices for LAr scintillation light collection. LAr scintillation light is now used only for triggering purposes; the aim is to extend its use for calorimetric energy reconstruction to improve the energy resolution of this detector technology. Actually two different light collection systems have been implemented in LArIAT cryostat, two PMTs and three SiPM readout boards.

The development and test of LAr light collection optical devices, especially dedicated cold front-end electronics for SiPM devices, for LArIAT will be the second and hardware oriented topic of my Thesis.

Chapter 1: Overview on Liquid Argon Time Projection Chambers for Neutrino Physics. The Liquid Argon Time Projection Chamber (LArTPC) detectors are the most promising technology to detect neutrino interactions due to the image-like quality data they provide. LArTPCs are the detector technology chosen for the future Large Neutrino Experiment to be built in the US. Liquid Argon detectors offer the opportunity

to detect neutrinos which will complement most other large detectors set to discover mostly anti-neutrinosì. The technology is still in ongoing development, especially in terms of scintillation light.

Chapter 2: Brief overview on LArIAT experiment. The LArIAT experiment is hosted in the Fermilab TestBeam Facility. A tertiary beam of charged particles, mainly pions and protons, with momentum tunable between 0.2 and 2.0 GeV/c, is driven to the LArTPC, which is deployed in a cryostat filled with LAr (90 K). The LArIAT TPC is briefly described as well as the light collection system and the DAQ and trigger system for data acquisition. The LArIAT experiment has been fully operational at the Fermilab Test Beam Facility since April 30, 2015. The 1st Run has ended on July 4th, 2015.

Chapter 3: The expected (charged pion,Ar) cross section dependence on energy, obtained with two MC generators (Geant4 and Genie) for thin Ar targets has been computed and compared with available experimental data for different target materials. The LArIAT LAr TPC volume represents a "thick target" for pion interaction. A new method for off-line data analysis is being developed, the "Sliced TPC" method, for the experimental pion cross section reconstruction, based on the specific features of the LArTPC.

Chapter 4: First data collection from LArIAT experiment and planned data analysis. TPC event imaging: A 2-D image of the ionization tracks in the event is obtained for each projection TPC wire plane; it is useful for studying the topologies of the interactions of incoming particles with Argon nuclei. Some pion interaction events collected in the TPC are reported. TPC event reconstruction in LArIATSoft dedicated framework: to achieve a 3-D reconstruction (track and energy deposit) of the event it is necessary to match the pulses which have the same drift time in the two views. The aim is to achieve a complete and precise event reconstruction of identified particles crossing or experiencing an interaction in the LArTPC active volume.

Chapter 5: Description of LArIAT ongoing development with SiPM devices for LAr scintillation light collection. The LArIAT light collection system is based on the concept developed for Dark Matter search with LAr detectors. The Ar VUV scintillation light is wavelength-shifted into visible and reflected up to collection by an array of PMTs and SiPMs immersed in LAr. The SiPM readout boards have been custom-designed for LArIAT. First preliminary characterization of the signal from the SiPM with and without a (cold) Pre-Amplifier stage is reported.

Chapter 1

Liquid Argon Detectors for neutrino physics

1.1 Neutrino research

Neutrinos are the least understood constituents of matter; but our universe is for a great part permeated with them.
They are nearly massless, neutral fermions. The most important of their features is that they rarely interact with matter; we could consider them as ghostly particles.

The basic properties of neutrinos, no electric charge and little mass, were at first hypotized by W.Pauli in 1930 to explain the apparent loss of energy in the process of radioactive beta-decay.[1]
E. Fermi in 1934 elaborated the theory of beta decay and gave the particle its name. An electron-neutrino is emitted with a positron in positive beta decay, while an electron-antineutrino is emitted with an electron in negative beta decay.[2]

Despite such predictions, neutrinos were not detected experimentally for more than 20 years, due to the weakness of their interactions with matter.

The first evidence of neutrino was given in 1956 from the Cowan and Reines experiment [3], where they discovered the electron-antineutrino (ν_e) via the reaction:

$$\overline{\nu_e} + p \longrightarrow e^+ + n$$

Neutrinos are building blocks of the Standard Model. Like quarks and charged leptons, neutrinos are spin-1/2 fermions, but they are electrically neutral and they interact with other particles only through weak interaction mediated by the $W^{\pm}$ charged bosons and the Z^0 neutral boson.
There are three neutrino "flavours": ν_e, ν_μ, ν_τ. Each of these is coupled via the weak interaction to the charged lepton of the same flavour:e, μ,τ.
Identification of ν_μ as distinct from ν_e was accomplished in 1962 by L.Lederman, M.Schwartz and J.Steinberger at Brookhaven National Laboratories. [4]
The discovery of the tau neutrino ν_τ was announced in 2000 by the DONUT experiment, at Fermilab, which was built to specifically detect that kind of neutrino. [5]

1.1.1 Neutrino sources

Neutrinos are generated in weak interactions and decays. Neutrinos can be produced by "natural" or "artificial" sources.

- Natural sources:
  - Neutrinos from nuclear fusion processes in the Sun [Solar neutrinos] (ν_e electron type, from few KeV to 15 MeV)
  - Neutrinos from supernova explosions [SuperNova neutrinos] (10 MeV - 100 MeV)
  - Neutrinos in air showers initiated by primary cosmic ray nuclei, mainly from π, K and μ decay [Atmospheric neutrinos] (ν_e, ν_μ 100 MeV -100 GeV)
- Artificial sources:
  - Reactor neutrinos from nuclear fission process, β decay ($\overline{\nu_e}$, 1 MeV - 10 MeV)
  - Beam dump neutrinos (ν_e, ν_μ, $\overline{\nu_\mu}$ 10 MeV - 50 MeV)
  - Accelerator neutrinos (mainly ν_μ ($\overline{\nu_\mu}$), 1 GeV - 100GeV)

Artificial ν-sources allow to limit systematics on the fluxes; an extended program with long-baseline neutrino beams (LBL) in Europe, US and Japan are active or are being launched.
A new generation short baseline program (SBL) has been recently approved at Fermilab, US.
Neutrino beams are created in weak decays of short-lived hadrons.
In this case a proton beam is extracted from an accelerator complex and the protons are smashed into a target, e.g. graphite, and secondary, short-lived particles are produced, such as pions and kaons. These particles travel a relatively short distance (few hundreds meters) through a "decay pipe". A good fraction of them decays producing neutrinos that continue on in the same direction, forming a neutrino beam, whereas all the other particles such as the remaining protons and undecayed mesons are absorbed by large iron or concrete blocks. Of the three known neutrino types, a beam produced in this manner contains mostly muon neutrinos.

The long-baseline neutrino beams that are in use or planned, which mostly provide ν_μ beams, are: [8]

- J-PARC Neutrino Facility in Japan, from Tokai to Kamioka, 295 km away, with off-axis beam configuration where the centre of the neutrino beam direction underground is shifted by a few degrees with respect to Super-Kamiokande detector (T2K experiment).
- CNGS ("CERN Neutrinos to Gran Sasso") from CERN to the Gran Sasso National Laboratory (LNGS), 732 km away (OPERA and ICARUS experiments).
- NuMI ("Neutrinos at the Main Injector") from Fermilab, IL, to Northern Minnesota, 735 km away (NOvA, MINOS experiments) (See Fig.1.1)[6]
- LBNF (" Long-Baseline Neutrino Facility "), from Fermilab, IL, to Sanford, South Dakota, 1300 km away (DUNE experiment)[7]. (Planned)

One of the short-baseline neutrino beams actually in use is the Booster neutrino beam [9] at Fermilab, which mainly produces ν_μ for short-baseline experiments as MiniBoone and now MicroBoone [26]. A system of three short-baseline detectors on the Booster neutrino beamline is expected by 2017.

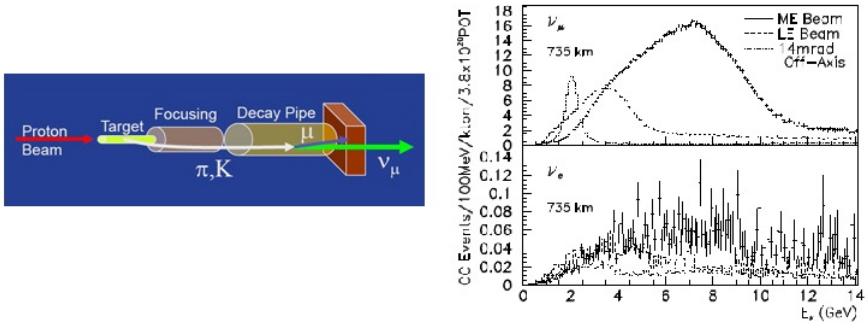

Figure 1.1: NuMI Beam: Schematic representation of neutrino beam production at Fermilab and fluxes of ν_μ and ν_e 735 km away from the NuMI target, both on and off axis for the low and medium energy beam configuration.

1.1.2 Neutrino oscillations

In the last decade, many experiments had found evidence of neutrino flavor oscillation. This implies neutrinos are massive.
The experimental observation of neutrino oscillations, from solar neutrinos firstly, led to the discovery that neutrinos have non-zero mass. So far neutrino mass is manifested through oscillation, while experiments that aim to a direct measurement of it did not reach yet the sufficient sensitivity.
In the Standard Model neutrinos are massless. It appears to be possible to extend the Standard Model making Dirac neutrinos gaining their mass from the linear coupling between the particle and the Higgs boson field, but it still leaves open questions about the strong mass difference among neutrinos and all charged leptons and quarks. Another theory is that neutrinos can have Majorana masses, which mix a particle with its antiparticle, while charged leptons and quarks cannot have them; they would gain their mass by the "see-saw" mechanism which couple light neutrinos to highly massive sterile neutrinos, which do not interact at all with matter.

The idea of neutrino flavor oscillation was first proposed in 1957 by Bruno Pontecorvo and developed by Maki, Nakagawa, and Sakata in 1962.
A neutrino can spontaneously change from one flavor to another; this phenomenon could happen because neutrinos of definite flavor (ν_e, ν_μ, ν_τ) are not mass eigenstates, but a coherent superposition of (ν_1, ν_2, ν_3).

$$|\nu_\alpha\rangle = \Sigma_{i=1}^{3} U_{\alpha i} |\nu_i\rangle \tag{1.1}$$

α=e, μ, τ.
The Pontecorvo–Maki–Nakagawa–Sakata matrix (PMNS matrix) or leptonic mixing matrix U is made by the coefficients which express ν_e, ν_μ, ν_τ in terms of ν_1, ν_2, ν_3.
When the three neutrino theory is considered, the unitary matrix U is 3 × 3. See Eqs.1.2 and 1.3.

$$U = R_{23} R_{13}(\delta) R_{12} \tag{1.2}$$

$$R_{12} = \begin{bmatrix} cos\theta_{12} & sin\theta_{12} & 0 \\ -sin\theta_{12} & cos\theta_{12} & 0 \\ 0 & 0 & 1 \end{bmatrix}, R_{13} = \begin{bmatrix} cos\theta_{13} & 0 & sin\theta_{13} \\ 0 & exp(i\delta) & 0 \\ -sin\theta_{13} & 0 & cos\theta_{13} \end{bmatrix}, R_{23} = \begin{bmatrix} 1 & 0 & 0 \\ 0 & cos\theta_{23} & sin\theta_{23} \\ 0 & -sin\theta_{23} & cos\theta_{23} \end{bmatrix} \tag{1.3}$$

where θ_{ij} i,j=1,2,3 are the mixing angles between mass eigenstates and δ is a phase angle.
While the flavor states (ν_e, ν_μ, ν_τ) are the eigentstates of the weak interaction hamiltonian, the mass states (ν_1, ν_2, ν_3) are the eigenstates of free propagation and thus can be described by plane wave solutions of the form:

$$|\nu_\alpha, t\rangle = e^{(i\vec{p}.\vec{x})}\Sigma_{i=1}^{3}U_{\alpha i}e^{(-iE_i t)}\,|\nu_i\rangle \tag{1.4}$$

where E_i=$\sqrt{m_i^2+p_i^2}$ (c=1) are different for the three mass eigenstates.
For a physical neutrino (weak eigentstate) produced with flavor α at t=0 is then possible to define the probability of oscillation to flavor β after time t:

$$\begin{aligned} P_{\alpha\to\beta} = |\,\langle\nu_\beta|\,|\nu_\alpha, t\rangle\,|^2 = \\ \delta_{\alpha\beta} - 4\Sigma_{i>j}Re(U_{\alpha i}^* U_{\beta i} U_{\alpha j} U_{\beta j}^*)sin^2(\frac{\Delta m_{ij}^2 L}{4E})+ \\ +2\Sigma_{i>j}Im(U_{\alpha i}^* U_{\beta i} U_{\alpha j} U_{\beta j}^*)sin(\frac{\Delta m_{ij}^2 L}{2E}) \end{aligned} \tag{1.5}$$

where $\Delta m_{ij}^2 \equiv m_i^2 - m_j^2$ is the quadratic mass difference, L is the oscillation distance from the production point and E is the neutrino energy.

If we consider for simplicity the case of two neutrino mixing, the mixing matrix U becomes a 2×2 matrix depending only on one mixing angle:

$$U = \begin{pmatrix} cos\theta & sin\theta \\ -sin\theta & cos\theta \end{pmatrix} \tag{1.6}$$

In this case the probability of a neutrino changing its flavor from α to β at time t is (in natural units):

$$P_{\alpha\to\beta,\alpha\neq\beta} = sin^2(2\theta)sin^2(\frac{\Delta m^2 L}{4E}) \tag{1.7}$$

To a first approximation a 2×2 scheme was found to represent well the detected oscillation phenomenon observed separately for Solar Neutrinos (KamLAND, SNO, Gallex/SAGE, Borexino experiments) with characteristic L/E $\approx$ 15000 Km/GeV:

$$\begin{aligned} \Delta m_{21}^2 = \Delta m_{sol}^2 = 7.53 \pm 0.18 \times 10^{-5} eV^2 \\ sin^2(2\theta_{12}) = 0.3 \end{aligned} \tag{1.8}$$

and for the Atmospheric Neutrinos (Super-K, MINOS, T2K; NOvA) with characteristic L/E $\approx$ 500 Km/GeV:

$$\begin{aligned} \Delta m_{32}^2 \approx \Delta m_{31}^2 = \Delta m_{atm}^2 = 2.44 \pm 0.06 \times 10^{-3} eV^2 \\ sin^2(2\theta_{23}) > 0.92, \theta_{23} = \theta_{atm} = 45.0 \pm 7.1^\circ \end{aligned} \tag{1.9}$$

The Atmospheric Neutrino result was definitely confirmed with LBL accelerator neutrinos by the K2K experiment (KEK to Kamioka-SuperKamiokande, L=250 km, $<E_\nu>$ $\approx$ 1 GeV).
Recently, with a second generation of neutrino oscillation experiments carried out using artificially produced neutrinos at reactors, the last, long awaited measurement of the remaining set of oscillation parameters in the 3×3 general formalism has been achieved (Daya Bay in China, Double Chooz in France, RENO in Corea, NOvA in Us):

$$\begin{aligned} |\,\Delta m_{ee}^2\,| = 2.44 \pm 0.11 \times 10^{-3} eV^2 \\ \approx \Delta m_{23}^2 (\text{if direct mass hierarchy}) \\ sin^2(2\theta_{13}) = 0.084 \pm 0.005 (\text{Latest Daya Bay results, [10]}) \end{aligned} \tag{1.10}$$

The neutrino flavor oscillation scheme is still not completed. Two fundamental questions remain open:

1. is the δ phase different from zero?

2. what is the neutrino mass hierarchy? direct or inverted?

A non-zero value of the δ phase allows for CP violation, occuring also for charged leptons; this would led to an explanation of matter-antimatter asymmetry in the Universe.
The neutrino mass hierarchy question is directly connected to the knowledge of the main mass component for each flavor neutrino. Since we have only quadratic values of mass differences from neutrino flavor oscillation experiments, in this very moment two possible mass hierarchies (direct and inverted) could be possible, as shown in Fig.1.2.
To answer these questions a number of new LBL experiments were recently activated (T2K in Japan, Nova in US) or just approved for construction (DUNE in US).

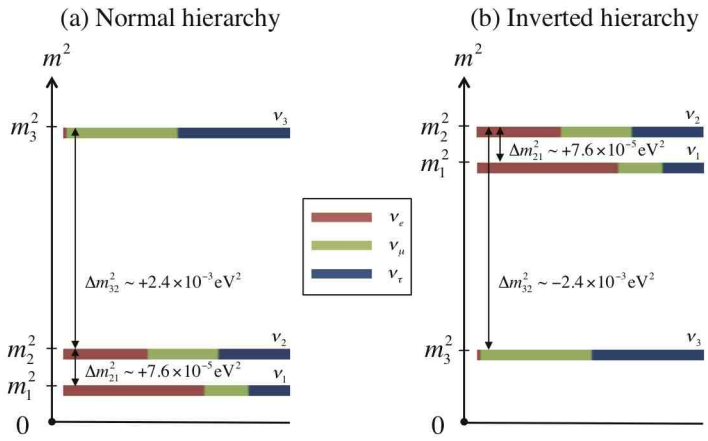

Figure 1.2: Neutrino mass hierarchy: direct or inverted.

Simultaneously with neutrino flavor oscillation studies, another research branch on neutrinos exists. It deals with Sterile Neutrinos.
Sterile neutrinos (inert neutrinos) are hypothetical particles that do not interact via any of the fundamental interactions of the Standard Model except gravity. The term sterile neutrino is used to distinguish them from the known active flavor eigenstates neutrinos which are present in the Standard Model.
Sterile neutrinos arise in several extensions of the Standard Model to accommodate massive (light) neutrinos.
Neutrino masses so suggest the existence of right-handed degrees of freedom, the sterile neutrinos, which would have very large Majorana masses. In particular the recently developed model considers 3 singlet states N_1, N_2 and N_3 associated with the 3 active neutrinos ν_e, ν_μ, ν_τ.
It is possible to introduce an oscillation probability between sterile and active neutrino states.
Both LSND (Liquid Scintillator Neutrino Detector) [11] and MiniBooNE [9] neutrino experiments, which aim to effect sensitive searches for neutrino oscillations in the mass region with $\Delta m^2 \approx 1\ eV^2$, see indications of electron neutrino/antineutrino appearance from muon neutrino/antineutrino. The LSND experiment observes excesses of events for both of them, corresponding to oscillation probabilities higher than the one expected

for the Δm^2 value from only the light active neutrinos mixing. These discrepancies could not be easily related to flavor oscillation and leave the door open to models with several sterile neutrinos. Investigations of high Δm^2 oscillations currently form one of the most active areas of neutrino physics and many new experiments are being mounted or considered, e.g short baseline program at Fermilab (three detectors along neutrino beam; MicroBooNE experiment [27] is actually running).

1.1.3 Neutrino interactions and detection

Neutrinos can only experience weak interactions.

Neutrino weak interactions can proceed through charged and neutral current interactions, with nuclei and atomic electrons at lower energies, and with p, n in nuclei and with quark in nucleons at higher energies.
For high energy neutrinos the charged current interaction on p,n (q, $\overline{q}$) in nuclei (nucleons) is usually decomposed in three channels:

$$\begin{aligned} \sigma_{tot} = \sigma_{QEL} + \sigma_{RES} + \sigma_{DIS} = \\ = \sigma_{0\pi} + \sigma_{1\pi} + \sigma_{n\pi} \end{aligned} \tag{1.11}$$

The first term in Eq.1.11, σ_{QEL}, refers to Quasi-Elastic Scattering, described with a Current-Current V-A Lagrangian:

$$\nu_l + n \longrightarrow l^- + p \tag{1.12}$$

The second term in Eq.1.11, σ_{RES}, is the Resonance Excitation Channel:

$$\nu_l + N \longrightarrow l + \Delta/N^* \longrightarrow l + \pi + N' \tag{1.13}$$

where N is the ground-state nucleon and Δ (and N^*) are excited states decaying with π production.
The Δ resonance is considered as an "excited nucleon" N; its rest mass is 1232 MeV, with S=0, I=$\frac{3}{2}$, $J^P = \frac{3}{2}^+$. It quickly decays via strong interaction in a nucleon and a pion ($\Delta \longrightarrow$ N π, τ = 5 x 10^{-24} s).
There are four $\Delta(1232)$ resonance particles: Δ^{++} (uuu), Δ^+ (uud) , Δ^0 (udd) , Δ^- (ddd). Each of them could decay in a charged or neutral pion and in a proton or neutron.

$$\begin{aligned} \Delta^{++} &\longrightarrow p + \pi^+ \\ \Delta^{+} &\longrightarrow n + \pi^+ \\ \Delta^{+} &\longrightarrow p + \pi^0 \\ \Delta^{0} &\longrightarrow n + \pi^0 \\ \Delta^{0} &\longrightarrow p + \pi^- \\ \Delta^{-} &\longrightarrow n + \pi^- \end{aligned}$$

As we can see in Fig.1.3, The QE scattering channel is the main process in the region around 1 GeV of neutrino energy. The Resonance Excitation channel appears in the "Intermediate" energy range (0.5-5 GeV); in this region nuclear effects have a non negligible role. These effects include motion of the target nucleon N in the parent nucleus, Pauli blocking and nucleon binding effects as well as multi nucleons correlations,

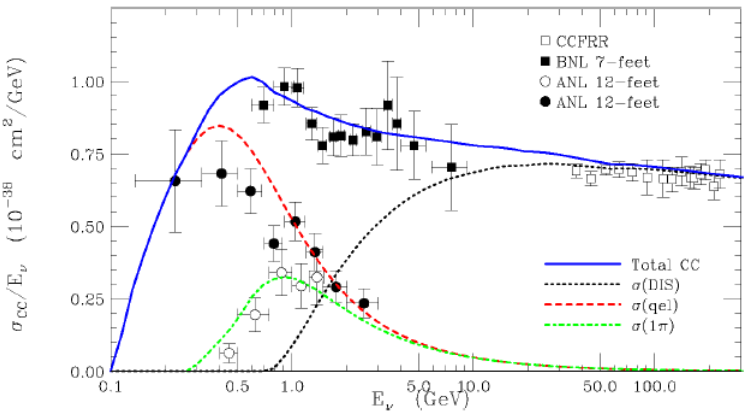

Figure 1.3: Charged current ν_μ cross section calculation.[12]

shadowing and final state interactions (FSI) in nuclear matter. This cause a suppression of the ν-N cross section and an increase of the systematic error due to the model choosen for FSI. So an adequate modeling of nuclear effects is needed to have a better knowledge of RES ν interaction channel.

The third term in Eq.1.11, σ_{DIS}, correspond to the Deep Inelastic Interaction modes on quarks, described with a V-A Lagrangian with the massive $W^{\pm}$ propagator:

$$\nu_l + N \longrightarrow l + X \tag{1.14}$$

The outgoing hadron X is usually a pion, coupled with a charged lepton; the DIS process starts around 500 MeV neutrino energy (necessary for pion production) and its cross section increases linearly with neutrino energy E_ν.

However, neutrinos have very small interaction cross sections with medium constituents, see Eq.1.15:

$$\begin{aligned} \sigma(\nu A)[1MeV] &\approx 10^{-44} cm^2, \text{Low energy neutrinos, scattering on atoms A} \\ \sigma(\nu N)[1GeV] &\approx 10^{-38} cm^2, \text{QE and RES channels, scattering on nucleons N} \\ \sigma(\nu q)[10GeV] &\approx 10^{-37} cm^2, \text{DIS channel, scattering on quarks q} \end{aligned} \tag{1.15}$$

Neutrino detection is always indirect; they can be detected in the weak interactions they experience with nuclei, nucleons or quarks depending on energy.
So to have measurable interaction rates, high neutrino fluxes, massive detectors and long exposure time are necessary.
For example, for MicroBooNE experiment on Booster neutrino beamline: 60 ton (60 m^3) Liquid Argon target on one year exposure time (effective exposure to neutrino flux: 4 months) to a neutrino flux with $<E_\nu>$ = 1 GeV, the number of expected neutrino interactions N_{int} on target nucleons, especially neutrons:

$$\nu + n \longrightarrow p + \mu$$

is calculated in Eq.1.16.

$$N_{int} = \sigma \Delta t n \Phi \approx 2 \times 10^4 \tag{1.16}$$

σ is the interaction cross section per nucleon for $<E_\nu>$ of neutrino beam, Φ is the neutrino flux = 1.2 $\times$ 10^4 $\frac{\nu}{cm^2 s}$, Δt is the exposure time ($\approx 10^7$ s), n is the number

of scattering centers in the target T ($n = \frac{NM_T N_A}{A_T}$, where M_T and A_T are the effective mass ad the nuclear mass of the target and N is the number of neutrons, for LAr in MicroBooNE: ρ_T = 1.4 gcm^{-3} and V_T=60 m^3, M_T= ρ_T V_T, A=40, N=22).

The detectors collect signals from the detectable particles (charged particles, decay products of excited nuclei or atoms) that are produced by the neutrino collisions with the constituents of the target material.
Several detector technologies have been used depending on:

- Neutrino energy range
- Physics goals
- Different neutrino sources (underground experiments for solar and atmospheric neutrinos to reduce background, surface experiments for reactor and accelerator neutrinos).

In general neutrino detectors are based on collection of ionization charge (bubble chambers, time projetion chambers..) or detection of emitted light, either scintillation or Cherenkov (e.g. Super-K), in all cases produced by the charged particles that comes out from a neutrino interaction with the constituents of the medium.

1.2 Liquid Argon Time projection chambers for neutrino detection

Bubble-chamber experiments played a key role in probing the properties of ν-interactions. The Liquid Argon Time Projection Chambers (LArTPC) technology, first proposed by C.Rubbia in 1977 with ICARUS project [14], is considered the modern evolution of bubble-camber concept, with the additional features of three-dimensional event reconstruction, high-resolution calorimetry, active mass coincident with detector sensitive mass and can intrinsically supply a trigger signal (self-triggering) by means of the scintillation light produced in the liquid noble gas. This technology is ideal to perform ν-studies in a broad energy range, from MeV up to few GeV, with high event reconstruction efficiency, thanks to the capability of particle identification and detailed reconstruction of different interaction topologies.
In Figure 1.4 is shown a neutrino interaction event, producing a proton, a pion and a muon, as seen in a bubble chamber and in a LArTPC.

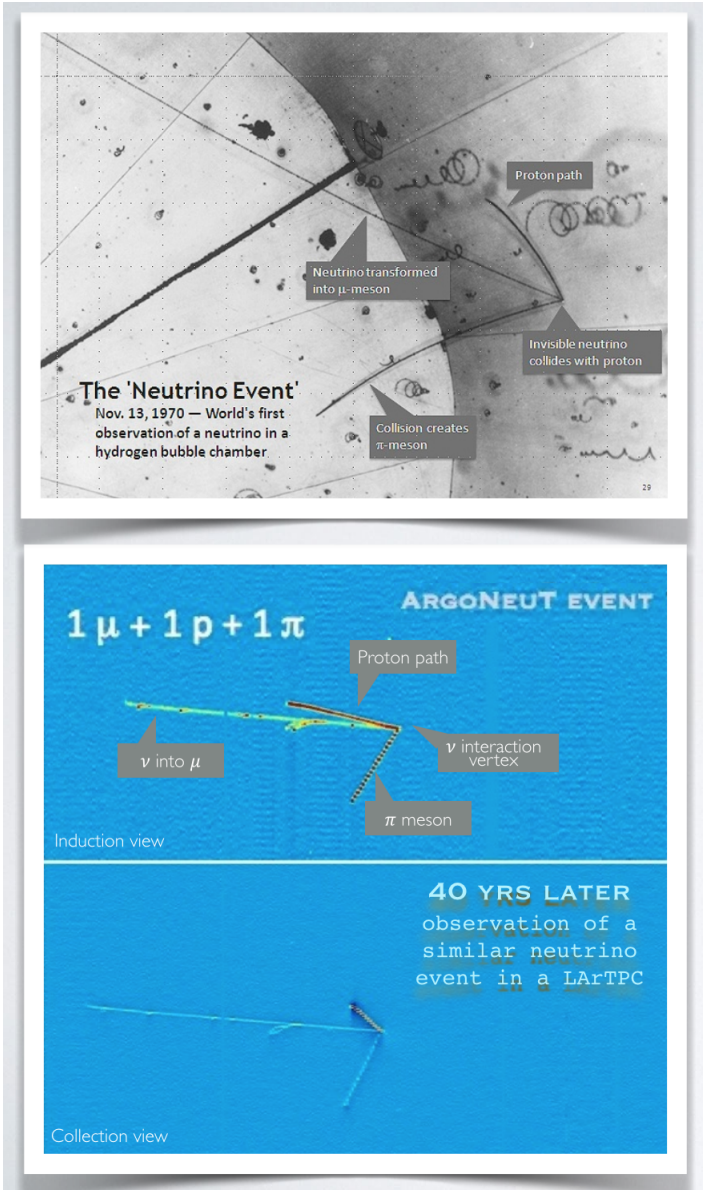

Figure 1.4: Neutrino charged current interaction - Resonance excitation channel- as seen in Argonne 12-feet Bubble Chamber in 1970 [13] and in ArgoNeuT LArTPC [23].

1.2.1 TPC: principles of operation

Ionization detectors have been frequently used in Experimental Particle Physics for the possibility to reconstruct particle trajectories and to have calorimetric information with a non-destructive technique.
Among them the most used have been the proportional counters, as Multi Wire Proportional Chambers (MWPC) and Drift Chambers, in which the charge collected after an ionizing process is directly proportional to the energy deposit of the primary particle that crosses the active volume or interacts there.

The Time Projection Chamber (TPC) makes use of ideas from both the MWPC and the Drift Chamber and it is actually used for charged particles 3-D tracking in a large number of particle and nuclear physics experiments.
A TPC consists of a gas-filled detection volume in an electric field with a position-sensitive electron collection system.

The TPC concept was first introduced by David Nygren in the late 1970s.[15] Its first application was in the PEP-4 detector, which studied 29 GeV electron-positron collisions at the PEP storage ring at SLAC.
The original design was a cylindrical chamber filled with methane gas, with MWPC as endplates and an intermediate screen to establish a uniform electric field parallel to the beam. A magnetic field was applied along the length of the cylinder, parallel to the electric field, in order to minimize the diffusion of the electrons coming from the ionization of the gas. Charged particles penetrating the active volume experience magnetic deflection and leave ionization tracks in the gas. Ionization electrons drift toward the positive end-caps, so the entire image of each trajectory can be reconstructed if the information from the end-caps is read out during the drift time. (See Fig.1.5 and 1.6)

The TPC is essentially a 3-D tracking detector capable of providing tracks reconstruction along with information on energy loss of the particle.
Charged particles crossing the sensitive volume (cylindrical chamber filled with a gas) produce free electrons via ionization; an uniform electric field is applied and it drifts the electrons towards the end-cap surfaces where they are detected by anode wires as in a MWPC. In this way we have the 2-D position of a space point projected onto the end-cap plane. One coordinate corresponds to the firing anode wire while the second is obtained from the signals induced on the segmented cathode pads along the anode wire.
The third coordinate, along the cylinder axis, is given by the drift time of the ionization electrons, from that the detector has been given the name of Time Projection Chamber, TPC. The third coordinate represents the distance from the sensing wire to the origin of the ionization electron. See Eq.1.17.

$$z = \int_{t_0}^{t_1} \overrightarrow{v}_{drift,e}(t)dt \qquad \overrightarrow{v}_{drift,e} = \mu_e \overrightarrow{E} \tag{1.17}$$

in which z is the coordinate along the TPC axis, parallel to the incident beam in this case, $\overrightarrow{v}_{drift,e}(t)$ is the electron drift velocity, μ_e is the electron mobility, t_0 is the arrival time of the primary particle - trigger time- and t_1 is the time at which the electron pulse appears at the anode.

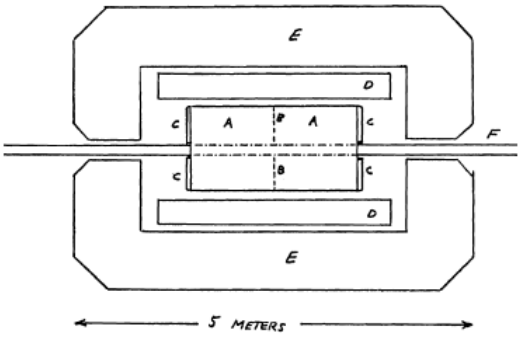

A. Methane-Filled region ~1 M dia., 2 M Length
B. Screen or Foil to establish $\vec{E}$ Field
C. End-cap detectors
D. Superconducting Solenoid (3.3 T)
E. Iron return yoke for B Field
F. Beam Vacuum Pipe.
Not shown are trigger scintillators, compensators Luminosity monitors, etc.

FIGURE 2 TPC Detector Schematic

Figure 1.5: Nygren's schematic design for a TPC for PEP for charged particles identification.[15]

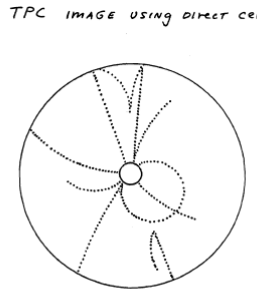

TPC IMAGE USING DIRECT CELL DATA.

Figure 3 "Typical event" with 12 charged tracks, shown in 2-dimensional projection. Some event tracks leave through the end caps.

Figure 1.6: A "typical" event in Nygren's TPC (2 dimensional projection, looking along the beam pipe).[15]

A schematic view of a cylindrical TPC is reported in Fig.1.7.
Chambers are usually operated in a region where the drift velocity is independent from $\vec{E}$. (Saturation region) So z=v_{drift} Δt, if the drift velocity can be assumed constant ($\Delta t = t_1$-t_0).

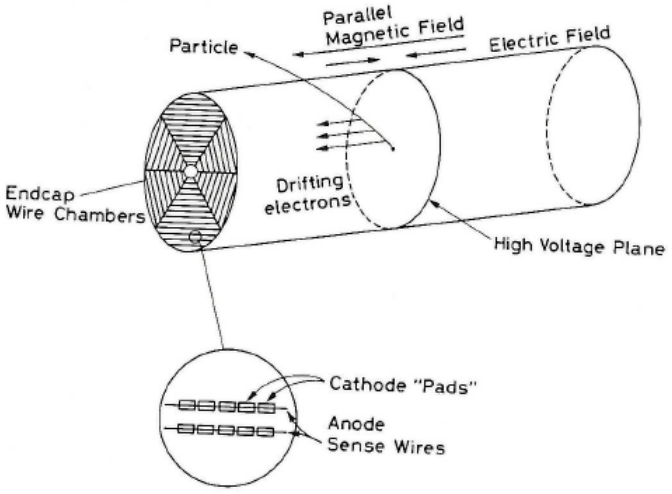

Figure 1.7: Schematic diagram of a Time Projection Chamber.[16](Fig.6.17 p.152)

The purity of the gas plays also an important role in electrons collection at the anode wires, since electrons won't be captured by electronegative impurities as they drift to the anodes. This effect is described in Sec.1.2.2.

Eventually the charge collected at the end-caps is proportional to the energy loss of the particle in the medium, so the signal amplitudes from the anodes also provide information on th $\frac{dE}{dx}$ of the particle. If the particle initial momentum/kinetic energy is known, this information can be used to identify the particle (PID: Particle IDentification with TPCs).

Because of the very large amount of data/electrons produced by each event, the measure of the drift time and signal charge need fast electronics capable of responding of more than one hit: Waveform Recorders or Flash ADCs directly coupled to the sense wires are usually used.

This kind of TPCs have been usually used in Nuclear physics experiments. Actually gas filled TPC technology can't be used for Neutrino physics experiments as they are. Huge volumes of Gas would be needed to have a few neutrino interactions, due to the small value of gas density which couples with small neutrino interaction cross section. A new concept of TPC filled with liquid was proposed, to have reasonable target volumes that would contain enough mass - scattering centers- for a neutrino to interact.

1.2.2 Ionization detectors with noble liquids

Using liquids instead of gas as active materials in ionization detectors has many advantages for increasing neutrino interaction statistics and measuring $\frac{dE}{dx}$ or total deposited energy E of secondary charged particles produced.

Liquids density is almost 1000 times greater than gas density; so there is a much higher concentration of active scattering centers for the crossing incident particle.

The specific energy loss $\frac{dE}{dx}$ for charged particles is 1000 times more in liquids than in gas.

$$(\frac{dE}{dx})_{liq} \approx 1000(\frac{dE}{dx})_{gas} \tag{1.18}$$

Moreover, the average energy required to produce an electron-ion pair (W_{e-i}) in liquids is 15-25 eV, less than in gas.
So liquids are expected to have a higher number of ionizations for the same total energy deposit than for gas.
For example: Energy deposit, ΔE = 1 MeV, numbers of pairs produced, N $\geq$ 4 x 10^4 e/ion, $\frac{dN}{N} = \frac{\sigma(E)}{E} = \frac{1}{\sqrt{N}} < 10^{-2}$.

Liquid noble elements (LAr, LXe, LKr) can be used as homogeneous calorimeters, because of their good counting properties.
Noble gas become liquid at low temperatures; so experiments need cryogenic equipment.

The lifetime of carriers τ, especially for electrons τ_e, in liquids is strongly dependent on the concentration of electronegative impurities, that act as scattering and absorption centers, usually referred to an "attachment".
The average lifetime for electrons τ_e is directly proportional to the mean free path, before carriers would be captured by impurities, λ_t which increase for lower impurities concentration K.

$$\tau_e \propto \lambda_t \propto \frac{1}{K} \tag{1.19}$$

So, for having a consistent value of electron mobility, it's necessary to achieve an extremely low level of electronegative impurities, as O_2 (for example: $K_{O_2} \leq 1$ ppb, $K_{N_2} \leq 1$ ppm for hundreds ton LArTPC experiments).

The ion mobility in liquids is lower than for electrons; the induced charge due to the ion motion has a very slow rise time; it can be hardly used electronically and usually it's neglected.
The electrons drift velocities $\overrightarrow{v}_{drift,e}$ are lower in liquids than in gas for the same applied electric field $\overrightarrow{E}$, because of the small electron mobility in liquids, see Eq. 1.17. For example:

$$\overrightarrow{v}_{drift,e} \approx \begin{cases} 1.6\dfrac{mm}{\mu s} & \text{Liquid Argon, } \overrightarrow{E} = 500V/cm \\ 100\dfrac{mm}{\mu s} & \text{Gas Argon, } \overrightarrow{E} = 500V/cm \end{cases}$$

Applying an appropriate electric field $\overrightarrow{E}$ in liquids is important to separate quickly the electrons that recombine with positive ions, that happens because of the high density.

In Table 1.1 the principal properties of Liquid Noble Elements (LAr, LXe, LKr) used as ionization detectors are listed.

	LAr	LXe	LKr
Atomic Number Z	18	36	54
Atomic weight A	40	84	131
Boiling Point Tb (K) @ 1 atm	87.3	120.0	165.0
Density (g/cm3)	1.4	2.4	3.0
Radiation lenght X_0 (cm)	14.0	4.9	2.8
Moliere Radius R_m (cm)	10.0	6.6	5.7
Wi (eV)	23.6	20.5	15.6
μ_e $(m^2/Vs)E$ =10^4 V/m	0.047	0.18	0.22
μ_e $(m^2/Vs)E$ =10^6 V/m	0.004	0.005	0.0025
Fano factor F	0.107	0.057	0.041
dE/dx MIP (MeV/cm)	2.1	3.0	3.8
Scintillation LY (γ/MeV)	40000	25000	42000
Scintillation λ (nm)	128	150	175

Table 1.1: Table of the principal properties of Liquid Noble elements

1.2.3 LArTPC: principles of operation

Among the ideas developed around the use of liquid noble gases for ν experiments, Liquid Argon Time Projection Chamber (LArTPC) technology appears to offer a unique combination of high precision tracking, precise calorimetry and scalability to very large sensitive volumes.

As previously said, LArTPC can be considered as an electronic version of a bubble chamber, continuously sensitive and self-triggering.

Bubble chambers have been widely used in Particle Physics for their capability of 3-D imaging of ionizing events. Bubble chambers can be a target and a detector at the same time for the high density of the liquid. However the slow mechanic process of chamber expansion and imaging on photographic films limits the use speed. The expansion can't be triggered to the precise moment in which the ionization occurs.
An electronic detector, in which the event produces directly electric signals which are extracted, amplified, digitized and recorded, can be triggered and read out online. More complex and sophisticated electronic detectors have gradually substituted the bubble chambers for Elementary particle physics. These detectors (MWPC, Drift Chambers and TPC) have some limits: due to the small density of the gas used as ionizing medium, they can't be targets and detectors at the same time.

So, for detecting rare events like neutrino interactions, the ideal detector is the one that provides detailed informations (spatial resolution, particle identification, 3-D event imaging) typical of bubble chambers and can have simultaneously an electronic readout.

LArTPC technology was first proposed by C.Rubbia at CERN in 1977 [14], leading up to the realization of the first LAr detector of significant size (600 tons) for underground physics application, ICARUS T600 [17] [18] [21]. See Fig.1.9.[1]
Rubbia proposed to extend the TPC concept, which provides informations on the topology of the event, to a liquefied noble gas, as Argon, that could act as a counter too.

(Pure) Liquid Argon appears to be an ideal sensitive medium since it provides high density (useful to enhance ν interaction probability) and excellent ionization and scintillation yields (as shown in Table 1.1); it's safe because it's inert. Liquid Argon is relatively cheap and quite easy to obtain (usually atmospheric Argon, 1% at atmospheric air) and to purify too.
As discussed in Section 1.2.2, a noble liquid element behaves like a dielectric insulator and at a reasonable purity level it has low electron attachment rate, so it permits small diffusion of the carriers, long drift times and it has a high electron mobility.

The LArTPC detector is fully active, homogeneous and isotropic.
The whole Argon volume is placed in an intense and uniform electric field, produced by two facing electrode planes. Charged particles crossing a volume of Liquid Argon produce tracks made by electron-ion pairs. A fraction of these pairs, due to the high electric field intensity, does not recombine and starts to separate moving along the electric field lines. They are transported undistorted by the electric field onto the anode wire-planes. The free electric charge motion induces a current on the wires. Electrons

[1] ICARUS (Imaging Cosmic And Rare Underground Signals) is a physics experiment aimed at studying neutrinos. It was located at the Laboratori Nazionali del Gran Sasso (LNGS). No longer operating, it is being refurbished at CERN for re-use in the same neutrino beam from Fermilab as the MicroBooNE experiment.

have a drift velocity in LAr $v_{drift} \approx 1.6\ \frac{mm}{\mu s}$ for E=300 $\frac{V}{cm}$, which is almost 10^5 times the ion dirft velocity; so the electrons give the main contribution to the current on the wires.
The cathode is a plane metal conductor at a fixed potential (or grounded). The anode consists in a system of parallel wire-planes (N $\geq$2), placed at the end of the drift path, continuously sensing and recording the signals induced by the drifting electrons.
Non-destructive readout of ionization electrons by charge induction allows to detect the signal of electrons crossing subsequent wire-planes with different orientation. With this configuration, each segment of an electron track induces a pulse signal ("hit") on one wire in each plane; in this way it's possible to have several projective views of the same event.
Timing of the pulse -drift time- combined with the drift velocity information determines the drift-coordinate of the "hit".
The starting time (t_0) of the ionization process has to be known.
In Fig.1.8 the schematic LArTPC working principle is shown; in Fig.1.9 and Fig.1.10 it is represented the LArTPC of ICARUS experiment and a collected event - wire waveforms and 2-D imaging - from the same experiment.

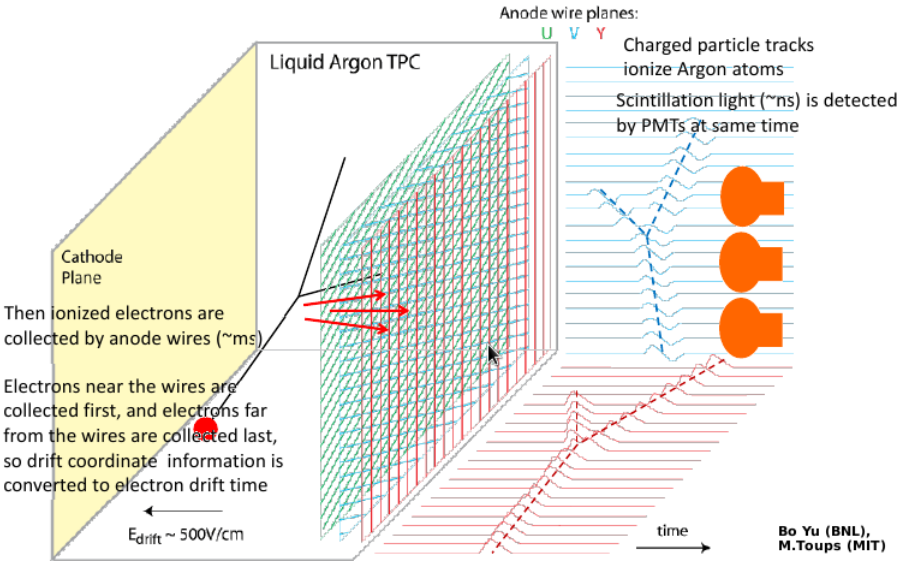

Figure 1.8: LArTPC schematic working principle. Electrons drift along horizontal axis. Induction and collection plane wires are perpendicular to the drift direction.

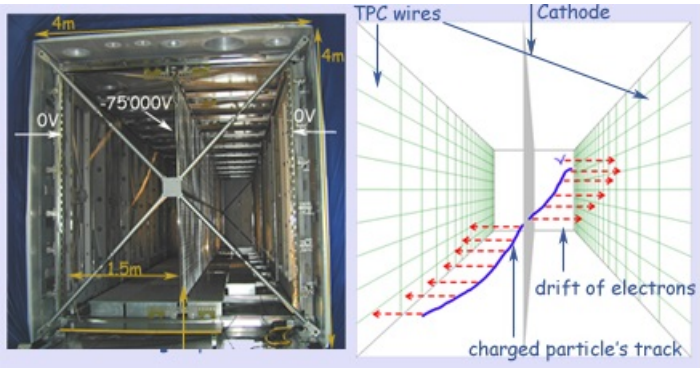

Figure 1.9: Schematic representation of a single module of the ICARUS LArTPC detector and its functionality. The ICARUS detector is composed by two semi-independent, symmetric, filled with liquid argon modules. The read-out chambers (two TPC for each half-vessel) are mounted on the internal walls with the cathode at the centre, to maximize the LAr sensitive volume (corresponding to about 480 ton in mass). The read-out chamber scheme consists of three parallel planes of wires (horizontal, +60 and -60 degrees).[19]

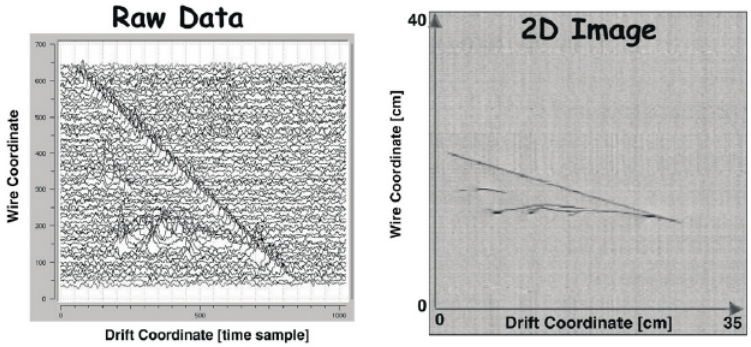

Figure 1.10: (left) Display of digitised waveforms recorded from a number of induction wires detecting an event and (right) the event image after gray-level coding of the waveform pulse-height.[20].

In Liquid Argon no charge multiplication occurs. So the collected charge corresponds directly to the amount of charge produced by ionization and that drifts from the production point to the readout electrode.
Since there is no charge multiplication in the medium, the signal pulse amplitude on each wire is proportional to the relatively small amount of charge in each track segment, collected for each TPC wire.
The disadvantage is that the charge that has to be revealed is very small (e.g. ≈ 8000 electrons for 1 mm MIP particle track in LAr); very low noise cold electronics is needed to be sensitive to the effective primary ionized charge on wires signals. The advantage is that a "non-destructive" read-out is possible to achieve a multi-dimensional readout. Drifting electrons can be used many times for producing induction signals on several readout planes, which should be transparent to their passage, placed before the collection wire plane.

Liquid Argon purity plays a key role to allow ionization electrons to drift over long distances.
Extremely high purity means a very low level of electronegative molecules concentration, like O_2 and hydrocarbons (≤ 1 ppb of O_2 concentration equivalent). This purity level is required for LArTPC experiments, to ensure that the electrons produced by ionizing tracks won't be captured by the electronegative impurities in LAr while drifting from the production point to the collection electrode.

One interesting feature of a LArTPC detector is that it can be self-triggering, so it can provide t_0 by itself. This is obtained exploiting the scintillation light produced by Argon atoms that are excited by crossing charged particles. This topic would be discussed in Ch.2 1.3.

LArTPC technology therefore allows a 3-D space point reconstruction and precise calorimetric measurements.
This kind of technology provides good resolution both for angular reconstruction (tracking) both for the energy (calorimetry).

The LArTPC spatial resolution in interaction vertex position and track direction determination depends on the dimensions of the 3-d pixel and on carriers lateral diffusion. The 3-D pixel is identified by the wire pitch and the wire planes gap, which are in general of the order of few mm.
Especially in large TPC volumes the lateral diffusion of the electrons, due to long drift distance, is not negligible. The spatial resolution along the drift coordinate (z) is strongly dependent on the diffusion suffered by the electrons while drifting:

$$\sigma_z = \sqrt{\frac{2Dz}{\overrightarrow{v}_{drift,e}}} \tag{1.20}$$

where D is the Diffusion coefficient for electrons (D$\propto \lambda_t^{\frac{3}{2}}$, with λ_t mean free path of the electrons the medium) and $\overrightarrow{v}_{drift,e}$ is the drift velocity, which is proportional to the applied electric field $\overrightarrow{E}$ and to the electron mobility μ_e.

As prevoiusly said, it is possible to integrate to ionized charge along the track, summing the signals recorded in the collection plane. Since the ionized charge is proportional to the energy deposit, the charge integral provides a calorimetric information on the energy of the particle that has produced such ionization. LArTPC detector is

thus an homogeneous calorimeter with high-resolution.
The energy resolution achievable for contained particles in a LArTPC [22]:

- $\frac{\sigma(E)}{E} = 11\ \% \sqrt{E(MeV)} + 2\ \%$ for low energy electrons, measured by ICARUS experiment [17],
- $\frac{\sigma(E)}{E} \simeq 3\ \% \sqrt{E(GeV)}$ for electro-magnetic showers, expected,
- $\frac{\sigma(E)}{E} \simeq 30\ \% \sqrt{E(GeV)}$ for hadronic showers in pure Argon, expected.

From the track and the calorimetric information is possible to achieve high precision particle identification, measuring the deposited charge from ionization per unit length and the range of particles that stops in the sensitive volume. See Fig.1.11.

The main LArTPC detectors features are here summarized:

- it's a 3-D tracking device that also allows event topology reconstruction,
- a measurement of local energy deposition ($\frac{dE}{dx}$) is feasible and it would provide e/π_0 separation and particle identification (PID) via residual range vs $\frac{dE}{dx}$ (π, K and p separation) (See Fig. 1.11),
- it would be possible to have total energy reconstruction of the event from charge integration on each track,
- it would be possible to obtain a momentum estimation via multiple scattering too.

The chamber can be used in a wide energy range (MeV to few GeV) and low thresholds for PID are possible given the high-granularity. It would be also possible, as proposed for the gas filled TPCs, to embed the detector in a magnetic field for charge discrimination.

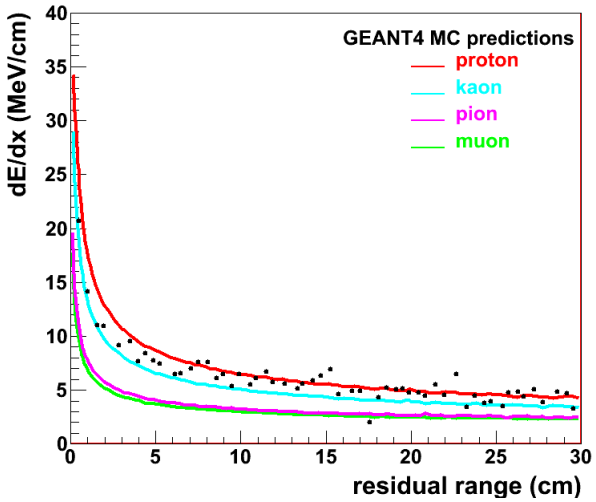

Figure 1.11: Specific energy loss per unit track length (average value) in LAr as a function of the residual range (distance to the track end) for different charged particles. Black points are ArgoNeuT experimental data from calorimetric reconstruction of the energy loss along the stopping tracks for mainly protons. [24]

1.2.4 LArTPC experiments at FNAL

Currently there is worldwide interest in utilizing LArTPC technology for studying neutrino interactions.
The goal would be deploying multi-kiloton LArTPC in near and far-detector locations as part of short and long-baseline neutrino oscillation and proton decay search programs.

In the US LArTPC program towards the construction of a massive LArTPC detector for long-baseline neutrino experiment DUNE [7], a first step has been the construction of the ArgoNeuT detector. [23] [24]
ArgoNeuT has been an R&D project at Fermilab to expose a small-scale LArTPC to the NuMI neutrino beam for ν-Argon interaction studies and eventually cross section measurements.
This was the first LArTPC operated in a "low-energy" neutrino beam (0.5-10.0 GeV neutrino energies range); these energies were relevant for long-baseline neutrino oscillation searches, as discussed in Sec.1.1.2. ArgoNeut consisted of a vacuum insulted cryostat for ultra-pure liquid Argon (LAr) containment in which it was mounted a TPC with its field-shaping system. The Argon inside the cryostat was maintained in liquid phase at constant temperature, around 88K, and a purification system -filter- was used to lower the concentration of electronegative impurities, as O_2, to less than 0.5 ppm. The TPC had an active volume of 47 cm (width) x 40 cm (height) x 90 cm (length), corresponding to a volume of $\approx$ 170 liters = 0.17 tonn of Liquid Argon. This volume was delimited by a rectangular box structure sitting inside the cryostat. The chamber was oriented in a way such that the longest dimension was parallel to the neutrino beam. Two opposite sides (40 cm x 90 cm) were instrumented as cathode and anode planes of the TPC, with the drift direction horizontal with respect to the ground and perpendicular to the beam (maximum drift length l_d=47 cm). There were three parallel wire-planes, equally spaced with interplane gaps of l_g=4 mm; the wire spacing onto the planes was δ_s=4 mm too.
The ArgoNeut experiment was commissioned in 2008 and acquired events from neutrino and anti-neutrino beam mode until February 2010. Then the ArgoNeuT TPC was refurbished to be used in LArIAT experiment. (See Ch.2)
A neutrino interaction event seen in ArgoNeuT, both on the two planes 2-D views (Induction and Collection planes), and the same event with its 3-D reconstruction are shown in Fig.1.12 and Fig.1.13. A detailed description of the analysis of TPC signals ad track reconstruction would be done in Ch.4.

The following step in the Us LArTPC program has been the commissioning and construction of MicroBooNE Experiment. [26] [27]
The experiment consists in a 170 ton Liquid Argon Time Projection Chamber (LArTPC) located along the Booster neutrino beam line, which aims to measure low energy neutrino cross sections. The MicroBooNE detector is a 60 ton fiducial volume LArTPC. It is placed at Liquid Argon Test Facility (LArTF) at Fermilab and it is the largest LAr TPC operating in the U.S. at the moment. The TPC consists of a cathode plane on one side, a field-shaping cage around the drift perimeter, and three planes of wires on the opposite end to record the signal. Further timing information will be provided by a photomultiplier tube (PMT) array measuring the scintillation light produced during the excitation of Ar atoms during an event. The experiment was commissioned in 2008, then the TPC was built and inserted into the cryostat in late 2013; then cryostat was moved to LArTF in June 2014 and the experiment has been running in the neutrino beamline since June 2015.

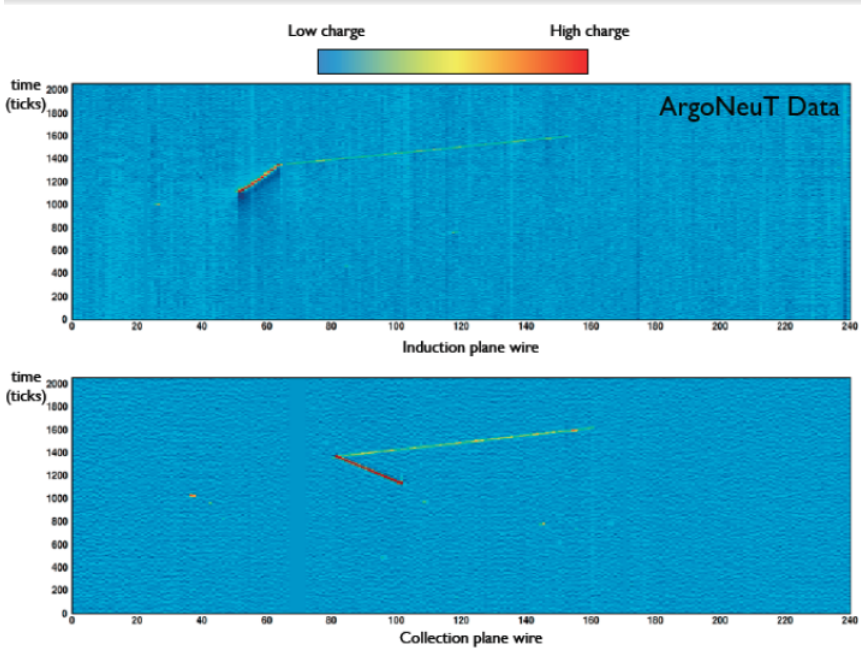

Figure 1.12: A CC ν_μ interaction event candidate (Run 627, Evt. 4192): the yellow trail corresponds to a MIP-like particle escaping ArgoNeuT, the red trail signifies a more densely ionizing particle (presumably a proton, leading to a possible CC-QE signature). [24].

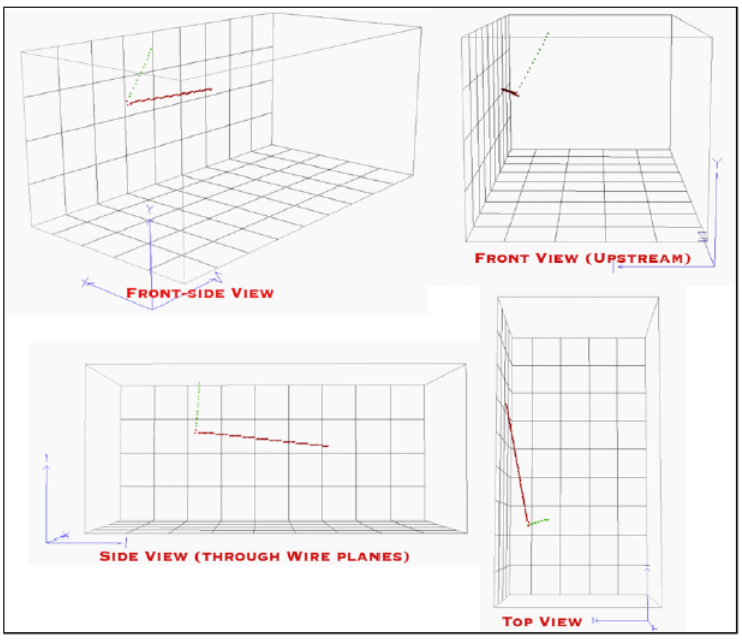

Figure 1.13: ArgoNeuT Neutrino event reconstructed in 3D space (Run 627, Evt. 4192, 2-D views shown in Figure 1.12). One track exits the TPC volume through the cathode plane. [24].

1.3 Liquid Argon scintillation light detection

While the LArTPC is used to collect and measure the ionization electrons generated by charged particles that pass through LAr, there is also an interest in collecting the LAr scintillation light for triggering purposes, as previously said, and the aim is to extend its use for calorimetric energy reconstruction.

1.3.1 LAr scintillation process

This process happens through two mechanisms, see Fig.1.14:

$$Ar^* + Ar \longrightarrow Ar_2^* \longrightarrow 2Ar + \gamma$$

or

$$Ar^+ + Ar \longrightarrow Ar_2^+,$$
$$Ar_2^+ + e^- \longrightarrow Ar_2^* \longrightarrow 2Ar + \gamma$$

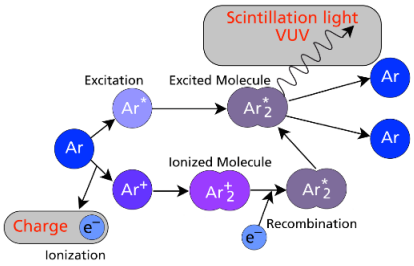

Figure 1.14: Liquid Argon scintillation process

The decay of the molecule of Ar_2^* results in an emission of ultraviolet photons narrowly peaked at 128 nm.
The argon molecule can be excited to either a singlet $^1\Sigma_u^+$ or triplet $^3\Sigma_u^+$ state; the scintillation photons from these two states have two different mean lifetime: singlet-fast $\tau_F \approx 6$ ns, triplet-slow $\tau_S \approx 1.26$ μs. Since the first Ar electronic excited state is at a higher energy than the singlet and triplet excited states, LAr is transparent to its own scintillation light.
The Liquid Argon scintillation signal S(t) is thus the convolution [2] of a gaussian distribution f(t,σ) (with $\sigma_G \simeq$ 4 ns), which represents the population of the excited states, with the double exponential distribution of the excited states decay via emission of scintillation photons, $N_\gamma(t)$. See Eq. 1.21.

$$\begin{aligned} S(t) &= f(t,\sigma) \otimes N_\gamma(t) \\ f(t,\sigma) &= \frac{1}{\sigma\sqrt{2\pi}} e^{-\frac{t^2}{2\sigma^2}} \\ N_\gamma(t) &= \frac{A}{\tau_F} e^{-\frac{t}{\tau_F}} + \frac{B}{\tau_S} e^{-\frac{t}{\tau_S}} \end{aligned} \tag{1.21}$$

[2] The convolution of two functions f(t) and g(t) is represented by the integral I(t):

$$I(t) = f(t) \otimes g(t) = \int_0^t f(\tau) g(t-\tau) d\tau = \int_0^t g(\tau) f(t-\tau) d\tau$$

In Eq.1.21 A and B parameters depend on the kind on incident particle in LAr. For example, for a MIP (muon,pion): A=0.3, B=0.7.
Detecting the scintillation photons from LAr in large neutrino detectors is technically challenging because of the difficulty in detecting the VUV photons efficiently. However LAr has an high scintillation light yield and is transparent to its own scintillation light, so the scintillating photons can be detected at a significant distance from their source.(See Par.1.2.2)

The LAr scintillation signal $i_{out}(t)$ that would be collected by a dedicated light detector is the convolution between the photon time distribution S(t), from Eq.1.21, and the optical device response $R(t)$, as shown in Eq.1.22.

$$i_{out}(t) = S'(t) \otimes R(t) \tag{1.22}$$

1.3.2 Wavelength shifting of LAr scintillation light

The LAr light collection is usually performed with optical photodetectors, as PMTs. These devices are sensitive to optical photons and not directly to LAr scintillation ones. So generally the scintillation photons are wavelength shifted into optical.
Many experiments use TPB (Tetraphenyl butadiene) as wavelength shifter material, to shift LAr scintillation VUV photons wavelength into optical ($\lambda \simeq 428$ nm).
The main effect of the TPB wavelength shifter on the scintillation photon distribution is to add an intermediate decay exponential to the distribution ($\tau_I \approx 34$ ns); it's due to the TPB typical optical response to incident photons.[28] The new convoluted scintillation response S'(t) is in Eq.1.23.

$$\begin{aligned} S'(t) &= f(t,\sigma) \otimes N'_\gamma(t) \\ N'_\gamma(t) &= \frac{A}{\tau_F} e^{-\frac{t}{\tau_F}} + \frac{B}{\tau_S} e^{-\frac{t}{\tau_S}} + \frac{C}{\tau_I} e^{-\frac{t}{\tau_I}} \end{aligned} \tag{1.23}$$

In Eq.1.23: A=0.188, B=0.738, C=0.074 for a MIP in LAr. In Fig. 1.15 is shown the expected LAr + TPB scintillation light distribution S'(t), from Eq.1.23.

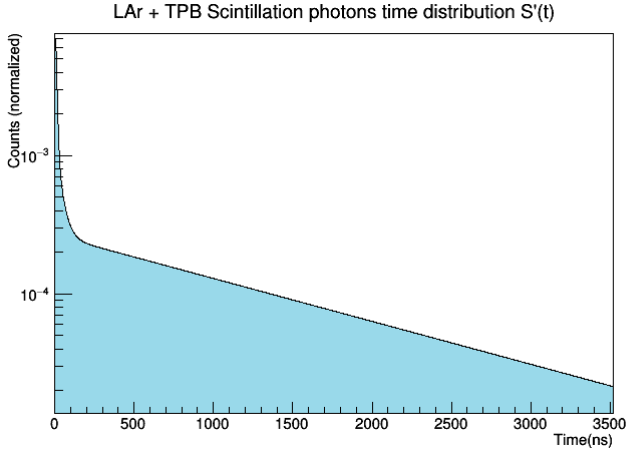

Figure 1.15: Expected LAr+TPB scintillation light photons time distribution.

Chapter 2

LArIAT: Liquid Argon TPC In A Testbeam

LArIAT stands for **Liquid Argon TPC In A Testbeam**.
This experiment is part of the **LArTPC neutrino program** at Fermilab.[29]

A full characterization of the LArTPC technology performance is considered of fundamental interest for the development of the Intensity Frontier Program in the US, especially for the SBN and LBN programs for precise neutrino oscillation physics and proton decay searches.
The LArIAT program consist in a full **calibration of the Argon TPC in a dedicated beam line**. (See pictures 2.1, 2.2 and 2.3.)
The experiment is focused on the study of all the charged particles that could emerge from SBN/LBN neutrino interactions in Liquid Argon; therefore the detector is placed on a beam of charged particles of known type and momentum, in the momentum range from 0.2 to 2.0 GeV/c. The aim is to characterize the signal from different particles in the LArTPC and to find criteria to discriminate among them. The charged particle testbeam will help to develop and validate the off-line software tools of particle identification, calorimetry and event reconstruction without relying solely on simulations.

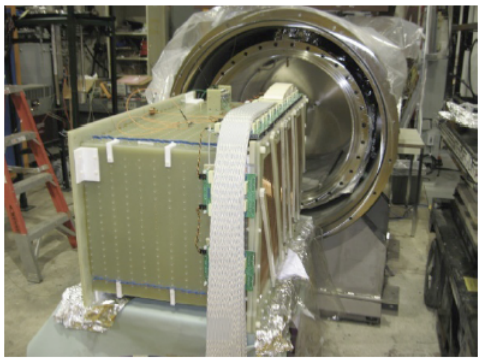

Figure 2.1: LArIAT TPC before it was settled inside the cryostat

Figure 2.2: LArIAT cryostat in the beamline in MCenter - FTBF

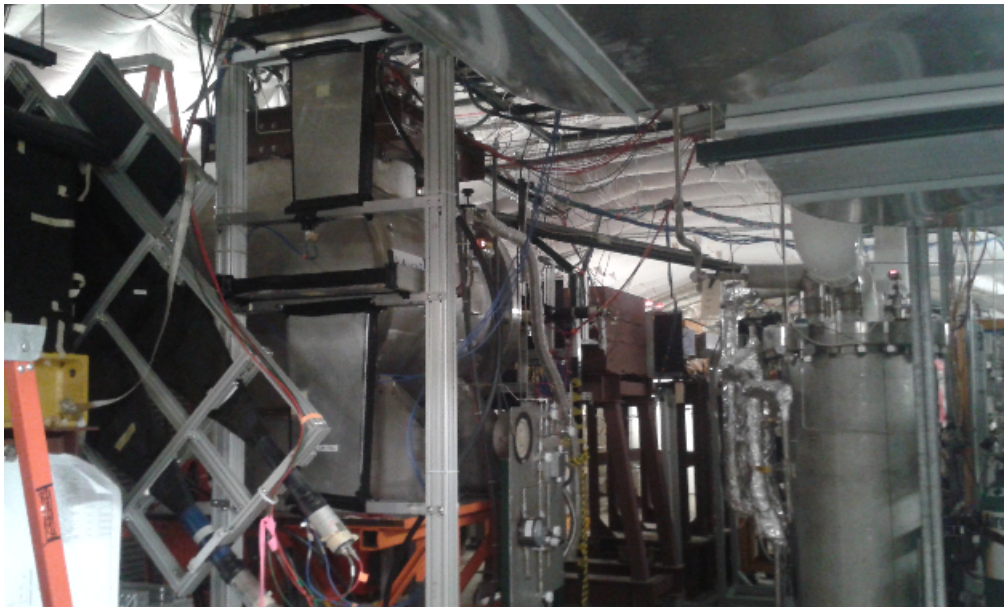

Figure 2.3: LArIAT TPC cryostat and beamline detectors at MCenter - FTBF

2.1 LArIAT main goals

LArTPC detectors offer full 3D imaging, good particle identification and precise calorimetric reconstruction.
The principal features that make high purity Liquid Argon detectors so interesting are: the electromagnetic shower reconstruction and separation of e-/gamma induced showers by the characteristic energy loss at the beginning of the shower, the determination of muon charge via its endpoint capture or decay, the identification of pions and kaons through the analysis of their interactions in Liquid Argon, the combined study of the deposited energy by ionization charge and scintillation photon yield.

2.2 Testbeam and beam line

At FTBF a primary beam of high energy protons (120 GeV) is targeted to a 25 cm thick target to create secondary charged particles (mainly pions, 1 - 80 GeV range) for two beamlines, MTest and MCenter. The MCenter line provides a collimated pion beam that is targeted on a thin Cu-plate and collimated by a collimator and two bending Fe-magnets; in this way we obtain the LArIAT dedicated tertiary beam composed by mainly pions and protons with momentum tunable between 0.2 and 2.0 GeV/c, as a function of the magnetic field. The tertiary beam is monitored by a set of Time of Flight (ToF) counters, a set of Wire Chambers (WC), two Aerogel counters (AG), an Halo Veto, a Muon Range Stack...[30] [31] (See Fig.2.3 and Fig.2.5.)

The expected particle composition of the tertiary beam is shown in Fig. 2.6 for a π^+ secondary beam on Cu-target for 0.35 T/100 A (magnetic field- current intensity) configuration of the Fe-bending magnets that provides high energy tuned particles (500 MeV/c - 2.0 GeV/c momentum). It is possible to obtain a low energy tuned tertiary beam (200 MeV/c - 700 MeV/c momentum) with 0.175 T/50 A magnets configuration. The charge of the particles that are driven to the TPC can be selected by changing the polarity of the bending magnets.

Figure 2.4: View of FTBF (Fermilab Test Beam Facility).[32]

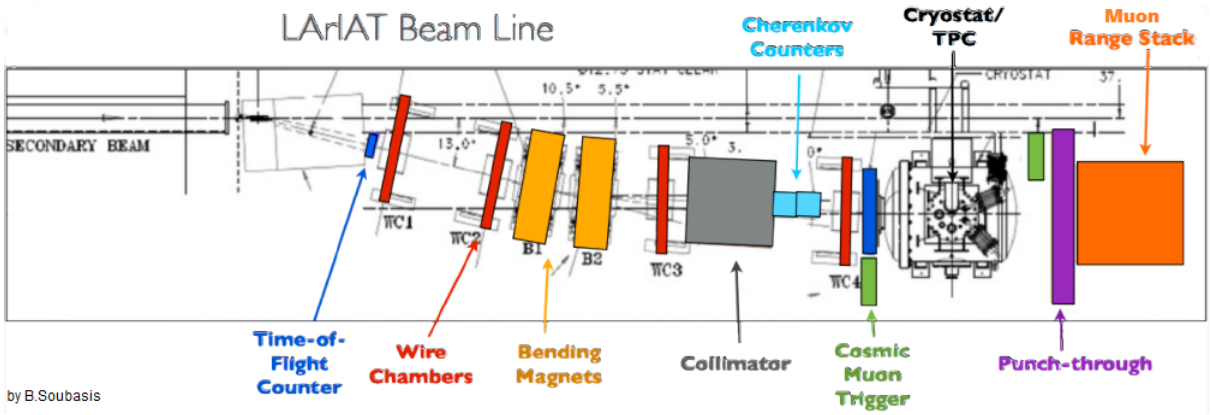

Figure 2.5: Schematic reconstruction of the tertiary beam line at MC7 - MCenter.

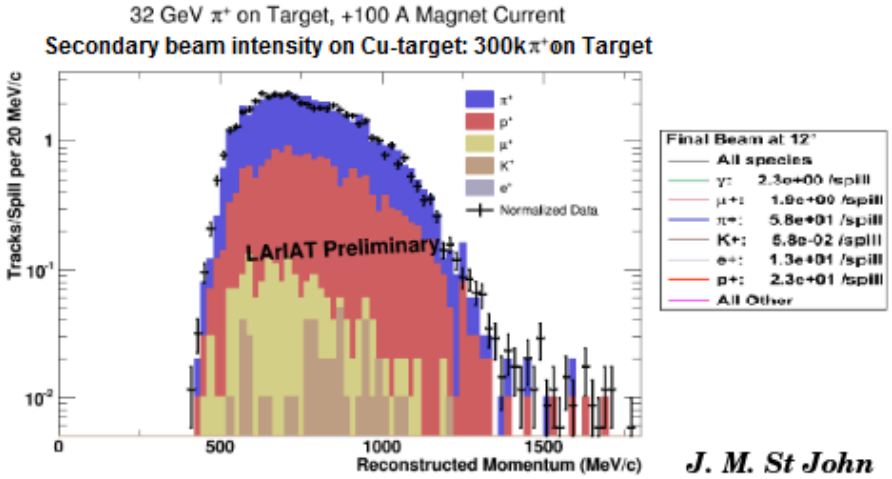

Figure 2.6: Expected tertiary beam composition for π^+ on Cu-target after the bending Fe-magnets - high momentum tuned - +100 A current on the magnets.

The ToF counters along the beamline are necessary to make Particle IDentification for the incoming particles to the TPC. The UpStream ToF scintillation counter is placed after the collimator, while the DownStream ToF is placed close to the TPC beam-entering window. The ToF evaluation can make us distinguish among protons, kaons and pions, since protons are slower than kaons and pions, due to their higher mass. The distinction between pions and muons is not feasible at this stage because the time

of flight of these two particles is quite close in this energy range and with our ToF detectors temporal resolution is not possible to distinguish between these two species. We hope to manage also to achieve pion to muon identification by the coupling the ToF measurements to Aerogel counters response and to the study of the topologies of the interactions seen in the TPC. (See Fig.2.7 and 2.8). The coincidence of the ToF signals with WC signals is also used as the former trigger for the system to select particles coming from the Cu-target and getting through the TPC.

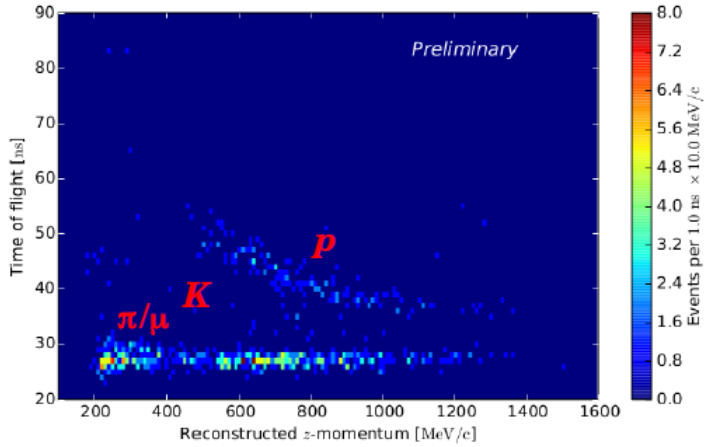

Figure 2.7: Time of Flight vs reconstructed momentum for tertiary beam particles.(MC simulation)

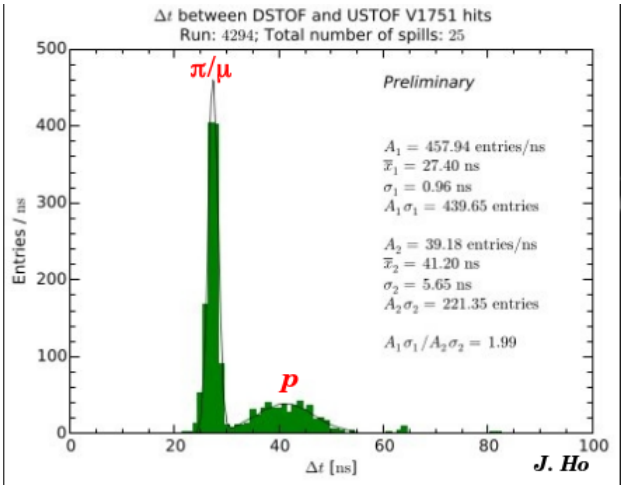

Figure 2.8: Time of Flight distribution for tertiary beam particles. (Data) See beam composition π^+:p $\approx$ 2:1.

2.3 LArIAT: TPC for ionization free charge collection

The liquid argon-related part of the experiment consists of the LArTPC detector, the LAr scintillation light detectors, the LArTPC read-out cold electronics, the liquid argon cryostat, and the cryogenic system connected to the cryostat for liquid argon cooling and purification.

The vacuum-insulated cryostat and the inner detector TPC are pre-existing components from ArgoNeuT experiment [23] [24].

Liquid argon is contained in a stainless-steel, vacuum-jacketed and insulated cryostat. The cryostat shape is cylindrical with convex end-caps. The main axis of the cryostat is horizontal and oriented parallel to the beam. The cryostat has a wide neck on the top that serves as access path for signal cables from the LArTPC and from the internal instrumentation, as well as for the high voltage (HV) feed-through. The cryostat has a "beam window" to reduce the amount of material upstream of the TPC active volume along the beam line, a connection for the Argon cooling and purification system and a connection flange for the scintillation light readout system.

The TPC consists in rectangular box structure in which anode wires are tensioned at one side and at the other side we find the cathode plane.
The active volume is 47 cm (width) x 40 cm (height) x 90 cm (length), corresponding to a volume of 170 liters of Liquid Argon.

The anode wire spacing - pitch δs - is 4 mm in all planes. There are three wire planes to see the drifting electrons inside the TPC. (See LArTPC: principles of operation Par.1.2.3.)
The first plane, the "Shield plane", contains 225 parallel equal length wires, vertically oriented with respect to the ground and perpendicular to the beam axis. This plane is not instrumented for the readout and serves to shape the electric field near the wire-plane and to shield the outer, instrumented planes against induction signals from the ionization charges while they are drifting through the LArTPC volume. The second, "Induction", plane consists of 240 wires oriented at +60deg relative to the beam axis. Electrons induce signals on this plane only after crossing the Shield plane and moving toward (bipolar current pulses). The third plane, the "Collection" one, is made up of 240 wires oriented at -60deg relative to the beam axis. Electrons are collected onto these wires at the end of their drift (unipolar current pulses). The wires of the induction and collection planes are of varying lengths.
The cathode is a G10 plain sheet with copper metalization on the inner surface opposite the anode wire planes; its biased at negative high voltage. The electric field is uniform over the entire TPC drift volume with a nominal value of 500 V/cm from the cathode to the anode planes, with a maximum drift length of $\approx$ 47 cm.
Induction and collection planes wires are read with dedicated cold electronics: cold preamp motherboard cards with ASIC chips, designed by Brookhaven National Lab, are mounted over the TPC inside the cryostat. The ASIC signals for each wire are then driven to out of the vessel DAQ boards that act as waveform recorders.
In Fig.2.9 there is a schematic view of the LArIAT TPC mechanism and in Table 2.1 there are its nominal specifications and features.

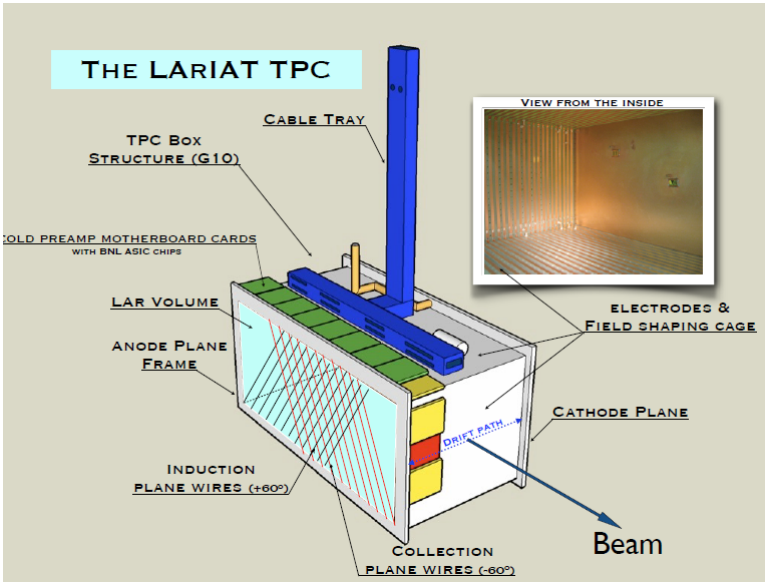

Figure 2.9: Schematic view of LArIAT TPC.[30]

TPC dimensions	40 h × 47 w × 90 l cm^3
TPC (active) volume	170 liters
Max. Drift Length (TPC width)	l_d = 470 nm
Number of wire-planes	3 (2 instrumented- I, Cl)
Interplane gaps width	l_g= 4 mm
Wire pitch (normal to wire direction)	δs = 4 mm (all planes)
Number of wires (total) Shield plane (S) Induction plane (I) Collection plane (C)	705 225 (non-instrumented) 240 (instrumented, wire index: n_w^I 240 (instrumented, wire index: n_w^C
Wire Orientation (w.r.t. horizontal)	90deg S , + 60deg I, - 60 deg C
Non-destructive configuration Drift volume S-I gap I-C gap	Electric Field (EF) nominal E_d= 500 V/cm E_{g1}= 700 V/cm E_{g2}= 900 V/cm
Electron drift velocity at nominal EF value	1.59 mm/μs
Max drift time at nominal EF	t_d = 295 μs

Table 2.1: LArIAT TPC nominal specifications and features.[24]

2.4 LArIAT: LAr scintillation light collection system

LArIAT's light collection system consists of an array of two high quantum efficiency cryogenic photomultiplier tubes (PMTs) and three Silicon Photomultiplier Detectors (SiPM). They were deployed in Liquid Argon and mounted behind the wire planes of the TPC. The assembled system is shown in Figure 2.10, 2.11 and 2.13.
The PMTs were used in previous tests and experiments by the WArP collaboration [35]; however the SiPM preamplifier boards were custom-designed for LArIAT (See Chapter 5).
The LAr scintillation UV photons are wavelenght shifted into optical by covering the whole TPC with TPB coated reflective foils. [33] See Fig.2.12.

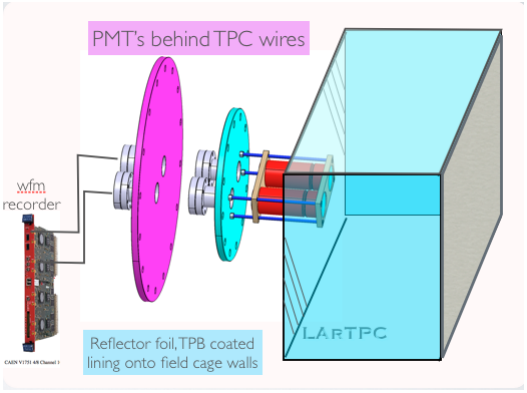

Figure 2.10: Schematic view of Scintillation Light Collection System with PMTs

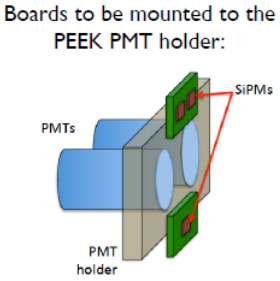

Figure 2.11: Schematic view of PMT and SiPM inner flange support.

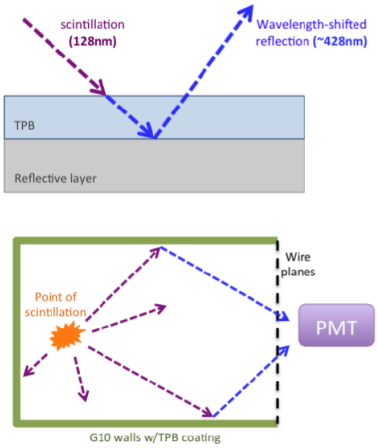

Figure 2.12: TPB coating of the boundary surfaces of the TPC volume and its wavelength shifting effect on LAr scintillation light.

Light collection system:

- Hamamatsu R-11065 PMT [36]: 3-inch diameter head-on PMT with low radioactivity and high photon detection efficiency,

- Electron Tubes Limited (ETL) D757KFL PMT [37]: 2-inch diameter PMT;
  the two PMTs have been specifically designed to operate under cryogenic temperatures and their operating voltage in Liquid Argon is within -1300 and -1500 V.
- SensL MicroFB 60035 SiPM with an OPA656 opamp,
- Hamamatsu S11828-3344M 4x4 SiPM array with an ADA4891 opamp,
- Hamamatsu S11828-3344M 4x4 SiPM array with an OPA656 opamp;
  the SiPM features, the circuit schematics and the tests we made before the installation in the cryostat are described in Chapter 5.

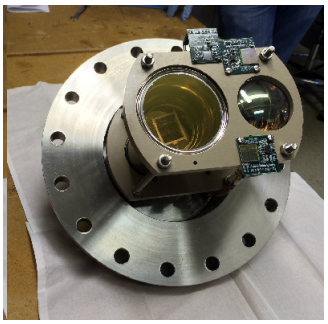

Figure 2.13: PMTs and SiPMs boards mounted to the inner flange of the cryostat.

The SiPM response to LAr scintillation light would be discussed in Ch.5 Par.5.2.4.

The scintillation light readout is now used only for triggering purposes and measure of TOF; the aim is to extend its use for calorimetric energy reconstruction.
This improvement is achieved by measuring the fraction of energy deposited into scintillation light and using pulse shape discrimination for PiD.
We expect an improvement of the calorimetric energy resolution up to a factor two when the scintillation light signal would be combined with TPC charge signal.[34]

2.5 TPC cryogenics and purity controls

The parameters of Argon inside the cryostat need to be monitored continuously, to maintain the medium at liquid phase, in a sufficient amount and with a low level of impurities contamination.
Level and pressure of LAr are monitored with a control system sitting inside the cryostat; since LAr inside the cryostat evaporates with time, every week there is a LAr refill. The pressure is monitored to maintain always vacuum inside the cryostat.
There is also a thermo-resistor system to check the temperature or Argon inside the vessel; having a temperature of 90 K ensures the medium is in the liquid phase.
Moreover there is a purification filter outside the cryostat to remove electronegative impurities from Argon flowing into the vessel. Electronegative impurities are expected to have a very low concentration: oxigen $O_2 \simeq 0.003$-0.140 ppm; $H_2O \leq 0.050$ ppm; nitrogen $N_2 \leq 0.7$ ppm.

2.6 Trigger and DAQ

The LArIAT trigger and DAQ system consists of modular electronics and computer systems which initiate detector read-out, do analog to digital conversion, interface and synchronize with the accelerator system, store raw data on disk, transfer data to archival storage and conduct first pass data quality monitoring. The system is made by commercial VME electronics from CAEN, a VME time to digital converter for the beamline time of fight system, and a readout system for beamline wire chambers.

A CAEN V1495 board is used to perform the Trigger of the whole detectors system.[39] It is a VME board, which can be directly customised by the User through two programmable FPGA.
For LArIAT experiment 16 trigger input signals are used, see Fig. 2.14. Through the FPGA configuration file "V1495.config" it is possible to define different trigger conditions - trigger output paths, with several logic combinations of the input signals.
For example:
<trigpat0>
<inreg>0x1104</inreg>
<cntreg>0x1070</cntreg>
<on>BEAMON USTOF DSTOF WCCOINC3OF4</on>
<off>HALO</off>
</trigpat0>
The former trigger output path is the one that selects particles from the beam that cross the whole beamline and get to the TPC.
Moreover it's possible to add a delay to the trigger and to set some combinations of signals as a VETO.

Trigger inputs
2015.05.08 14h20

```
0   WC1       | OR of 2 X view TDCs ANDed with OR of 2 Y
1   WC2       | "                                      "
2   WC3       | "                                      "
3   WC4       | "                                      "
4   BEAMON    | Spill gate : STARTs on $21, STOPs on $36 (cable says $26 but Bill says $36)
5   USTOF     | OR of 4 PMTs
6   DSTOF     | OR of 2 PMTs
7   PUNCH     | OR of 2 X view paddles ANDed with OR of 2 Y
8   HALO      | OR of 2 PMTs
9   PULSER    |
10  COSMICON  | Cosmic gate : STARTs on $36, STOPs on $00 (not optimal, would like to stop before $00)
11  COSMIC    | the trigger signal from the cosmic rack
12  PILEUP    | Coincidence of any later LARSCINT with a delayed gate initiated by itself. Higher discrimination thresh.
13  MICHEL    | Coincidence of two light flashes in TPC (LARSCINT) occurring within a 5us time window
14  LARSCINT  | Coincidence of Hamamatsu and ETL PMTs (discriminated)
15  MuRS      | Any coincidence of two planes.  Each plane is the OR of the discriminated pulses of 4 paddles.
```

Figure 2.14: CAEN V1495 board - Trigger Inputs

Waveforms from beamline detectors and optical devices (PMTs and SiPMs) inside the cryostat are collected using two CAEN V1751 boards (For v1751 boards inputs, see Table 2.2.). They are both fed by the V1495 fast trigger. Each has a unit boardId and produces CAENFragment raw data objects.
The CAEN V1751 Waveform Digitizer [40] is VME module housing 8 Channel 10 bit 1 GS/s Waveform Digitizer with 1 Vpp input dynamic range; the range that has been set for our purposes is 204 mV, so 1 ADC count corresponds to 0.2 mV. The input channel provides a programmable voltage offset in the $\pm$ 0.5 V range too; we used this feature to adjust baseline offsets on our signals. The time window can also be adjusted by user maintaining the same sample frequency (1 GS/s); we've started with a 7.168 μs

time window, but after preliminary studies on the signals collected by PMTs and SiPMs we've moved to a 14.336 μs window that could allow us to sample over all the slow LAr scintillation component (τ_S) signal tails, to study single photoelectron response of the optical devices.

boardId	Channel	Input signal
8	0	US TOF 1
8	1	US TOF 2
8	2	DS TOF 1
8	3	DS TOF 2
8	4	AG US E
8	5	AG US W
8	6	AG DS E
8	7	AG DS W
9	0	TPC PMT 1 (Ham.)
9	1	TPC PMT 2 (ETL)
9	2	TPC SiPM 3 (Ham.B)
9	3	TPC SiPM 2 (Ham.A)
9	4	TPC SiPM 1 (SensL)
9	5	beam halo amplified
9	6	beam halo amplified
8	7	AG Cosmic 1

Table 2.2: V1751 Waveform Digitizer boards inputs: beamline detectors and optical detectors in the TPC.
US = upstream, DS=downstream; AG = aerogel counter; TOF = Time of Flight counters; TPC PMTs and SiPMs are the optical devices deployed in LAr. For a schematic of the beamline detectors placement see Fig.2.5.

2.7 Control systems

There are several online slow control systems at LArIAT test beam [38]:

- ACNET : The Accelerator Control NETwork is a system of computers that monitors and controls the accelerator complex. They are interfaced to users through consoles in the FTBF Control Room. We use ACNET for beam monitoring in MCenter beamline. (See Fig.2.15 and 2.16)

- Synoptic: Graphical User Interface (GUI) for representation of real-time data; allows to create plots in a simple way, and eventually set data to control system. We use it basically for whole beamline overview, power voltage and counts monitoring of the beamline detectors as well as for TPC monitoring (cathode and wire planes voltage, PMTs and SiPMs deployed in LAr operating voltage and cryogenic controls). (See Fig.2.17)

- Run Status Webpage (http://lariat-wbm.fnal.gov/lariat/run.html): it shows the current run time evolution, the beam main informations and the trigger conditions.(See Fig.2.18)

- (Near-real-time) DQM (http://lariat-daq01.fnal.gov:5000/): It's a webpage, developed by J.Ho (Univ. of Chicago), connected to lariat-daq, continuously updated with data-blocks from all the VME boards in the trigger and acquisition system and monitoring plots (like ToF distribution, hit time from the MWPC which gives us an information on the beam profile...) from the DAQ stream of raw data for each spill.

- Event viewer: the online event viewer collects all the pulses recorded by the DAQ for each wire on the Induction and Collection planes and plots their amplitude in a 2-D plot (wire number vs drift time), resulting in a two-dimensional representation on two views of the event happening inside the TPC. It is useful to make beam tuning, to reduce intensity and halo particles, and also to study noise effects on the wires, changing their bias voltage and/or the parameters of the ASICs (gain and filter). (See Fig.2.19.)

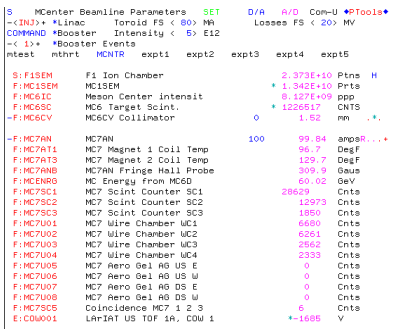

Figure 2.15: ACNET: MCenter Beamline Parameters

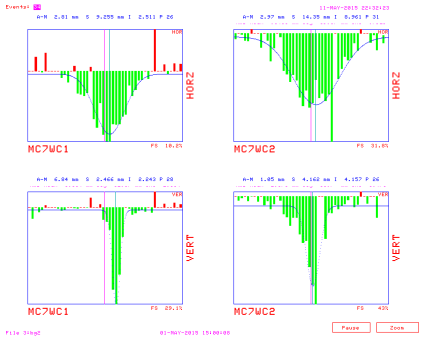

Figure 2.16: ACNET: Beam profile from beamline Wire Chambers

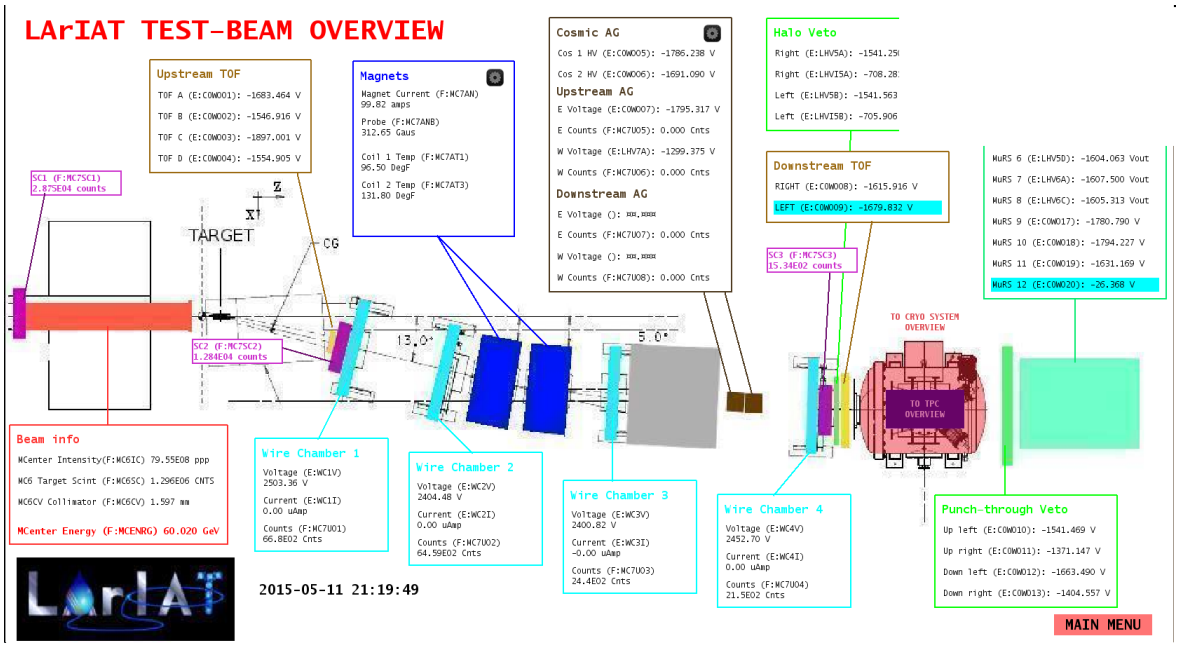

Figure 2.17: Synoptic: LArIAT Test-Beam Overview

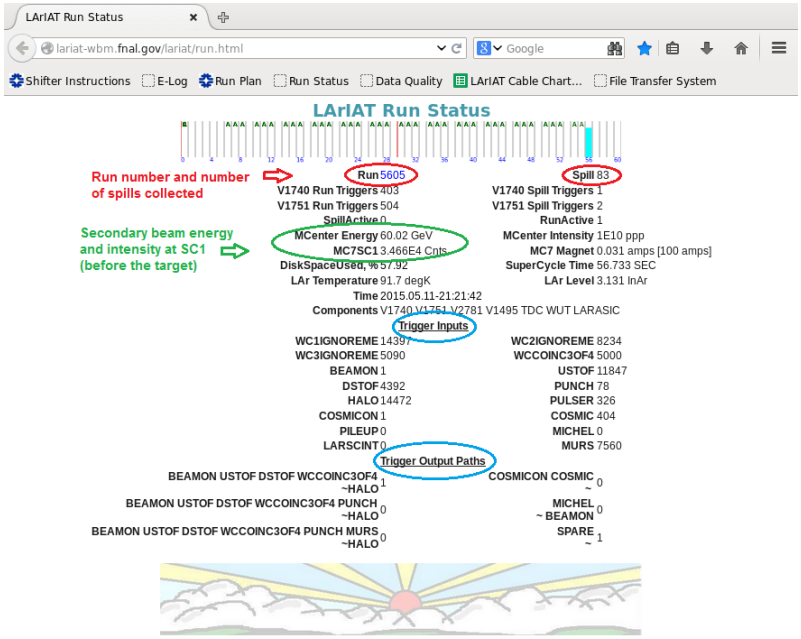

Figure 2.18: LArIAT Run Status webpage (Screenshot)

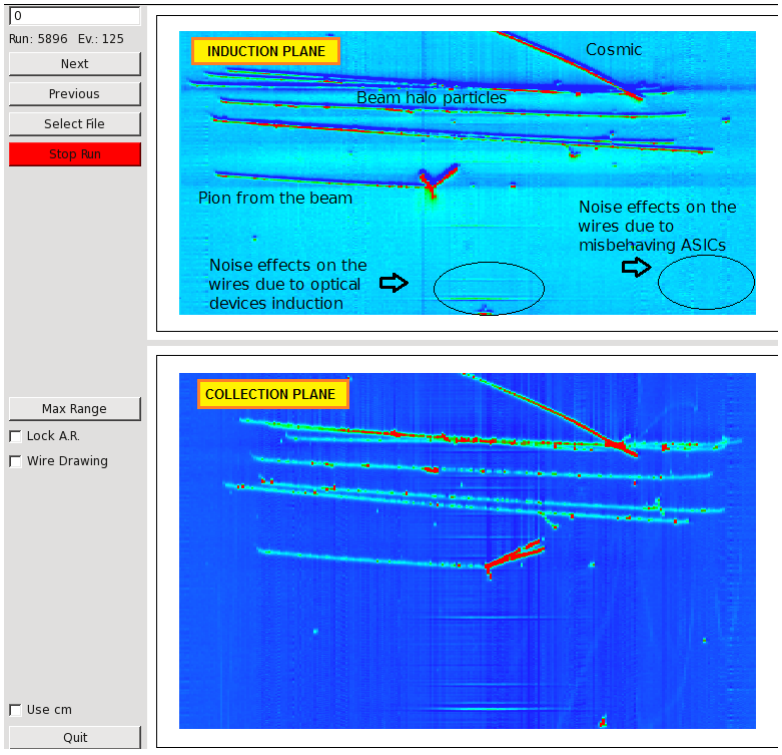

Figure 2.19: Event viewer: example of a "non-clean" event collected in the TPC, with possible sources of noise and halo particles.

Chapter 3

Pion interaction processes in Liquid Argon

Pion interaction with matter was a central topic in particle physics for decades.
Extensive experimental studies were performed with pion beams. Different materials were used as a target, from light to heavy elements, like He, Li, C, Fe, Pb...
The interaction processes are in general well understood based on strong hadronic interaction models.[41][42] [43]
Argon, Ar, target was used for some dedicated pion experiments but in general experimental data for π-Ar interactions are spare.
Current MC simulation codes, like Geant, use interaction models for Ar based on extrapolations from data with lighter or heavier elements.

The goal of a dedicated pion run with LArIAT is to develop pion identifcation algorithms based on their interaction modes in Argon and to exploit direct and precise measurement of the pion-nucleus cross-sections to reduce the uncertainty on the hadron interaction models adapted in MC simulations for Ar target.
The software/analysis oriented part of my activity at FNAL with LArIAT has been a Monte Carlo study of pion interactions in Liquid Argon, the development of a data analysis code to evaluate pion-nucleus total cross section and a possible identification method for different interaction channels.
Next step will be applying this analysis to real data acquired from LArIAT TPC, as described in Ch.4 (preliminary studies).

The ultimate goal is to possibly reduce the systematic error related to π interaction uncertainty in neutrino ν interaction (neutrino energy reconstruction and event topology recognition in future experiments with LAr detectors.

3.1 Charged pion interactions with nuclei

Pions have very large hadronic interaction cross sections with nuclei, especially nearby the Δ resonance region (80 MeV-400MeV).
Therefore pion interactions with nuclei play an important role for neutrino physics. In fact pions are frequently produced in neutrino interactions with nuclei for E_ν in few GeV range, as described in Ch.1 Par.1.1.3.
In Fig.3.1 is shown an ArgoNeuT event: ν_μ interaction with Ar nucleus producing a charged pion.[25]
In Fig.3.2 and Fig.3.3 there are the momentum spectra for secondary particles produced in neutrino interactions, for LBNB beamline ($<E_\nu> \approx 3$ GeV) and Booster

Neutrino Beamline/SBNE ($E_\nu \leq 1$ GeV). In Fig.3.4 there is the momentum distrubution of charged pions produced in ν-nucleus interactions, from Booster neutrinos; this momentum distribution is compared with the charged pions momentum ranges that are accessible from LArIAT tertiary beam.
In order to reconstruct the incident neutrino energy from the outgoing particles, the pion total energy needs to be measured.

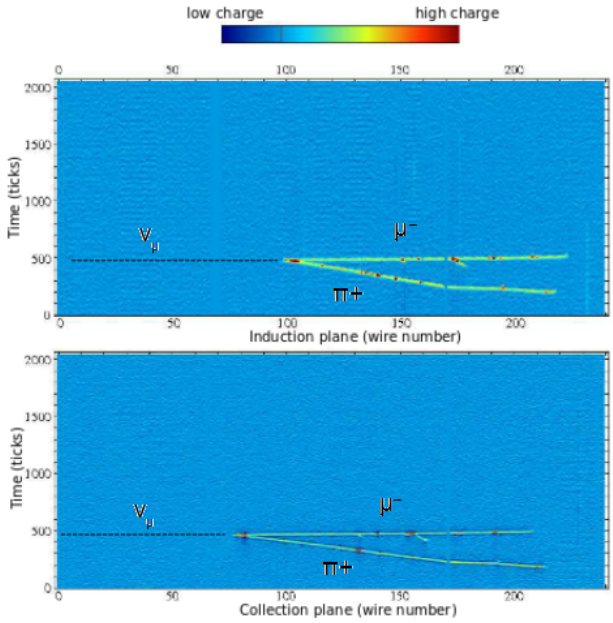

Figure 3.1: An example of CC Coherent pion production from a neutrino in ArgoNeuT: $\nu_\mu + \mathrm{Ar} \rightarrow \mu^- + \pi^+ + \mathrm{Ar}$. The neutrino's incoming direction is along the horizontal coordinate; the muon track corresponds to the most forward going one. A kink in the pion trajectory is visible.[25]

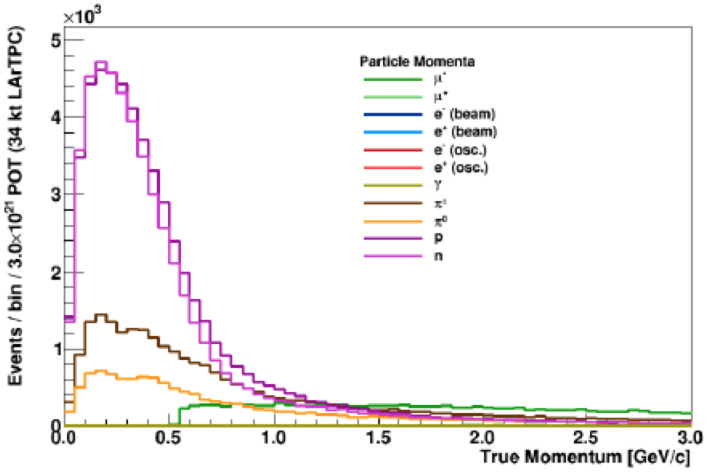

Figure 3.2: Momentum distribution of the secondary particles produced in neutrino interactions, for LBNB neutrino beamline (Long Baseline Experiments).

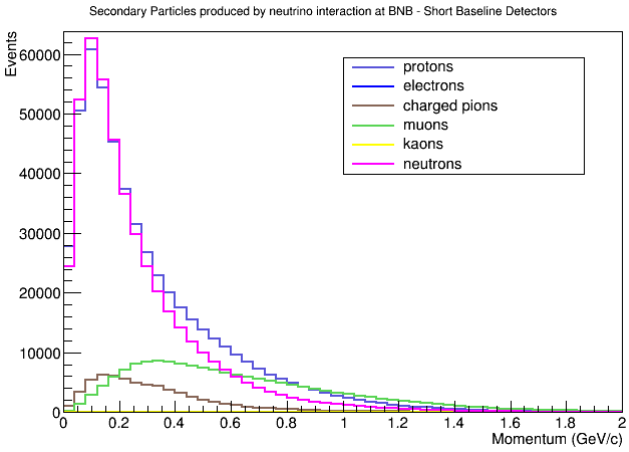

Figure 3.3: Momentum distribution of the secondary particles produced in neutrino interactions, for BNB Booster neutrino beamline (Short Baseline Experiments).

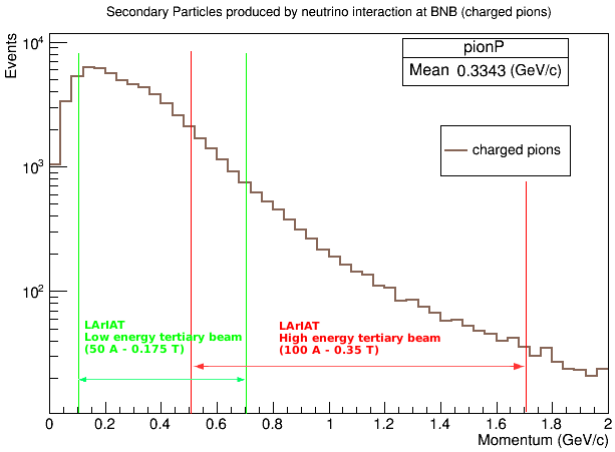

Figure 3.4: Momentum distribution of the charged pions produced in neutrino interactions, for BNB. The charged pions momentum ranges accessible from LArIAT tertiary beam are superimposed.

To first order, the pion in the nucleus (N) can be considered as interacting with individual "free" nucleons either p or n (quasi-free approximation). We can give estimate of the **pion-nucleus hadronic interaction** cross section by means of the "classical" definition of the total cross section, using the optical potential:

$$\sigma_{tot} \approx \pi R^2 \tag{3.1}$$

where R is the "effective" nuclear radius for the interaction. The average nuclear radius R is defined as :

$$R \approx R_0 A^{1/3}$$

with R_0= 1.2 fm, Fermi radius for nuclei.
For Argon, ^{40}Ar, A=40: R $\approx$ 4 fm $\rightarrow$ $\sigma_{tot} \approx$ 500 mb.
This is supposed to be an estimate of the pion interaction cross section order of magnitude, that is so expected to be few hundreds mb. We can easily see that strong hadronic interactions (π-nucleus) have very high cross section compared to the weak neutrino interactions discussed previously ($\sigma_{\pi-nucleus} \approx 10^{10}\ \sigma_{\nu-nucleus}$).

Let's consider now the **pion-nucleus total cross section** σ_{tot} for a pion traveling through a target.
In general the target is not a single particle, but a slab of material containing many diffusion centers; we'll assume the target centers uniformly distributed and the target thin enough not to have one center sitting in front of another one (definition of **thin target**).
The cross section contains the strength of the interaction coupling between the incident particle and the target medium. We can define a *total cross section* $\sigma_{tot}(E)$ for a given energy E at the interaction point as the integral of the differential cross section $\frac{d\sigma}{d\Omega}(E,\Omega)$ over all solid angles.
If we consider a small thickness x (**thin target**), the survival probability in that distance as:

$$P_{surv}(x) = e^{-\frac{x}{\lambda}} = e^{-N\sigma_{tot}x} \tag{3.2}$$

and the interaction probability:

$$P_{int}(x) = 1 - e^{-\frac{x}{\lambda}} = 1 - e^{-N\sigma_{tot}x} \tag{3.3}$$

where λ is the *mean free path - interaction length*, the mean distance traveled by a particle before suffering an interaction, and σ_{tot} is the *total interaction cross section per nucleon*.
Assuming the density of scattering centers N for a target, with nuclear mass A and density ρ (N_A=6.022x10^{23}, Avogadro Number):

$$N = \frac{\rho N_A}{A}$$

we can write the total cross section per nucleon in terms of interaction length:

$$\sigma(E) = \frac{A}{\lambda(E)\rho N_A} \tag{3.4}$$

To perform an experimental measurement of the **pion-nucleus total cross section** we aim to scan different pion initial energies and count how many interactions N_{int} have happened or not N_{surv}.

$$N_{surv} = N_{inc} - N_{int} \tag{3.5}$$

where N_{inc} are the number of pions shot onto the target, $N_{interaction}$ are the number of them which have experienced an interaction inside the target.
From the rate of interactions at each energy we can calculate the total cross section σ_{tot} from:

$$N_{surv}(x,E) = N_{inc}e^{-\sigma_{tot}(E)Nx} \tag{3.6}$$

where x is the target thickness (cm), along the incident pion direction, N is the scattering centers density in the target (cm^{-3}) and and σ_{tot} (cm^2) is the total cross section per nucleon.

The total pion-nucleon cross section σ_{tot} calculated with this method and its statistical error, assuming in this case a known fixed number of incident pions N_{inc}, are shown in Eq.3.7:

$$\begin{aligned} \sigma_{tot} &= ln(\frac{N_{inc}}{N_{surv}})\frac{1}{Nx} \\ \Delta\sigma_{tot} &= \frac{1}{Nx}\frac{1}{N_{surv}^2}N_{inc}\Delta N_{int} = \\ &= \frac{1}{Nx}\frac{1}{N_{surv}^2}N_{inc}\sqrt{N_{int}} \end{aligned} \tag{3.7}$$

N_{int} counts follow a binomial distribution, since the pion could either interact in thickness x or survived and cross that target. Since for a thin target, the number of interactions N_{int} is very low while the number of incident particles N_{inc} can be high enough, we find ourselves in the Poisson distribution limit for N_{int}; this is the reason why I've assumed a Poisson statistical error on N_{int} in Eq.3.7.

When the "thin target" approach is not applicable, i.e. the case of **thick target** experiments, to get a precise evaluation of the pion cross section dependence on energy, it is necessary to have the information about the energy lost by the pion while crossing the target before the interaction, i.e the energy of the primary particle at the interaction point. For this reason we have to take in account the primary particle energy deposition by collisions with atoms of the medium before the interaction happens.

The average energy loss (or stopping power) $\frac{dE}{dx}$ (MeV/cm) for a charged particle is well described by the *Bethe-Bloch formula*, see Eq.3.8, which takes in account the quantum-mechanical calculation of the energy transfer from the incident particle to the atom of the medium causing an ionization or an excitation of the latter. It treats the energy loss as a uniform and continuous process.

$$-\frac{dE}{dx} = Kz^2\frac{Z}{A}\rho\frac{1}{\beta^2}[\frac{1}{2}\ln(\frac{2m_ec^2\beta^2\gamma^2T_{max}}{I^2}) - \beta^2 - \frac{\delta}{2} - \frac{C}{Z}] \tag{3.8}$$

in which: K=0.307075$\frac{MeVcm^2}{g}$.
For example:
Target - absorbing material (LAr): density ρ=1.396$\frac{g}{cm^3}$, $\frac{Z}{A}$=0.45059, mean excitation potential I=188eV.
Incident particle (Pion+/-): z^2=+1, $\beta = \frac{v}{c}$ and $\gamma = \frac{1}{\sqrt{1-\beta^2}}$ are the relativistic values for the incident particle, the maximum energy transfer in a single collision $T_{max} \approx 2m_ec^2\beta^2\gamma^2$ (if M » m_e, with M mass of the incident particle and m_e electron mass).
δ is the "density correction", which becomes important for high energies of the incident particle. It describes the fact that the electric field of the primary particle polarizes the atoms along its path and electrons far from the path of the particle are shielded from the full electric field intensity and the collisions with them contributes less to the total energy loss.
C is the "shell correction", which becomes important when the velocity of the incident particle is comparable or smaller than the orbital velocity of bound electrons in the absorber, so the Bethe-Bloch formula assumption that the electron is stationary with respect to the incident particle is no longer valid. In general this correction is very small though.
Fig.3.5 show the Bethe-Bloch formula as a function of kinetic energy for several different particles (μ, π, K, p, d and α) in Liquid Argon.

We should note that, when the target is thin, it's reasonable to consider only the pion-nucleus hadronic interactions, while for thick target experiments we should also consider the possibility of **pion decay** (τ_π = 2.6 x 10^{-8} s) in the target volume (decay in flight and decay at rest).

$$\pi^+ \longrightarrow \mu^+ + \nu_\mu \quad \text{BR } 99.98\%$$
$$\pi^- \longrightarrow \mu^- + \overline{\nu_\mu} \quad \text{BR } 99.98\%$$

In case of a π decay at rest the 2-body decay constrains the $\mu^\pm$ to have $\approx$ 5 MeV kinetic energy and it shortly decays into a $e^\pm$.

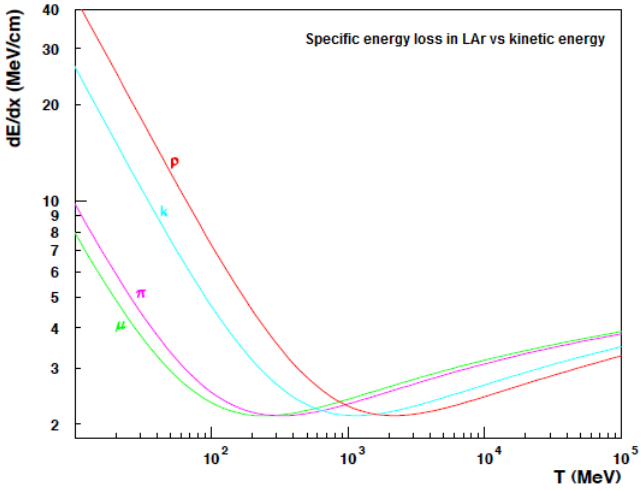

Figure 3.5: The stopping power $\frac{dE}{dx}$ as function of kinetic energy for different charged particles (p, $K^{\pm}$, $\pi^{\pm}$, $\mu^{\pm}$) in Liquid Argon.

For negative pions π^- at the end of range (near stopping) another process has to be taken in account: the **capture at rest** on target nuclei.
A stopping π^- can be tighten around one target nucleus and move on a closer orbit than an electron due to its higher mass. Then as soon as the pion sits in an orbit very close to the nucleus surface it can be absorbed; the capture process is so "at rest" in the nucleus reference system.
The nuclear capture of negative pions at rest leads in general to the emission of low energy nucleons. First, the pion is absorbed on a cluster consisting of two or more nucleons. The constituents of this cluster share most of the energy of the incoming pion, basically the pion rest mass, among each other. In the case of absorption on a two-nucleon cluster, this leads to the back to back emission of the nucleons with approximately equal energy ($\approx$ 70 MeV, half of the pion mass). The removal of the capturing cluster frequently leaves the residual nucleus in a highly excited state from which it decays first through particle emission and later through radiation. The particles emitted by this mechanism are generally of low energy and are emitted isotropically.
Negative pion π^- capture at rest on nuclei for high A, nuclear mass, is dominant over π^- decay "at rest" for low energy pions.

3.2 Hadronic interaction channels: Final state topologies

Let's now discuss the different strong interaction processes a pion can undergo while crossing a target. The pion energy is here assumed in the range $\approx$ [100 MeV - 2 GeV]. Many hadronic interaction channels are available and the pion total cross section can be decomposed in "elastic" and "reaction" channels:

$$\begin{aligned} \sigma_{tot} &= \sigma_{el} + \sigma_{reac} \\ \sigma_{reac} &= \sigma_{inel} + \sigma_{abs} + \sigma_{chex} + \sigma_{\pi prod} \end{aligned} \tag{3.9}$$

The interaction channels in Eq. 3.9 can be listed according to the pion multiplicity in the final state:

(a) *0 π in the final state*:
- **Pion Absorption**, σ_{abs}: it occurs on bound nucleons and it's enhanced near the

Δ-resonance region. Absorption on single nucleons in nuclei is highly suppressed (absorption by a single free nucleons is forbidden by energy conservation), therefore this process should occur on at least two nucleons system:

- 2-body absorption (back-to-back emission)

$$\pi^+(np) \longrightarrow pp \quad \text{BR } 19\% \quad \pi^-(np) \longrightarrow nn$$

- 3-body absorption

$$\pi^+(pnn) \longrightarrow ppn \quad \text{BR } 31\% \quad \pi^-(pnn) \longrightarrow nnn$$

$$\pi^+(ppn) \longrightarrow ppp \quad \text{BR } 12\% \quad \pi^-(ppn) \longrightarrow pnn$$

- Multi-body absorption, e.g. absorption on α cluster

$$\pi^+(ppnn) \longrightarrow pppn \quad \text{BR } 10\% \quad \pi^-(ppnn) \longrightarrow pnnn$$

(b) *1 π in the final state*:
- **Elastic scattering** , σ_{el}, on nucleus/nucleon N, which is left in ground state ("pion kink"):

$$\pi^+ + N \longrightarrow \pi^+ + N$$
$$\pi^- + N \longrightarrow \pi^- + N$$

- **Charge exchange**, σ_{chex}:

- Single Charge Exchange: charged pion converts in a neutral pion

$$\pi^+ + n \longrightarrow \Delta^+ \longrightarrow \pi^0 + p$$
$$\pi^- + p \longrightarrow \Delta^0 \longrightarrow \pi^0 + n$$

- Double Charge Exchange: charged pion converts in a pion with inverted charge

$$\pi^+ + N \longrightarrow \pi^- + nucleons$$
$$\pi^- + N \longrightarrow \pi^+ + nucleons$$

- **Inelastic scattering**, σ_{inel}:

- "Pure" Inelastic scattering: Nucleus excited, low lying bound states are populated
- Inelastic reaction with nucleons knock-out:
  - Nuclear break-up with nucleons and/or fragments knock-out
  - Delta resonance excitation and decay ($E_\pi^{kin} \approx$ 150-200 MeV):

$$\pi^+ + p(target) \longrightarrow \Delta^{++} \longrightarrow p(\text{nucleon knock-out}) + \pi^+$$
$$\pi^+ + n(target) \longrightarrow \Delta^+ \longrightarrow n(\text{nucleon knock-out}) + \pi^+$$
$$\pi^- + p(target) \longrightarrow \Delta^0 \longrightarrow p(\text{nucleon knock-out}) + \pi^-$$
$$\pi^- + n(target) \longrightarrow \Delta^- \longrightarrow n(\text{nucleon knock-out}) + \pi^-$$

- Inelastic products from Final State Interactions (FSI): while the pion comes out from the nucleus, the nucleons produced in its first interaction can experience other successive interactions inside the nucleus and other particles can be emitted (e.g. deuteron, α particles)

(c) $\geq$ *2 π in the final state*:
- **Pion Production**, $\sigma_{\pi prod}$, ($E_{\pi}^{kin} > 500$ MeV):

$$\pi + N \longrightarrow \geq 2\pi + nucleons$$

In Table 3.1 are listed the pion cross sections as a percentage of the total value and the actual values near the peak of the Δ-resonance region for carbon and iron.

	% of Total in C	% of Total in Fe	σ in C	σ in Fe
Total			630 mb	1700 mb
Elastic	35%	40%	210 mb	700 mb
Inelastic	33%	20%	210 mb	360 mb
"True" Absorption	25%	35%	160 mb	600 mb
Single Charge Exchange	7%	5%	45 mb	83 mb

Table 3.1: Summary of π^+ cross sections (σ) in Carbon and Iron for E_{π}^{kin}= 205 MeV. [50] [47]

The pion-nuclear interaction can be separated in three different domains depending on the kinetic energy of the incident pion: low-energy region $0 < E_{\pi}^{kin} \leq 80$ MeV, the Δ-resonance region 80 MeV $< E_{\pi}^{kin} \leq 400$ MeV, high-energy region $E_{\pi}^{kin} > 400$ MeV. In the low-energy region the pion mean free path inside the nucleus is much longer than the distance between nucleons ($\approx$ *O(1 fm)*) and the interaction is weak, so the pion can penetrate deeply in the nucleus. Elastic scattering and (two-body) absorption phenomena play an important role in this region, they can be treated with optical potential.
Moving from low-energy scattering to the Δ-resonance region, the features of pion-nucleus interaction drastically change. The pion mean free path in the nuclear medium is shorter than the average internucleon distance ($\lambda_{\pi \text{ in nucleus}} \leq 1$ fm for $E_{\pi}^{kin} \simeq 180$ MeV), therefore the primary πN interaction takes places at the nuclear surface. The pion-nucleus interaction in this region is dominated by the formation of the Δ particle and its decay inside the nucleus.

There have been several experiments measuring pion-nucleus total cross sections on different nuclei, especially in the Δ resonance energy region, and studying the dependence of the total cross section and the different interaction channels on targets of different mass number A, as shown in Figure 3.6 and Figure 3.7.[44] [45] [46]

The Δ-resonance structure is more prominent in the π-nucleus total cross section σ_{tot} for nuclei with A$\leq$50 as it can be seen on Figure 3.6. The peak energy is shifted downward for increasing nuclear mass number A; the reason is partly kinematic and partly due to the modified propagation of the Δ inside the nucleus. The width of the resonance is more than the natural-decay width of the free particle and it increases with nuclear mass number; it's due to multiple-scattering effects and it reflects also the coupling of the resonance to many-body reaction channels.
For fixed pion energy, the total cross section and the individual channel cross section increase according to a power law for target of increasing mass number, A, as shown in Fig.3.6.

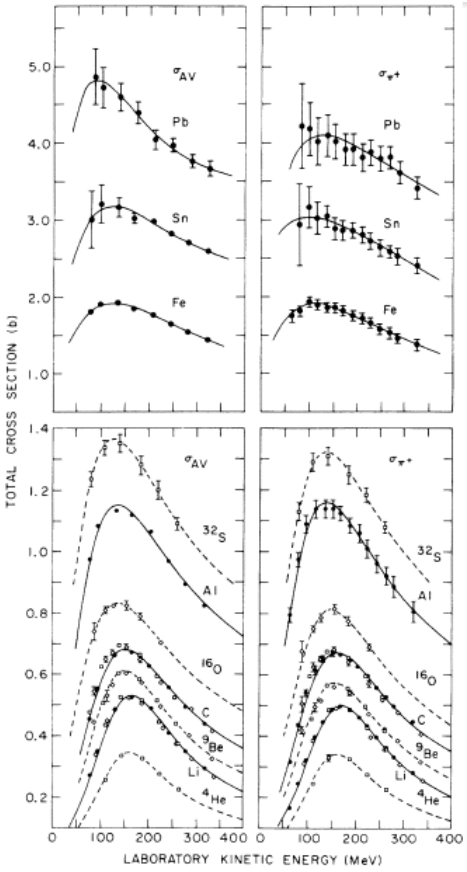

Figure 3.6: Pion-nucleus total cross-sections in the Δ-resonance region for π^+ and π^-. On the left side there are the averaged cross section values, $\sigma_{av}=\frac{(\sigma_{\pi^-}-\sigma_{\pi^+})}{2}$; on the right there are the total cross sections for π^+, σ_{π^+}. The curves correspond to empirical fits to all the data assuming a Breit-Wigner shape. [45]

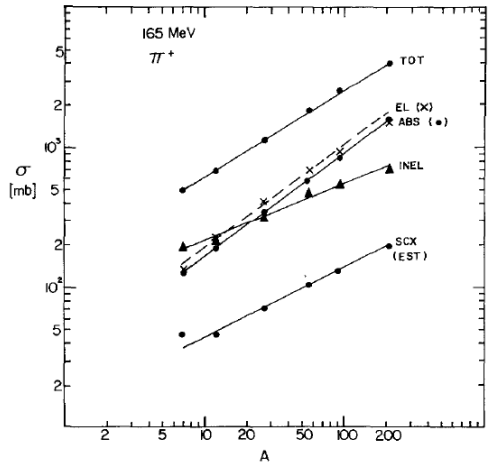

Figure 3.7: Nuclear mass (A) dependance of pion-nucleus interaction cross section for different interaction channels nearby the Δresonance-region.[46]

3.3 Geant4 stand-alone program for pion interactions on Ar

As a first step in the study of pion interaction we proceed to the simulation of pion interactions with different material targets, eventually focusing on Ar, with a Geant4 stand-alone program (Geant4 version 10.1) [54] [55] [56].

Together with Dr.Hans Wenzel (Fermilab - Geant Team) we've developed a Geant4 simulation code for hadronic interactions on different target materials (G4HadStudies).[1]

In the Monte Carlo simulation pions with kinetic energies in the [50 MeV,2 GeV] energy range are sent on a fixed target. In case an interaction happens inside the target thickness, the type of interaction is recorded as well as the secondary particles produced. [2]. Every secondary particle produced in that interaction is put on the stack (G4 Stacking Action) and its Pdg code, position and quadrimomentum are collected.

The Monte Carlo events produced by the Geant4 simulation are then analyzed through a C++ module in Root.[57]

The aim of this calculation of the pion-nucleus total cross section through this simulation is to provide a ***validation of Geant4 models*** for pion interactions [58] in the energy interval of our interest, especially the FTFP_BERT physics list, where the Bertini Cascade model is used for the pion interactions in this energy range, by comparison with available cross section experimental data for several target materials.

The **Bertini model** [59] [60] generates the final state for hadron inelastic scattering on nucleon inside the nucleus and subsequent reinteractions of the first product inside the nucleus (intra-nuclear cascade). [3]The target nucleus is treated as an average nuclear medium, in which the nucleons are assumed to have a Fermi gas momentum distribution. The final state of each collision is sampled according to free-particle cross section data. Clusters of nucleons are considered only in case of pion absorption which requires at least dinucleons. Nuclear effects, i.e. secondaries which can interact with other protons and neutrons inside the nucleus and so on until the last secondaries escape the nucleus or are absorbed, are also taken in account. This model reproduces detailed cross section data for nucleons, pions and kaons in the region below 1 GeV and is expected to do reasonably well in the multi-GeV region.

The comparison of Geant4 pion hadronic cross section has been extended also to the predictions of another MC generator, the **Genie(version 2.8.2)** Montecarlo.
GENIE [62] is a Neutrino Monte Carlo Generator used especially in Neutrino Physics Collaborations. The GENIE model is universal. It handles neutrinos and nuclear targets, and all processes relevant from MeV to PeV energy scales. So it is possible to have information on hadron-nucleus interactions too from Genie. For pion-nucleus in-

[1]Github Repository: https://github.com/hanswenzel/G4HadStudies

[2]Each time an interaction happens it's flagged with a proper value of the variable intType (inelastic pion-nucleus scattering: "pionInelasticScattering" intType= 1, elastic scattering: "hadElasticScattering" int Type= 2 , pion decay in flight and/or at rest: "decay" intType= 3, negative pion capture at rest: "hBertiniCaptureAtRest" intType=4

[3]Since in particle-nuclear collisions the deBroglie wavelength of the incident particle is comparable or shorter than the average intra-nucleon distance, the intra-nuclear cascade model (INC) describes the interactions in terms of particle-particle collisions.

teractions, Genie uses INTRANUKE hA model, which is a simplified INC (intra-nuclear cascade) data-driven model. Each particle has at most 1 interaction as it propagates through residual nucleus. The hA model is tuned on different particles cross section on Fe target data.
I met Prof. S.Dytmann (University of Pittsburgh) who is the main author of all hadron-nucleus interactions in GENIE and, since I was involved in pion-nucleus cross section studies using Geant4 framework, we decided to compare results from Geant4 Bertini Cascade model, Genie hA model and experimental data.

3.3.1 Thin Target Simulation

In the Geant4 stand-alone program (G4HadStudies) we've defined a disk (G4Tubs) as a thin target for pion interaction, see Fig.3.8; we've set the target material (i.e G4_C, G4_LAr...) [61] and dimensions in the input file for the simulation. Pions of fixed energy were shot with their momentum direction perpendicular to the disk surface. In my simulations I generate 10^6 pions (π^+, π^-) of incident kinetic energy E_π^{kin} from 50 MeV to 2 GeV, with 50 MeV energy steps.

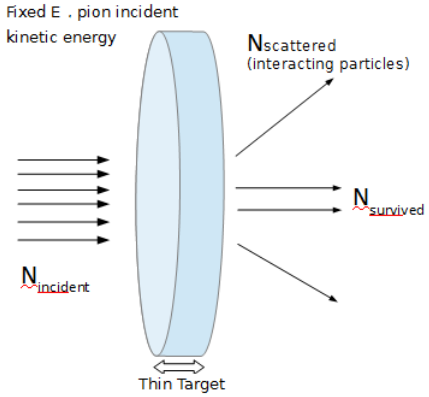

Figure 3.8: Schematic representation of the thin target for pion interactions simulated in my Geant4 stand-alone program.

Using the method described in the previous paragraph and the Bertini Model for hadronic interactions in Geant4 simulation, I've calculated the total, elastic and inelastic cross sections for charged pions on thin targets of different materials (Carbon C, Calcium Ca, Beryllium Be, Lithium Li, Aluminum Al, Iron Fe, ...).

- $\pi^\pm$ - ^{12}C Interactions
  The first comparison is for charged pions π^- **and** π^+ **on Carbon** ^{12}C **target**; cross sections from simulations and experimental data (Clough [44], Allardyce [48], Ashery [47]) are shown in Fig.3.9 and Fig.3.10.

  From the cross section plots in Fig.3.9 and 3.10, we see there is good agreement with data (total, elastic and reaction cross sections) and Geant4 predictions for π^- and π^+ on Carbon target both in Delta resonance region and at high energies ($>$ 500 MeV). Genie predictions appear to give similar results as Geant4 in the Delta resonace region, while for higher energies they show some particular features ("bumps") around 500 MeV and 900MeV. These should be due to the excitation

of higher resonances in the hA model. Actually we could not conclude these resonances really affect the cross section shape, as it appears from Genie predictions, since the experimental data have a smoother distribution over energy ($E_\pi^{kin} > 500$ MeV) and they're well overlapped by the Geant4 prediction cross section shape. The cross section is definitely enhanced in the Delta resonance region: for pions in Carbon the total cross section close to 200 MeV is $\approx$ 700 mb, which is about twice the value for energies far from the resonance excitation region, i.e $E_\pi^{kin} >$ 500 MeV total cross section $\approx$ 300 mb.

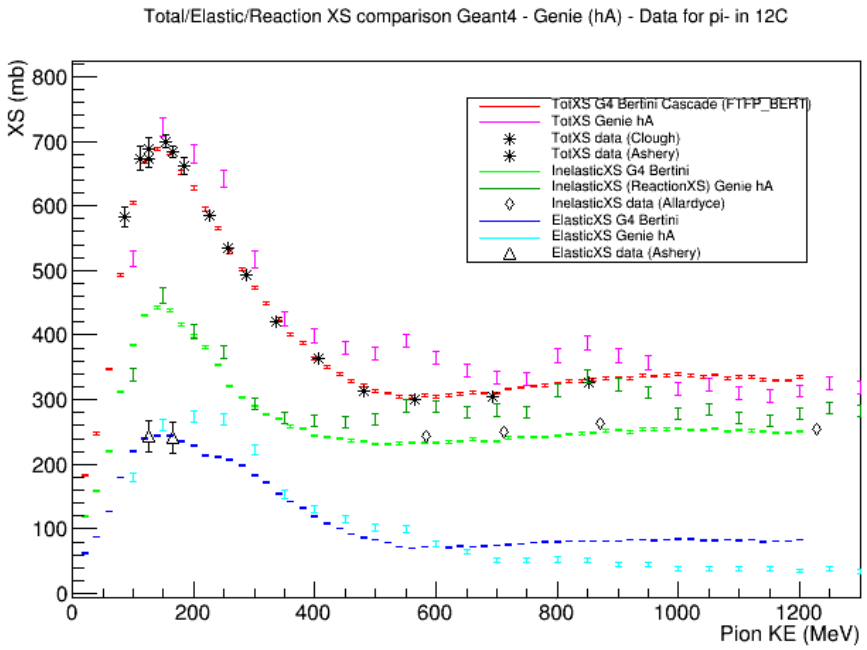

Figure 3.9: Total, elastic and reaction cross section for π^- on Carbon ^{12}C within 50 MeV - 1.2 GeV pion kinetic energy range. Comparison of cross section results from Geant4 thin target simulation (Bertini cascade model), from Genie simulation (hA model) and experimental data [44] [47] [48].

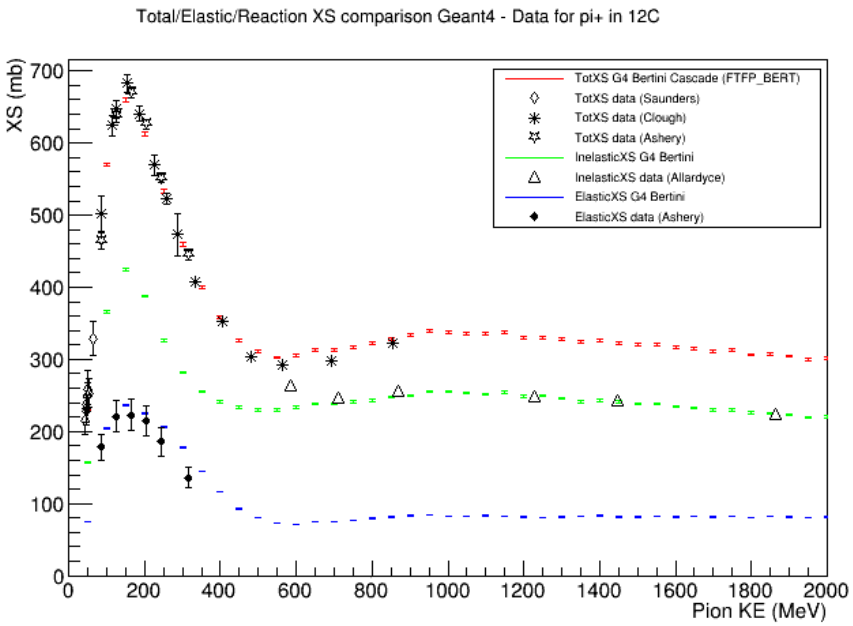

Figure 3.10: Total, elastic and reaction cross section for π^+ on Carbon ^{12}C within 50 MeV - 2.0 GeV pion kinetic energy range. Comparison of cross section results from Geant4 thin target simulation (Bertini cascade model) and experimental data [44] [47] [48][49].

- $\pi^{\pm}$ - ^{56}Fe Interactions
  Since the Genie model is tuned on Fe cross section data, the same comparison has been performed for π^- **and** π^+ **on** ^{56}Fe **target** for energies around the Delta resonance region (E=50 - 350 MeV). In Fig.3.11 and 3.12 the results are shown.

  The cross section results are interesting. Basically, Genie well reproduces the total and elastic cross section for both π^- both π^+ on Iron in 50 MeV - 350 MeV region, as expected since it was tuned on these experimental data. Geant predictions instead appear to underestimate the total cross section of about 600 mb compared to the experimental data. Probably it is due to an unrealistic reproduction in Geant4 (Bertini model) of the elastic channel interaction probability for high mass nuclei. [4]

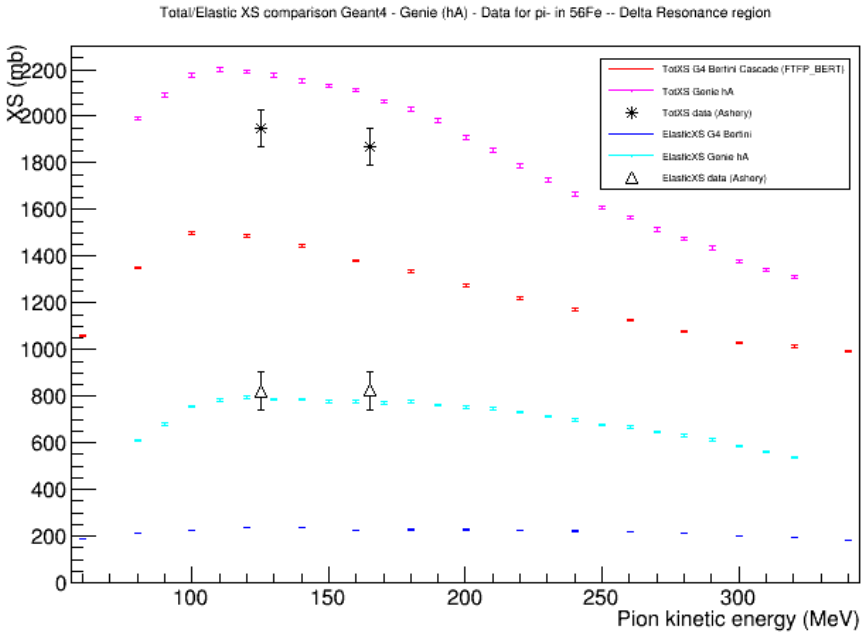

Figure 3.11: Total and elastic cross section for π^- on Iron ^{56}Fe within 50 MeV - 350 MeV pion kinetic energy range. Comparison of cross section results from Geant4 thin target simulation (Bertini cascade model), from Genie simulation (hA model) and experimental data [47].

[4] For high mass nuclei maybe the treatment of the nucleus as an uniform medium fails and/or the elastic interaction probability has to take in account for multi-body collisions, not only single nucleon subsequent collisions as Bertini model does.

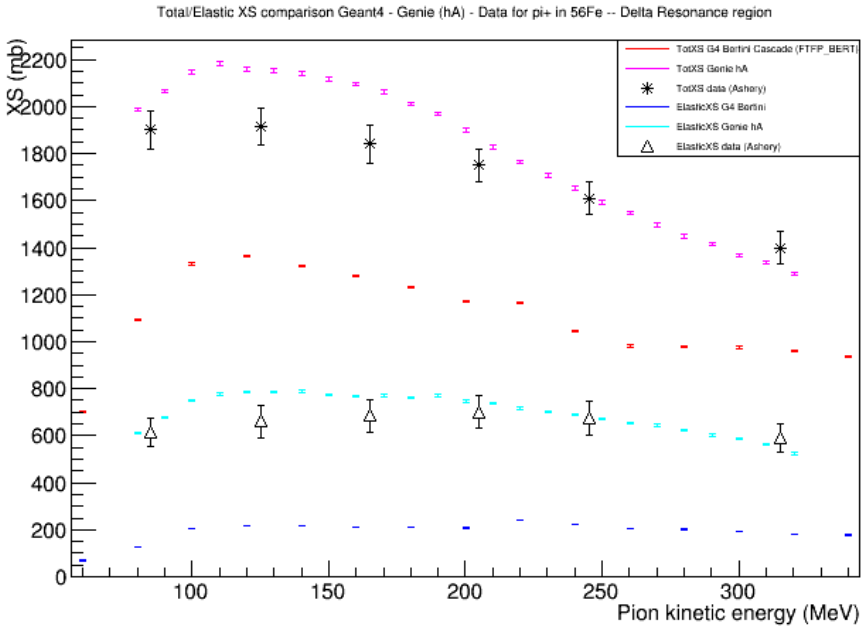

Figure 3.12: Total and elastic cross section for π^+ on Iron ^{56}Fe within 50 MeV - 350 MeV pion kinetic energy range. Comparison of cross section results from Geant4 thin target simulation (Bertini cascade model), from Genie simulation (hA model) and experimental data [47].

- $\pi^{\pm}$ - ^{40}Ca Interactions
  We're interested in charged pions cross sections on Ar, which has nuclear mass A=40. There are no experimental cross section data on Ar target. However some data are available for π interaction on ^{40}Ca, a nucleus of same nuclear mass as Ar.
  The simulation of π - ^{40}Ca interaction has been performed to provide a closer term of comparison in view of the π - ^{40}Ar studies.

  Fig.3.13 shows the expected total and reaction cross sections for π^- on Calcium from Geant4 (Bertini model) and Genie (hA model). There are also superimposed the available experimental data of reaction cross section, from [48], for E $>$ 500 MeV. We can observe that Geant4 and Genie predictions for E$>$500 MeV quite overlap and well reproduce at least the few reaction cross section experimental data we have from literature. Instead for energies nearby Delta resonance region, Genie and Geant4 predictions are quite different: Genie model appears to predict a higher cross section ($\approx$ 1600 mb total cross section) than Geant ($\approx$ 1300 mb) at the peak and the Delta resonance peak is shifted to a bit higher energy than the same in Geant4 prediction. Actually we don't have experimental data in this region to validate one model or another.
  This reinforces the need of experimental data on Ar, since the available models on nuclei of similar nuclear mass, as Ca, seem not completely appropriate.

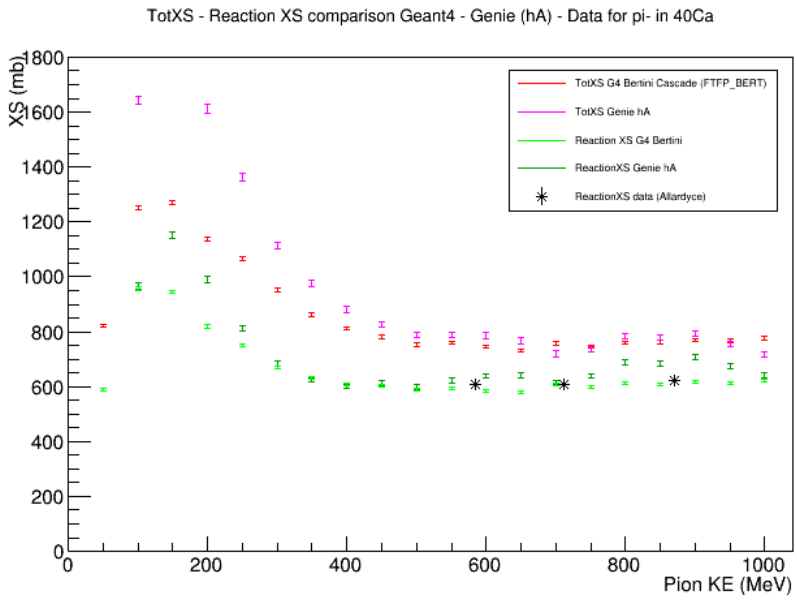

Figure 3.13: Total, elastic and reaction cross section for π^- on Calcium ^{40}Ca within 50 MeV - 1.0 GeV pion kinetic energy range. Comparison of cross section results from Geant4 thin target simulation (Bertini cascade model), from Genie simulation (hA model) and experimental data [48].

- $\pi^{\pm}$ - ^{40}Ar Interactions
  For the Geant4 stand-alone simulation code, we've used Bertini cascade for **charged pion interactions in LAr** as well as Intranuke hA for the simulation with Genie. In Fig.3.14 are shown total and reaction cross section plots for π^- on Ar (A=40) from Genie hA model and from Geant4 thin target simulation with G4HadStudies code.

  As already seen for Calcium, the Delta resonance region cross section is more enhanced in the Genie hA model than in the Geant4 Bertini one (total cross section at peak: 1900 mb Genie hA model, 1300 mb Geant4 Bertini model), while for E>500 MeV they both give similar values ($\approx$ 800 mb total cross section).
  These "expected cross section" plots would be reference values to compare with the first charged pions on Ar cross section measurements from LArIAT experiment, to check efficiency and acceptance of our system and the cross section calculation method. When we'll produce trusty cross section measurements for pions in LAr that could cover the whole 50 MeV - 2 GeV region, they could be used for Geant4 and Genie model tuning and/or validation.

  In the plots in Fig.3.15 and 3.16, the interaction cross section dependence on energy for π^- and π^+ on LAr thin target produced through Geant4 stand-alone program (G4HadStudies) is shown.
  In my simulation and analysis code I've also tried to find selection criteria to discriminate among the several reaction channels (absorption, charge exchange, inelastic scattering, pion production), which are plotted on the following figures too. The selection criteria were mainly based on the multiplicity of the secondary particles produced:

  - Absorption channel: no pions in the final state neither charged pions π^-, π^+ nor neutral pions π^0
  - Single charge exchange: 1 π^0 and no charged pions in the final state
  - Double charge exchange: 1 charged pion of the opposite sign of the incoming pion and no π^0 in the final state
  - Inelastic: 1 charged pion in the final state, corresponding to the incoming pion, and no π^0
  - Pion production: all the rest (more than 1 π^0 or 1 π^0 and charged pions or no π^0 and more than 1 charged pions...)

  From the plots in Fig.3.15 and 3.16 we can observe that the main contribution to the total cross section appears to come from Reaction channels, i.e $\sigma_{react} \approx 3 * \sigma_{el}$ all over the energy range.
  At energies near the Δ resonance region the Absorption channel is dominant while for higher energies the Pion Production channel gives the main contribution to the interaction cross section.
  In Table 3.2 there are the percentages of the different interaction channels for π^+ in the Δ resonance region (E_{π}^{kin} =200 MeV) obtained from the LAr thin target simulation; we can see the reaction channels have a reasonable agreement with the percentages for π^+ on Carbon and Iron from the experimental data shown in Tab.3.1 at the same energy. Instead the percentage over the total of the elastic cross section is strongly less than for Carbon and Iron, so probably there is not a completely correct representation of the hadronic elastic interaction for pions in the Geant4 MC framework (and in Genie too).

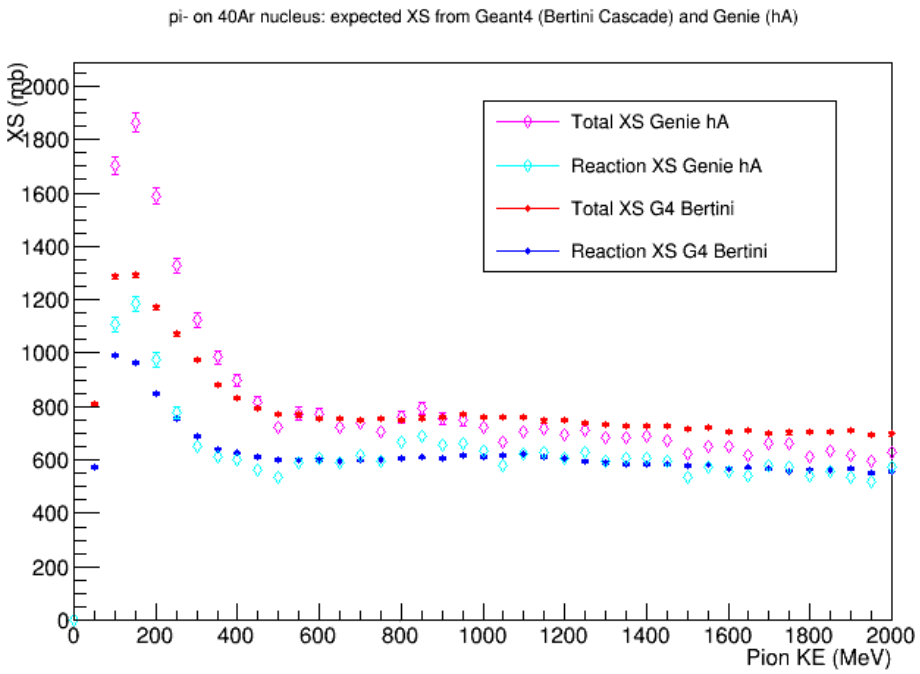

Figure 3.14: Total and reaction cross section for π^- on (Liquid) Argon ^{40}Ar within 50 MeV - 2.0 GeV pion kinetic energy range. Comparison of cross section results from Geant4 thin target simulation (Bertini cascade model) and from Genie simulation (hA model).

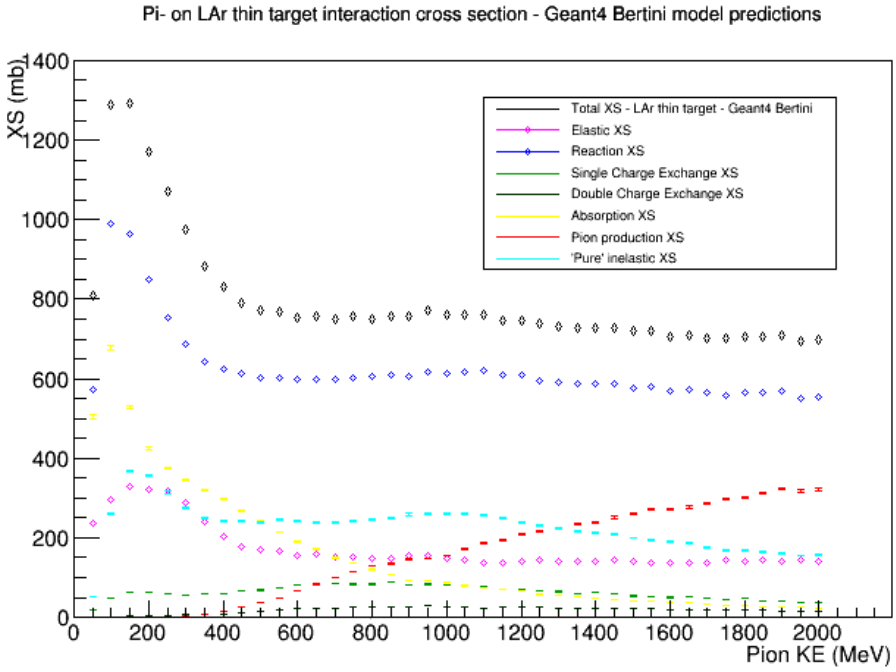

Figure 3.15: Interaction cross section (several channels) for π^- on (Liquid) Argon ^{40}Ar within 50 MeV - 2.0 GeV pion kinetic energy range from Geant4 thin target simulation (Bertini cascade model).

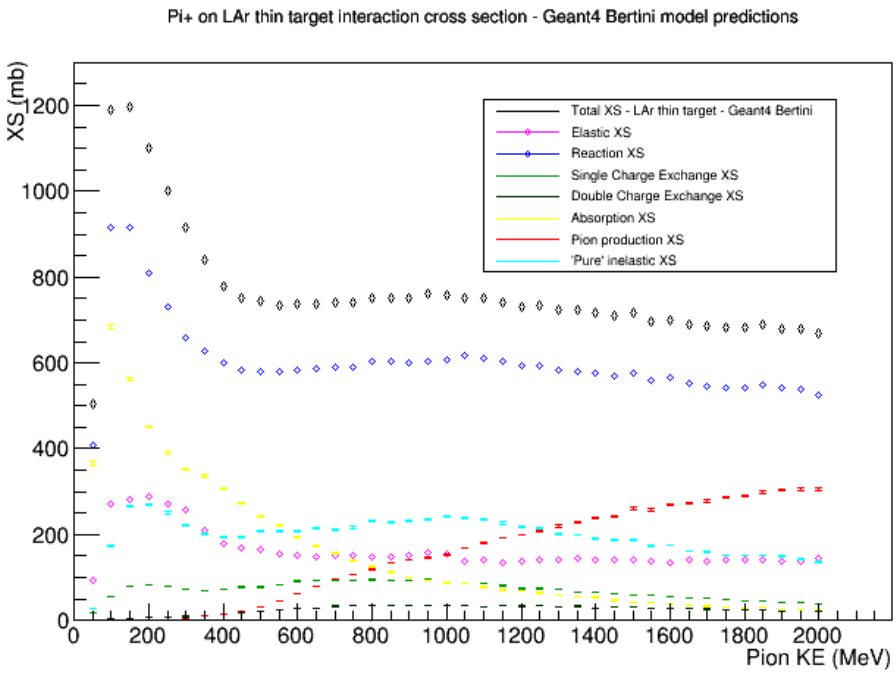

Figure 3.16: Interaction cross section (several channels) for π^+ on (Liquid) Argon ^{40}Ar within 50 MeV - 2.0 GeV pion kinetic energy range from Geant4 thin target simulation (Bertini cascade model).

Geant4 (Thin target)	% of Total in LAr	σ in LAr
Total		1105 mb
Elastic	25%	280 mb
Inelastic	25%	276 mb
Absorption	38%	450 mb
SCEX	7%	80 mb

Table 3.2: Summary of π^+ cross sections (σ) in LAr for E_π^{kin}= 200 MeV fro Geant4 thin target predictions.

Another way to analyze the pion-nucleus interaction cross section is to consider a fixed kinetic energy (or very short energy range), plot the experimental data for different target materials and **extrapolate the cross section expected for the Ar target**, at that energy. In this way we can also compare Geant4 and Genie pion cross sections predictions for different mediums in those energy ranges.
The total and reaction cross section vs nuclear mass A, comparison plots for two energy ranges for π^-:

- Δ resonance region (130 - 150 MeV) (See Fig.3.17 and 3.18 for π^-)
- "Flat" high energy region (for this region, I've chosen 900 MeV energy value to make the comparisons to be far from the resonance region) (See Fig.3.19 and 3.20 for π^-)

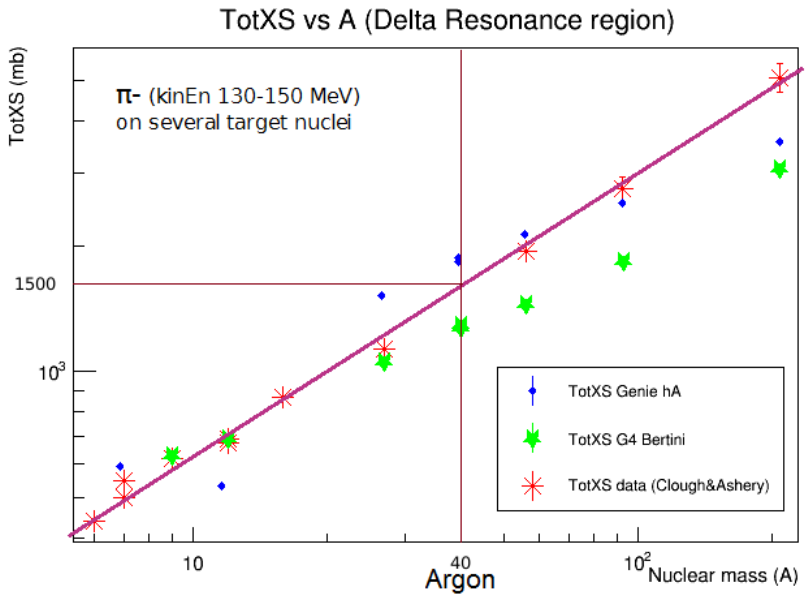

Figure 3.17: Total π^- cross section vs Nuclear Mass (A) in the Δ resonance energy region. Geant4 and Genie predictions and experimental data [44] [47]. The error bars for Geant and Genie cross section predictions are very small and may be hidden by the markers dimensions.

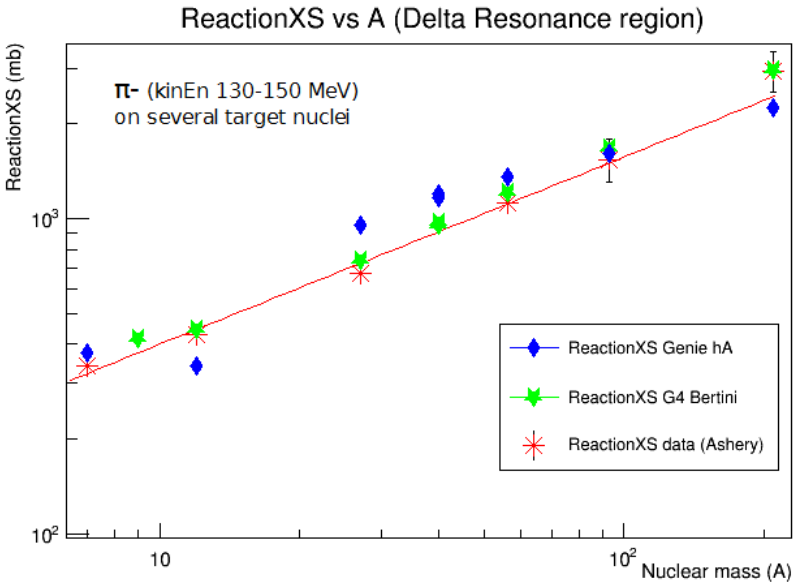

Figure 3.18: Reaction π^- cross section vs Nuclear Mass (A) in the Δ resonance energy region. Geant4 and Genie predictions and experimental data [47]. The error bars for Geant and Genie cross section predictions are very small and may be hidden by the markers dimensions.

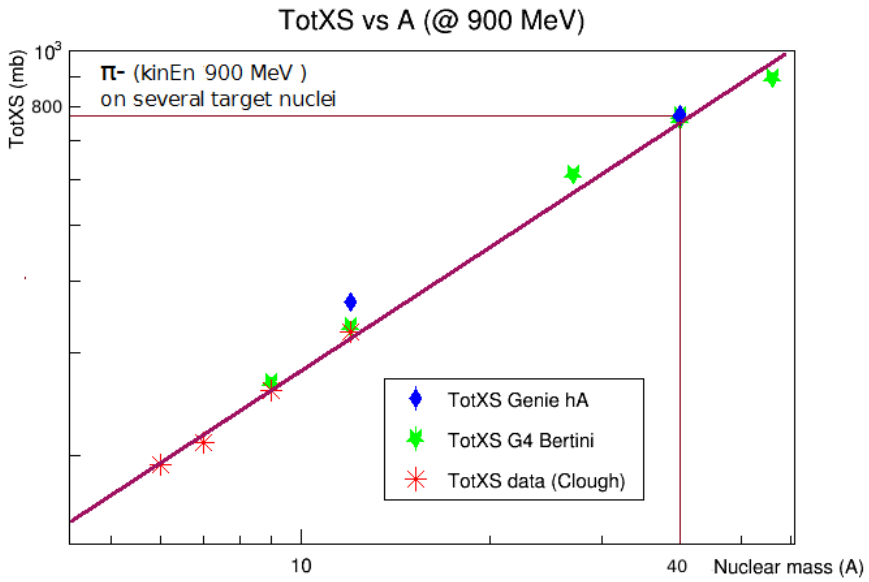

Figure 3.19: Total π^- cross section vs Nuclear Mass (A) at 900 MeV. Geant4 and Genie predictions and experimental data [44].

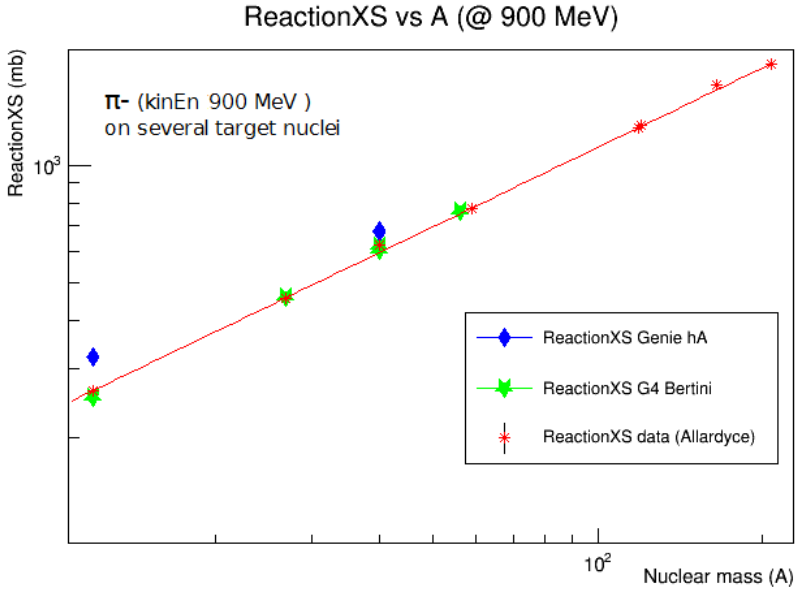

Figure 3.20: Reaction π^- cross section vs Nuclear Mass (A) at 900 MeV. Geant4 and Genie predictions and experimental data [48].

So we can extrapolate the expected total cross section in LAr, A=40, from the plots of the total cross section experimental data for pions on different targets for a fixed energy.
For π^-, see Fig.3.17 and 3.19:

- $\sigma_{tot} \approx 1500$ mb in Δ resonance energy region (130-150 MeV)
- $\sigma_{tot} \approx 800$ mb in "Flat" region at 900 MeV

Using this approach, the total cross section we expect for π^- in LAr in Δ resonance energy region should be a bit higher than the Geant4 Bertini prediction (≈ 1300 mb) and lower than the Genie prediction (≈ 1900 mb), see Fig.3.14.

We fit the Reaction cross section to the data points in the plots in Fig.3.18 and 3.20 with the empirical equation, suggested in Allardyce paper [48]:

$$\sigma_{reac} = CA^n \tag{3.10}$$

The fit results (parameter n) obtained for π^- Reaction cross section vs nuclear mass, A, in the two energy ranges previously described are listed in Table 3.3.

Energy region	Reaction cs	parameter n
Δ resonance 130- 150 MeV	from Data [47]	0.595 $\pm$ 0.033
Δ resonance 130- 150 MeV	from Geant4	0.605 $\pm$ 0.002
Δ resonance 130- 150 MeV	from Genie	0.546 $\pm$ 0.002
900 MeV	from Data [48]	0.677 $\pm$ 0.007
900 MeV	from Geant4	0.721 $\pm$ 0.003
900 MeV	from Genie	0.612 $\pm$ 0.003

Table 3.3: Table of the fit results for Reaction cross section vs A using the empirical formula in Eq. 3.10, for experimental cross section data [47] [48] and Geant4 and Genie cross section predictions.

We see there is a reasonable agreement among Reaction cross section data and Geant4 and Genie predictions; while there isn't such a good agreement for the total cross section; as previously said, it could be due to the model used in Geant4 and Genie to simulate hadronic elastic pion interactions that does not well reproduce the real interaction process.

3.3.2 Thick Target Simulation: LArTPC simplified geometry

After having studied the main features of the pion interaction in thin targets, the next and main task of the MC study is to extend it to the thick LAr target case, the LArIAT TPC geometry, developing a dedicated simulation code (G4HadStudiesLArTPC).[5]
Dimensions ans density of the target correspond to the LArIAT TPC active volume, so that the MC result with the thick Ar target here reported will provide a first indication on the expected behavior of the pion cross section from the LArIAT measurements.
A box (G4Box) of 40 cm height x 47 cm width x 90 cm length (thickness along beam

[5]Github Repository: https://github.com/inutini/G4HadStudiesLArTPC

axis) corresponds to the LAr active volume inside the TPC, see Fig.3.21.
The FTFP_BERT physics list and Bertini cascade model for hadronic interactions simulation in Geant4 has been selected.

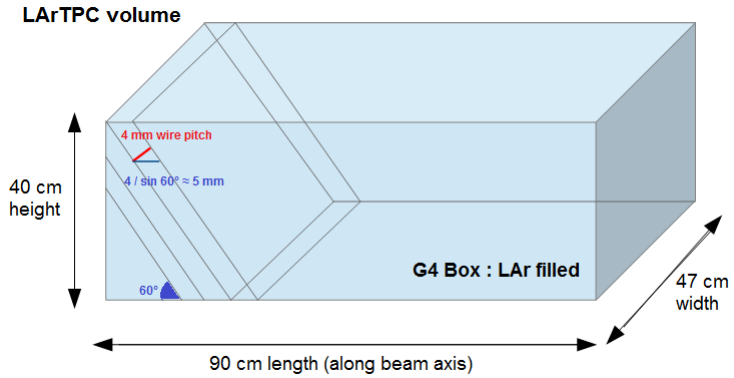

Figure 3.21: Schematic representation of the simplified LArTPC target for pion interactions simulated in my Geant4 stand-alone program.

We estimated the interaction probability inside the whole target - TPC volume through the relative fraction of interactions bin by bin in incident kinetic energy.

In Fig.3.22 and 3.23 are shown stacked histograms in which is plotted the fraction of pions that experience an hadronic interaction (with different channels displayed) or not, normalized to the total number of incident particles shoot for each fixed initial kinetic energy (each bin corresponds to 50 MeV steps, total energy range 50 MeV - 2 GeV).
For example, for π^- with 250 MeV incident kinetic energy, corresponding to $\approx$ 360 MeV/c incident momentum [6], only 10% of these pions would cross all the TPC volume without experiencing an interaction; 20% of them would undergo elastic scattering on nuclei and 30% of them would be absorbed.
We see that pions with initial kinetic energy higher than 200 MeV are very likely to interact at least once in the whole TPC volume (80 - 90 % of them experience an interaction). Low energy pions ($<$ 150 MeV) while crossing the LAr volume deposit more energy and tend to stop quite soon (before half of the TPC thickness, e.g for a 150 MeV incident π its stopping range is almost 40 cm), sometimes before having experienced an hadronic interaction; at that point they could decay (or be captured by the nuclei, for π^-) while at rest.

For the thin target MC cross section results, the pion mean free path for hadronic interactions in LAr is expected to be less than the TPC thickness (90 cm) in the whole energy range from 50 MeV to 2 GeV, from Eq.3.4, so most of the pions will experience at least one interaction in the volume:

$$\begin{aligned} \lambda(E_\pi^{kin} = 130 - 150 MeV) &\approx 32 cm (\Delta \text{ resonance region}) \\ \lambda(E_\pi^{kin} = 900 MeV) &\approx 60 cm \end{aligned} \tag{3.11}$$

[6] The relativistic relation between total energy and momentum:

$$E = \sqrt{p^2c^2 + m^2c^4}$$

E=mγ c^2, E_{kin} = m(γ-1) c^2 , where m is the rest mass of the particle and γ is its cinematic parameter. For a charged pion: m = 139.57 MeV/c^2

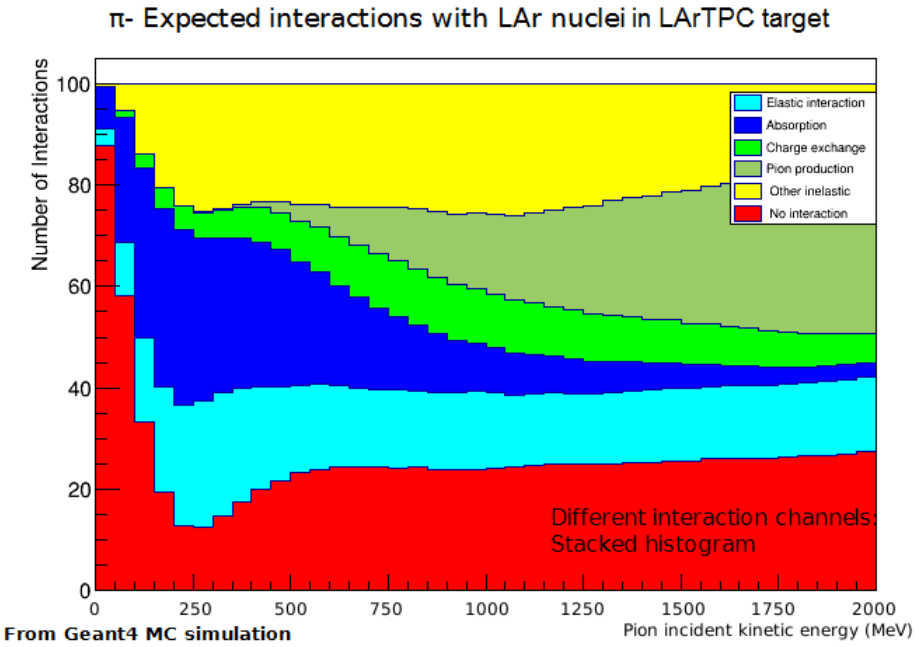

Figure 3.22: π^- expected interactions in LArTPC volume vs pion initial kinetic energy - Stacked histogram (from Geant4 thick target simulation).

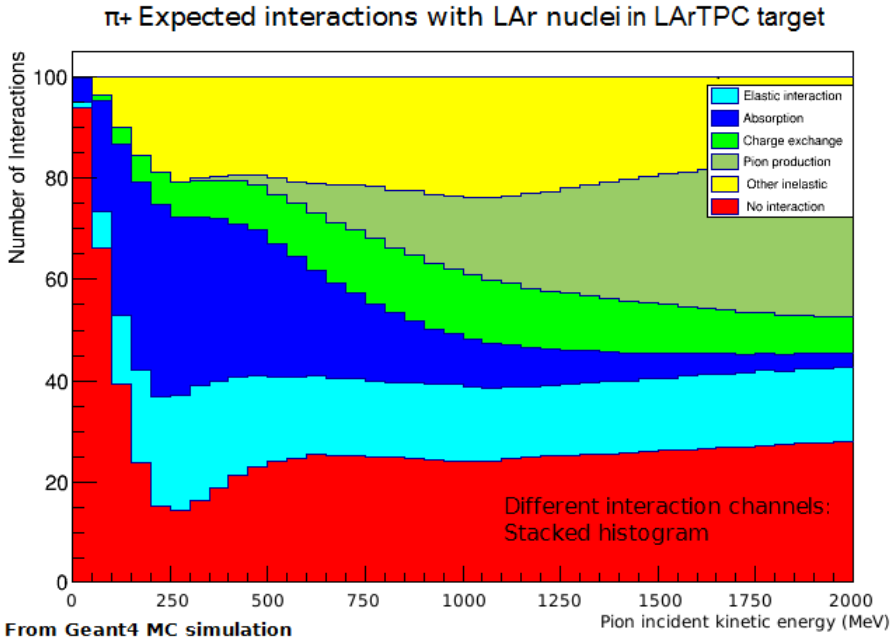

Figure 3.23: π^+ expected interactions in LArTPC volume vs pion initial kinetic energy - Stacked histogram (from Geant4 thick target simulation).

To estimate the pion cross section on Ar from the data in the thick target TPC volume we developed the method described below.
I've called this approach **"Sliced TPC"**. It makes use of the fine granularity and of the high resolution (spatial and calorimetric) of the LArTPC.
The two wire planes of the TPC are composed by 240 wires oriented at +/- 60° at 4 mm distance. Each wire thus collects signals ($\propto$ energy released) in a 60° inclined 4 mm thin slab of Liquid Ar. The TPC depth is thus geometrical sliced in 240 adjacent thin slabs viewed by either the collection or the induction plane.
It is rather "natural" to subdivide the TPC volume in 240 slices of Δx = 4 mm/sin(60°) $\approx$ 5 mm thickness along the x axis, i.e. direction of the incident particle (pions).
This thick target simulation is performed "at particle level", i.e. no other detector features are taken into account and simulated, except for the slices geometry in the LAr TPC volume, that allows to apply for each slice the cross section calculation for a thin target (see Fig.3.8).

To do so however we should consider first that the pion kinetic energy at the interaction point is different (lower) from the initial kinetic energy due to loss of energy via collisions (ionization/excitation) with LAr atoms while crossing the medium.
To take this effect in account I applied the Bethe-Bloch energy loss formula, see Eq.3.8, to estimate the energy deposition along the track. Since the particle slows down and changes its γ and β values in the Bethe-Bloch formula while crossing the medium, I've used this information to evaluate the expected $\frac{dE}{dx}$ (x is the coordinate along the beam direction - TPC thickess) step by step (slice by slice). [7]The kinetic energy of the particle after crossing the n-th slice is:

$$E_n^{kin} = E_{inc}^{kin} - \Sigma_{i=1}^{n}(\frac{dE}{dx})_i \Delta x$$

At each step/slice the MC thus returns the kinetic energy of the pion entering the slice and the information if (or not) an interaction occurred in the slice.

In my analysis code I book two histograms in energy h_N_{inc} and h_N_{surv} with the energy range subdivided in 50 MeV bins. When a pion enters the TPC h_N_{inc} is filled multiple times, once per slice with the current kinetic energy of the pion crossing that slice. h_N_{surv} is filled whenever a particle hitting a slice crosses that without interacting. For each incident particle, the process of filling the histograms is repeated until the particle either exits the last slice of the TPC or "disappears" in one slice (hadronic interaction or decay/ capture at rest). In particular, in case an hadronic interaction has happened at a slice with kinetic energy E_i^{kin}, a count is added to the current bin of h_N_{inc}, but no counts are added to the same bin of h_N_{surv}. In case of a decay in flight or a stopping particle in a slice, a count is added to the bin of h_N_{inc} and one count is added to the bin of h_N_{surv}, since the particle has not experienced a hadronic interaction but is"disappeared" as primary particle track.

Then the ratio $\frac{N_{surv}}{N_{inc}}$ for each energy bin ($\frac{N_{surv}}{N_{inc}}(E_i)$ is evaluated. Then, using Eq.3.7 for a target thickness Δx= 1 cm (two slices), the pion cross section $\sigma_{tot}(E)$ is finally obtained.
The statistical error for the cross section for each kinetic energy takes in account two contributions: ΔN_{inc} and ΔN_{surv}. The statistical error on the total cross section, from Eq.3.7, thus becomes:

[7]The Geant4 simulation code (G4HadStudiesLArTPC) uses G4Stacking action, that collects the informations of the secondary particles produced but does not collect the track informations (energy deposit and position) step by step, which is done instead by the G4Step action. This is the reason why I've evaluated the energy deposition along the track using the Bethe-Bloch formula directly.

$$\sigma_{tot} = ln(\frac{N_{inc}}{N_{surv}})\frac{1}{Nz}$$
$$\Delta\sigma^2_{tot} = \frac{1}{(Nz)^2}[(\frac{\Delta N_{inc}}{N_{inc}})^2 + (\frac{\Delta N_{surv}}{N_{surv}})^2] \quad (3.12)$$

N_{inc} and N_{surv} counts for each bin of the histograms previously described follow a multinomial distribution. The number of incident particles N_{inc} for each energy can be high enough (it depends on the tertiary beam intensity) for each energy bin; therefore we've seen the number of particles that cross the whole TPC volume without experiencing an hadronic interaction N_{surv} would be very low compared to the incident flux. We find ourselves in the Poisson distribution limit for N_{inc} and N_{surv}; this is the reason why I've assumed a Poisson statistical error on N_{inc} and N_{surv} in Eq.3.12.

Then I've compared the cross section dependence on pion kinetic energy (at interaction point) obtained with this "Sliced TPC" approach with the same plot obtained for pions with fixed incident kinetic energies on a LAr thin target (see previous paragraph); both of these results come from Geant4 simulation with Bertini model for hadronic interactions.

In Fig.3.24 there is a schematic representation of this "Sliced TPC" method.

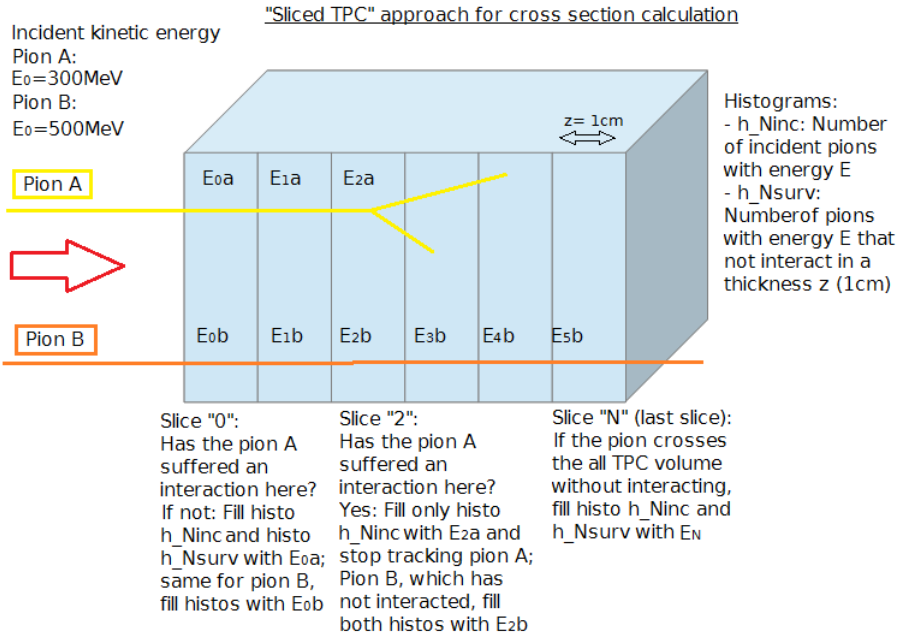

Figure 3.24: Schematic representation of "Sliced TPC" approach to calculate pion interaction cross section (see Eq.3.6) from LArTPC tracks.

The kinetic energy of the incident π^+ and π^- in my simulation was sorted under a normalized distribution (Pdf) in two energy ranges corresponding to two beam settings of the LArIAT tertiary beam (2×10^5 pion generated in total, using GPS, General Particle Source, in Geant4 to generate the incoming pions according to the predicted tertiary beam profile). Fig.3.25 shows the two normalized kinetic energy distributions for π^- from the LArIAT tertiary beam profile, that have been used for sorting the incident π^- kinetic energy in the simulation.

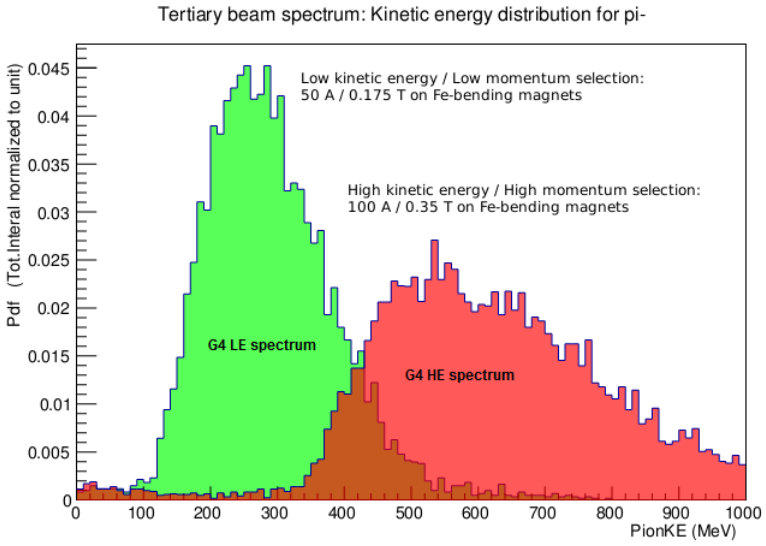

Figure 3.25: π^- Incident kinetic energy distributions in the two energy ranges corresponding to two beam settings of the LArIAT tertiary beam. (Low Energy: - 50 A/ 0.175 T on Fe-bending magnets. High Energy: - 100 A/ 0.35 T.)

The cross section results of my simulation for π^+ and π^- in these two energy ranges applying the "Sliced TPC" approach are shown in Fig.3.26 and Fig.3.27.
Here I've used 1 cm thickness for the slices and 50 MeV energy bins for h_N_{inc} and h_N_{surv} histograms.
The statistical error we can obtain with this energy step selection is: $\frac{\Delta\sigma_{tot}}{\sigma_{tot}} \approx$ 1 - 5 % on average.

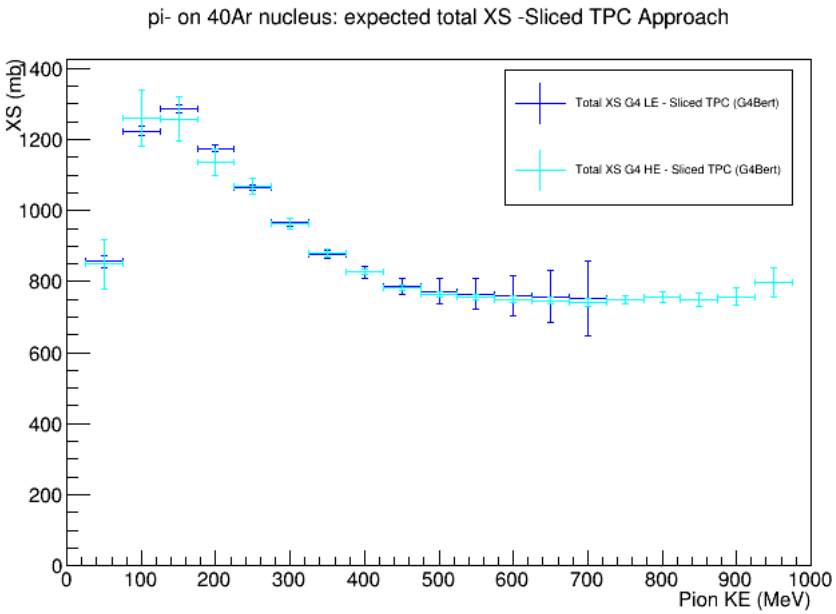

Figure 3.26: π^- Total cross section kinetic energy dependence from Geant4 MC simulation for the two energy ranges obtained applying the "Sliced TPC" approach to the LArTPC thick target. The values of energy in the plot correspond to the pion kinetic energy at the interaction point in the TPC volume. Energy spacing: 50 MeV.

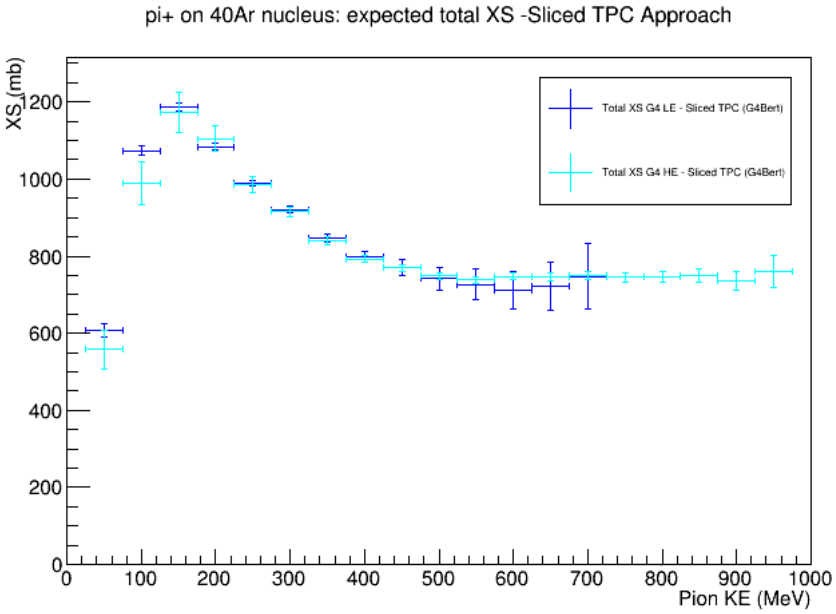

Figure 3.27: π^+ Total cross section kinetic energy dependence from Geant4 MC simulation for the two energy ranges obtained applying the "Sliced TPC" approach to the LArTPC thick target. The values of energy in the plot correspond to the pion kinetic energy at the interaction point in the TPC volume. Energy spacing: 50 MeV.

The results for the total cross section calculated with the "Sliced TPC" approach are compared with the values obtained for LAr "thin target" simulations with Geant4 and with Genie in Fig.3.28.
The cross section values calculated with the thick target method well reproduces the thin target predictions (in Geant4 framework).

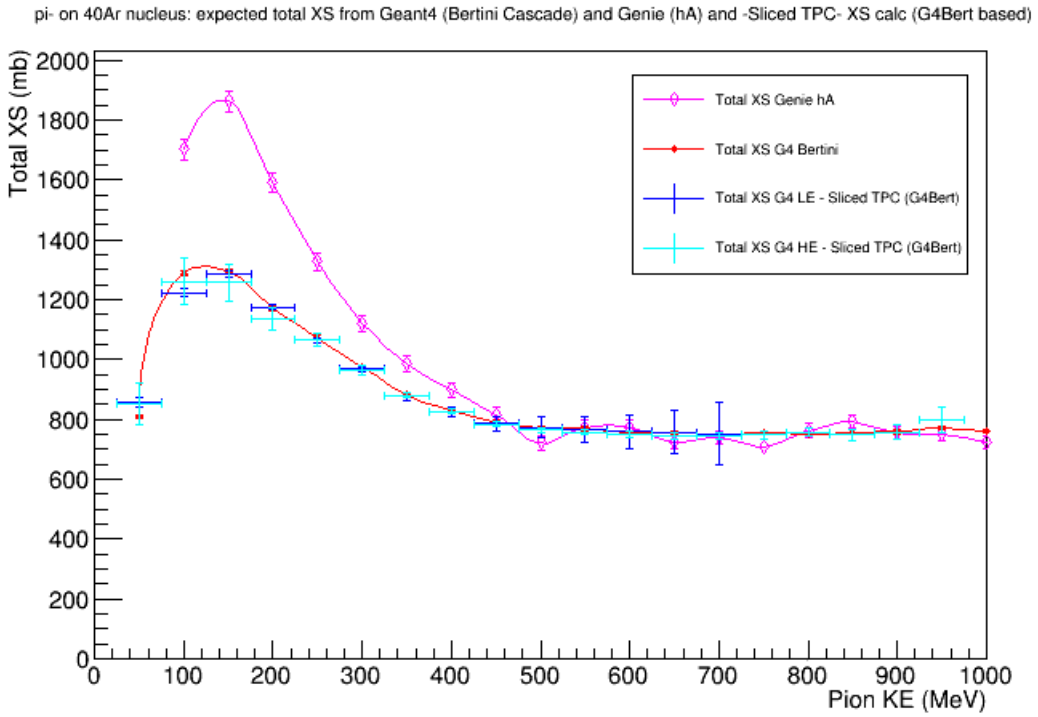

Figure 3.28: π^- Total cross section kinetic energy dependence from MC simulations: comparison towards Geant4 and Genie predictions for a LAr thin target and extrapolated cross section with "Sliced TPC" approach in a Geant4 Bertini based simulation of the LArTPC thick target.

In Table 3.4 there is a summary of the percentages over the total number of incident pions of the different processes (hadronic interactions, decays, π^- capture at rest...) that can happen at $\pi^\pm$ in the LArTPC volume in the energy ranges of the LArIAT tertiary beam.
The reaction channel is dominant towards the elastic scattering in the two energy ranges for both charged pions.
Pions from the low energy beam have a higher percentage of decays, since they can both decay in flight but they can stop shortly in LAr volume and decay at rest too. However for low energy π^- the capture process is dominant if compared with the decay.

In Fig.3.29 are shown the histograms (50 MeV energy bins) of the processes experienced by π^- for different initial kinetic energies (Low energy π^- beam spectrum) and in Fig.3.30 the same histograms are filled with the evaluated energy at the "interaction" point for these pions.
From Fig.3.29 we can see that π^- within this initial kinetic energy are most likely to experience an hadronic interaction while crossing the LAr volume.
However part of π^- with initial kinetic energy $E^{in}_{kin} \leq 250$ MeV tend to slow down and are more likely to be captured by Ar nuclei than to decay. The kinetic energy of a π^- that experience a "capture at rest" process is actually concentrated in the first bin, as shown in Fig.3.30.
The decay process for π^- is slightly more likely for pions in flight, as we can see in Fig.3.30, in which the energy spectrum of the effective kinetic energy of pions that experience a decay is enhanced more around 200 MeV than at lower energies.

	% Survived	% Elastic Sc.	% Reaction	% Decays	% π^- capture
π^- LE	8.6%	22%	60%	2.1%	6.7%
π^- HE	21%	17%	59%	1.3%	1.3%
π^+ LE	10%	20%	60%	9.4%	//
π^+ HE	22%	16%	59%	2.8%	//

Table 3.4: Expected $\pi^\pm$ percentages of hadronic interactions (Elastic scattering and Reaction channel), decays and π^- captures experienced by the incoming pions in the LArTPC volume for different energy ranges. (from Geant4 MC simulations)

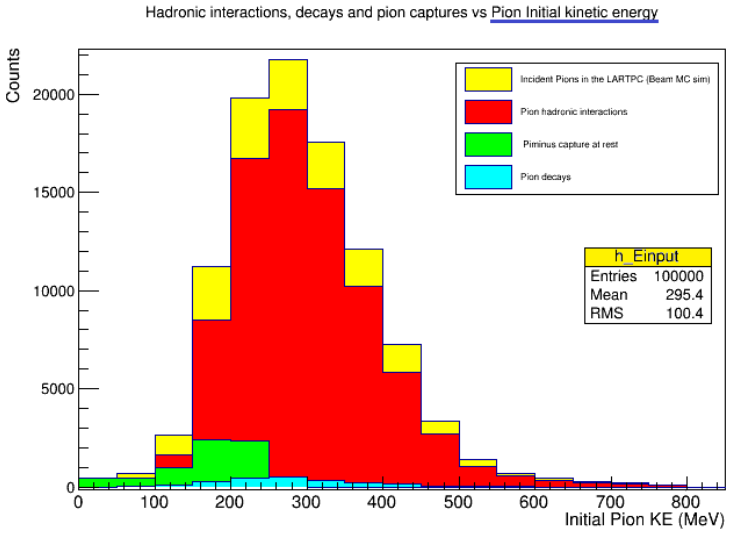

Figure 3.29: Low energy π^- beam spectrum. Distribution of incident, hadronic interacting, decaying and captured at rest pions in the LArTPC volume vs their initial (incident) kinetic energy E_{kin}^{in}. (Geant4 MC simulation)

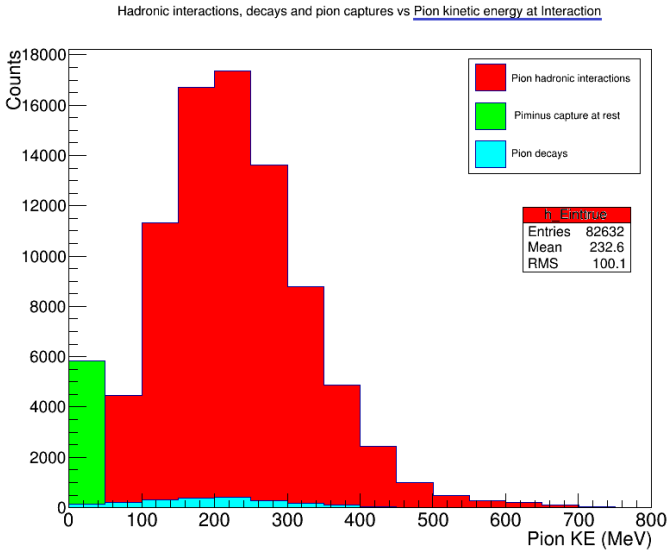

Figure 3.30: Low energy π^- beam spectrum. Distribution of hadronic interacting, decaying and captured at rest pions in the LArTPC volume vs their kinetic energy at the "interaction" point E_{kin}. (Geant4 MC simulation)

In conclusion the main results of my MC analysis are reported in Fig.3.26 and Fig.3.27.
These are the predictions for charged pion (π^+, π^-) total interaction cross section on Ar that can be achieved applying the "Sliced TPC" method to our thick target experiment. These plots are a fundamental hint for future studies on real data, since they provide an expectation value for the cross section experimental results.

Summary:
The results of this analysis of pion interaction in Liquid Argon based on simulated data in Geant4 MC framework can be here summarized:

- The Geant4 Bertini model for hadronic interactions has been validated for pions for several target nuclei (^{12}C, ^{40}Ca, ^{56}Fe...) through comparison with experimental data. Moreover the Geant4 Bertini model and also the Genie hA model still need to be improved for intermediate nuclear masses A range (as Ar, A=40) for energies near the Δ resonance region.

- The "Sliced TPC" approach to evaluate charged pion- Ar nucleus interaction cross section in a thick target experiment, as LArIAT TPC volume, gives same results as a thin target experiment; so it could be applied to real data (pion tracks) to evaluate the cross section for pion interactions in LArTPC.
  For LArIAT experiment, with our actual beam intensity, it appears that in the current beam conditions we would need two weeks of continuous data acquisition for each fixed pion charge (π^+, π^-) to acquire enough data to process later with the "Sliced TPC" technique to achieve a statistical error of less than 10 % on total cross section σ_{tot}, calculated with 50 MeV energy steps.

- Next step would be to apply the "Sliced TPC" approach to real reconstructed tracks from LArIAT TPC to get out an evaluation of charged pion-Ar nucleus cross section (systematic errors need to be estimated).

Chapter 4

LArIAT: Data collection and preliminary analysis

4.1 Commissioning and first runs

LArIAT was commissioned in February 2012. The MCenter beamline in FTBF [32] had to be readapted for LArIAT experiment purposes.
We had the first beam runs from summer 2014 to test beamline detectors while ArgoNeuT TPC was refurbished for LArIAT purpose, the group from BNL was completing the cold electronics readout that would be mounted over the TPC inside the cryostat and we were testing and setting up the light collection system too. In November 2014 the TPC was put inside the cryostat on the beamline.
After the last tests and surveys, the TPC was filled with Argon on 29th April 2015.
On Thursday, April 30, the TPC wire planes and the cathode were powered on at their nominal voltage and we started taking data.
Luckily we had beautiful tracks at first try. In Fig.4.1 and Fig.4.2 are shown the first cosmic track and one of the first beam events collected by the LArTPC.

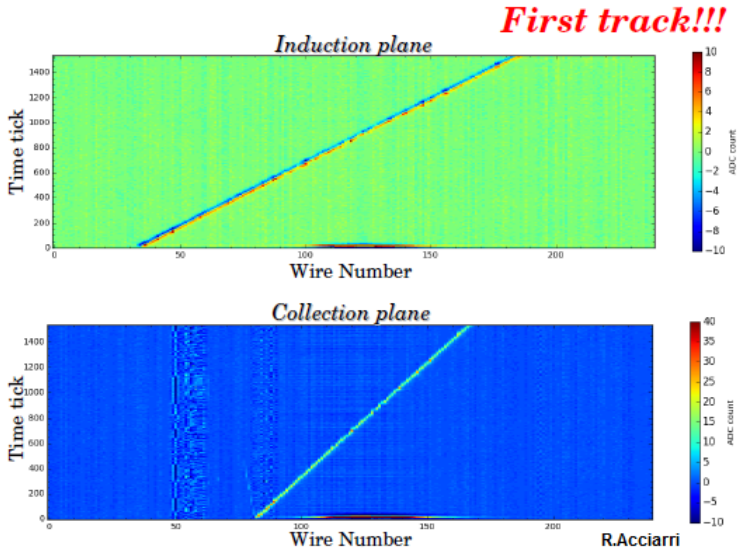

Figure 4.1: First events collected in the TPC - 30/04/2015: track of a cosmic ray crossing the TPC.

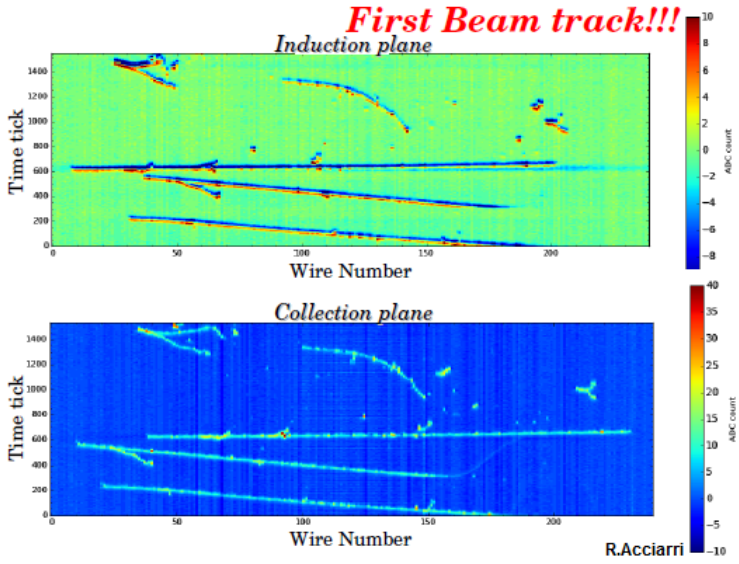

Figure 4.2: First events collected in the TPC - 30/04/2015: beam particle track in the TPC.

We run the test beam for 24 hours a day while tuning the beam, the TPC readout performances and the DAQ issues and taking data. This first run lasted about three months, until the 4th of July, after which the cryogenic system and the detector itself will undergo upgrades to prepare for longer follow-up runs.

4.2 TPC Event Imaging

The non-destructive configuration of the wire-planes and the individual wire signal readout/recording, described in Par.2.3, allow for imaging of the ionization event in the LArTPC volume.

In LArIAT TPC each of the two instrumented wire-planes provides a two dimensional image corresponding to the event projection on a plane whose axes are identified as "wire coordinate" and "time coordinate". Both coordinates are discrete, in terms of the wire-number in the plane (n_w, from 1 to 240 for both Induction and Collection) and of the time tick of the signal digitization (n_t, from 1 to 3072 samples).
A schematic view of the wire plane geometry and of the reference coordinate frames are shown in Fig.4.3. The two projection-planes are indicated as (w; t) for the Collection and (v; t) for the Induction. The two planes have the time coordinate in common. The wire-coordinates lie along the wire pitch directions.
A 2-D image of the ionization tracks in the event is obtained for each projection plane. It is possible also to see the recorded waveforms V_{n_t} of each wire in the plane, exploited through the signal waveform processing. The signal pulse amplitude (i.e. the local ionization charge release) is coded into the color level of the image pixelation.
Image reconstruction in 3-D can be accomplished by combining information from the two 2-D views (see Par.4.4). The reference system (x; y; z) adopted for such spatial reconstruction is also indicated in Fig.4.3.

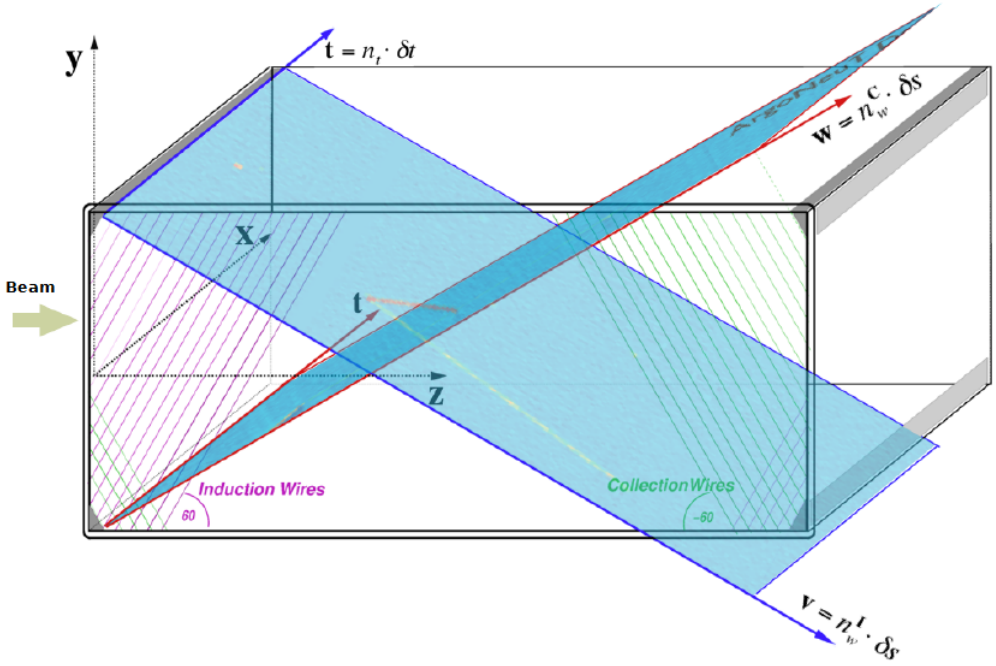

Figure 4.3: Schematic of the LArIAT TPC and the reference frames adopted for 2-D and 3-D imaging of the ionization events. The coordinates (w; t) for the Collection view and (v; t) for the Induction view are explicitly indicated in terms of wire index ($n_W^{I;C}$ and wire pitch (δs) for the wire coordinate and time tick index (n_t) and sampling time (δt) for the time coordinate.

4.3 Pion interaction events collected in the TPC

Some events collected in the LArTPC are here displayed.
Event display - 2 views: top view is Induction Plane, bottom view is Collection plane).
From Fig.4.4 to Fig.4.13 are shown the different topologies of different pion processes in LAr: hadronic interactions, decays, π^- capture, as discussed in Chap.3 Par.3.2. As discussed in Chap.3 Par.3.3.2, a pion can also experience multiple interactions inside the LArTPC active volume, as we can see in Fig.4.11 and Fig.4.12.
Other beam particles, as electrons and protons, and their tracks and interactions in LArTPC volume are here shown in Fig.4.14 and Fig.4.15.
Some cosmic events are represented in Fig.4.16.

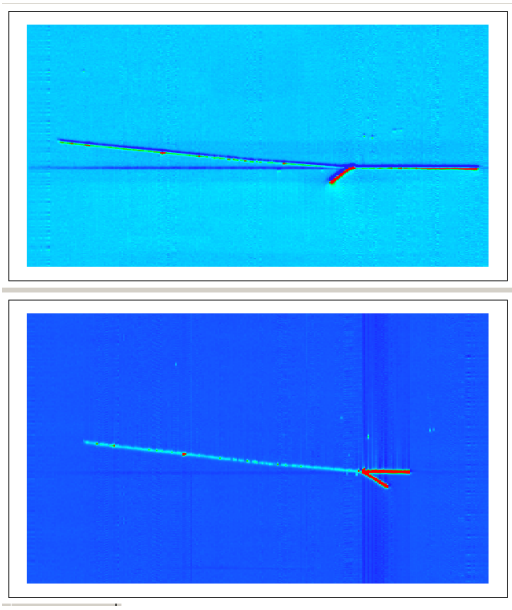

Figure 4.4: π^+ Absorption on Ar nucleus with 2p in the final state.
$\pi^+(np) \rightarrow p\ p$

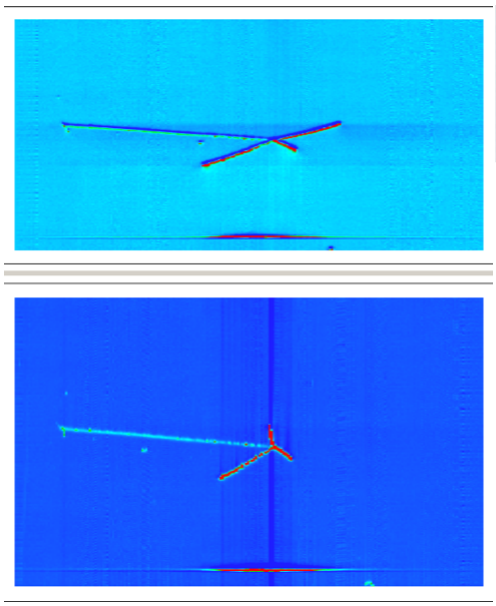

Figure 4.5: π^+ Absorption on Ar nucleus with 3p in the final state.
$\pi^+(npp) \rightarrow p\ p\ p$

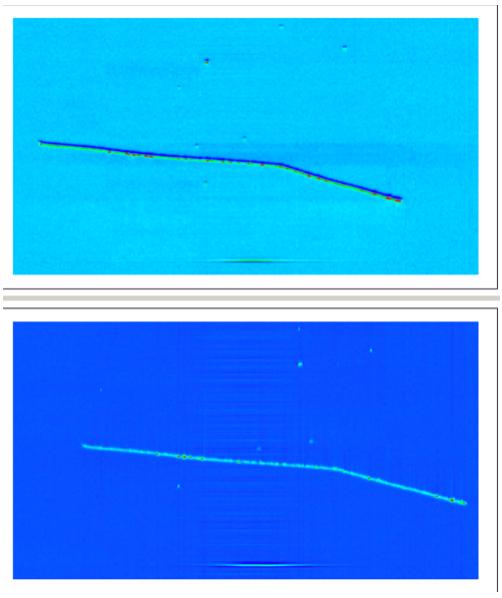

Figure 4.6: Pion π elastic scattering (one kink).

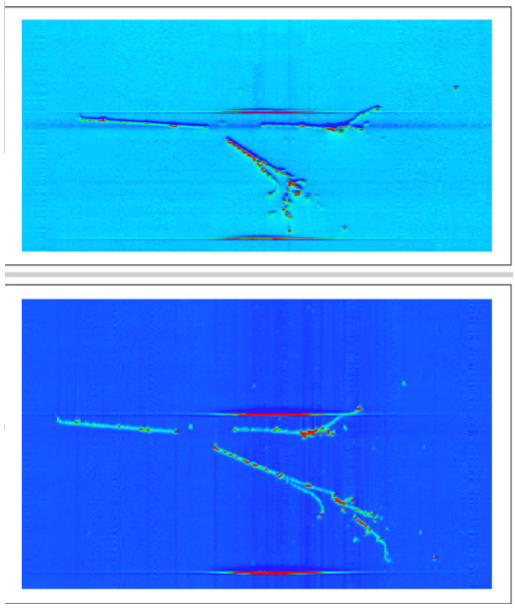

Figure 4.7: π^- Single charge exchange.
$\pi^- + p \rightarrow \Delta^0 \rightarrow \pi^0 + n$.
The neutral pion π^0 quickly decays in two gammas which initiate two electromagnetic showers.

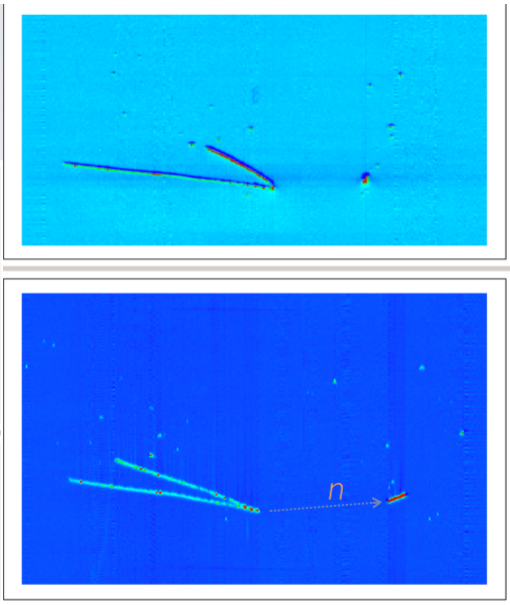

Figure 4.8: π^- Inelastic scattering on Ar nucleus. The pion is back-scattered and a neutron n is knocked-out, then it is captured by another nucleus and it is converted in a proton.
π^- + n(target) $\rightarrow$ π^- + n (knock-out)

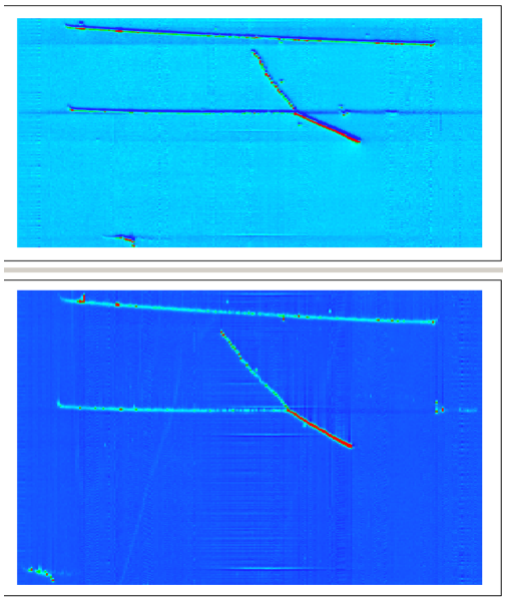

Figure 4.9: π^+ Inelastic scattering on Ar nucleus. The pion is scattered and a proton p is knocked-out.
π^+ + p(target) $\rightarrow$ π^+ + p (knock-out)

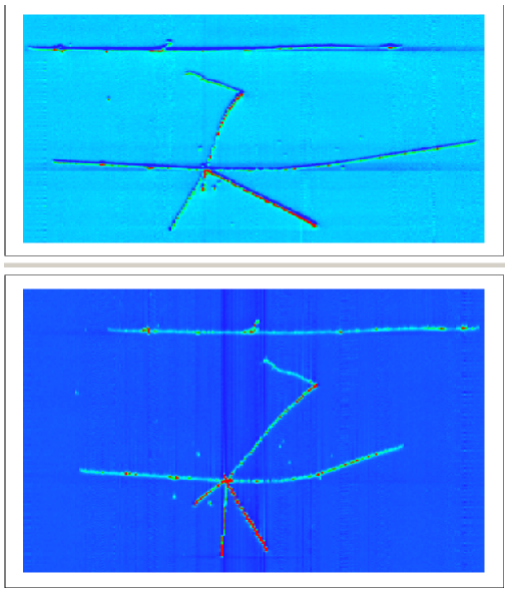

Figure 4.10: High energy charged pion interaction with Ar nucleus, with many pions production (3 charged pions) and a few nucleons are knocked out (2 p).

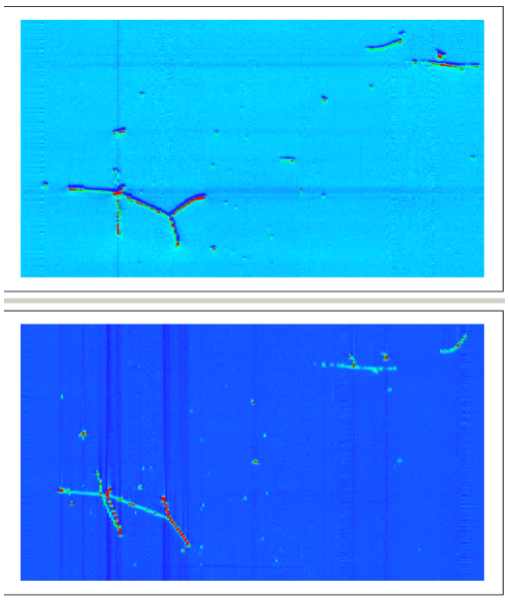

Figure 4.11: Multiple hadronic interactions experienced by a charged pion crossing the LAr volume.

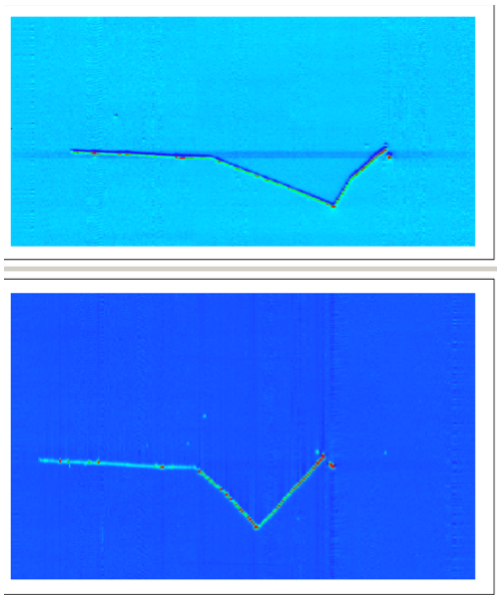

Figure 4.12: π^- Double elastic scattering and then it is captured at rest by Ar nucleus and low energy nucleons are emitted.

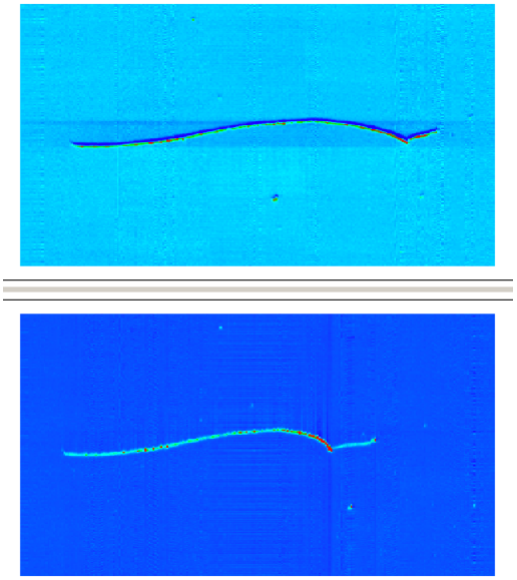

Figure 4.13: π^+ Decay at rest.
$\pi^+ \rightarrow \mu^+ + \nu_\mu$,
$\mu^+ \rightarrow e^+ + \nu_e + \overline{\nu_\mu}$

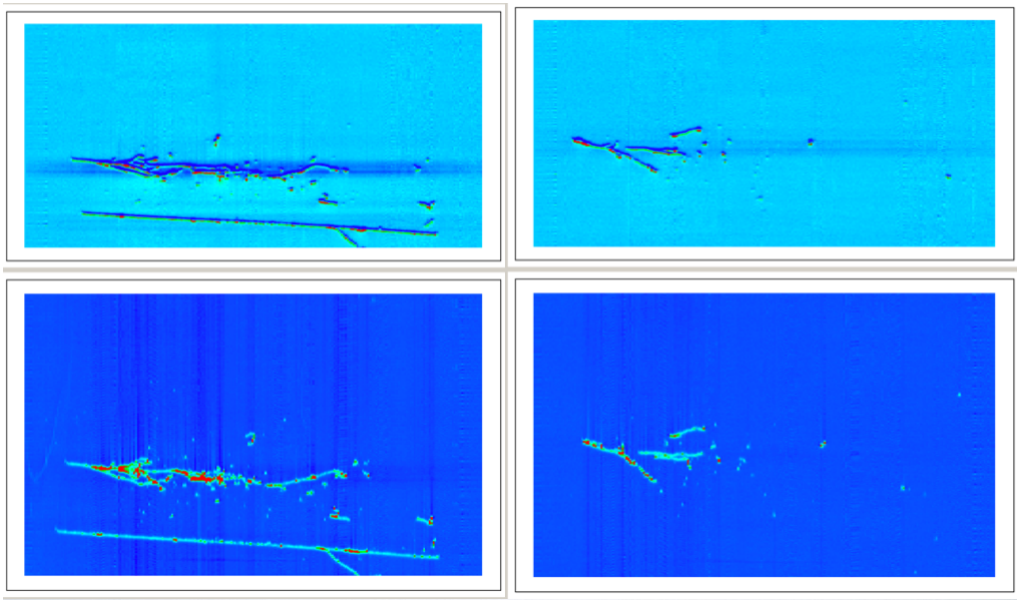

Figure 4.14: Electron induced shower (electron coming from the tertiary beam) at left and gamma induced shower (e.g. gamma coming from π^0 decay happened outside the TPC volume) at right.

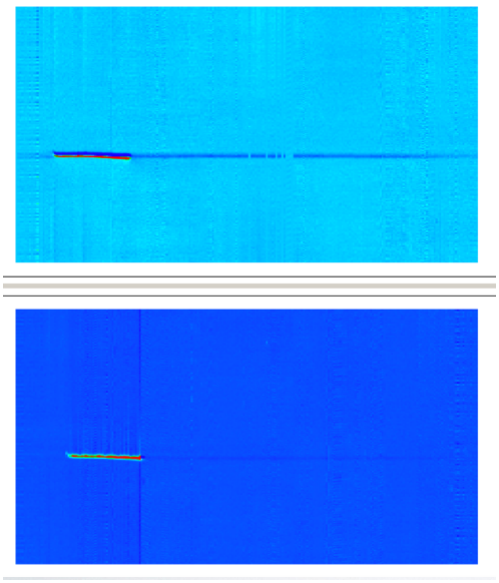

Figure 4.15: Proton track. The proton is a heavily ionizing particle and tends to stop quickly in LAr volume.

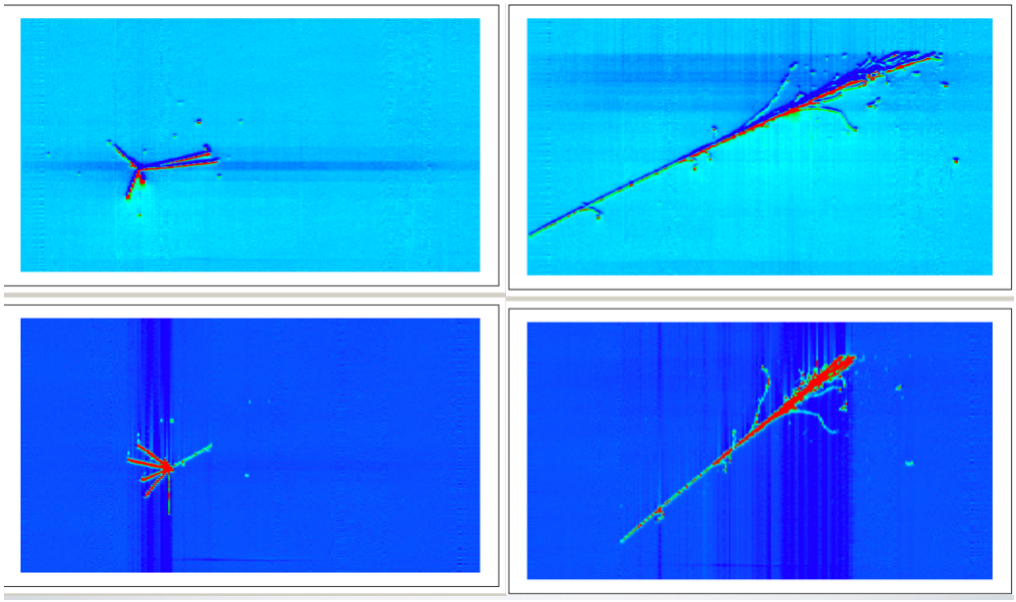

Figure 4.16: Cosmic triggered events.
Hadron interaction (π) with 4 p at the vertex at left. High energy deposition of a crossing cosmic (μ) at right.

4.4 Event Reconstruction

The pulse signals on the TPC wires are collected and analyzed through LArIATSoft, a dedicated framework for Liquid Argon TPC tracks reconstruction for our specific experiment. [65]
With the Event Viewer, previously described, it is possible to achieve a 2-D track reconstruction of the event on the Induction and Collection planes; it is useful for studying the topologies of the interactions of incoming particles with Argon nuclei.
To achieve a 3-D reconstruction of the event it is necessary to match the hits/clusters which have the same drift time in the two views.
It is also possible to measure of the energy deposit along the track (calorimetry), after a calibration of the electronics response to the collected charge (ADC - pC).

The aim is to achieve a complete and precise event reconstruction of identified particles (pions, muons, protons...) crossing or experiencing an interaction in the LArTPC active volume. After that, the following step would be to make charged pion interaction cross section studies, since pions are the main component of LArIAT tertiary beam, and a complete characterization of the LArTPC response.

4.4.1 Event Reconstruction in LArIATSoft

The LArIATSoft offline software code [65] is organized within the LArSoft package [64], a common framework for the simulation and data reconstruction/analysis of LAr-based experiments at Fermilab.
The general structure of the offline event reconstruction chain is well established, while the individual steps are subject to continuous improvement. The event reconstruction development has focused on straight-line tracks, along with vertex finding algorithms, for charged particles tracking. More complicated pattern recognition software is currently being developed for the reconstruction of electromagnetic showers.
At each beam-spill, the LArIAT Art-event structure recorded by the DAQ system contains N triggers, in which N is how many times during the beam-spill duration (4 s) one of the selected triggers in V1495 board is fired; for each trigger 2×240 digitized signal waveforms from the wires in the Induction and Collection planes are collected.
When a packet of electrons (e.g. a segment of an ionization track crossing the TPC) is detected by a wire, a pulse above baseline is generated within the drift time interval of the recorded waveform from this wire. The shape of the pulse is different for wires in the Induction-plane and in the Collection-plane due to the geometrical and electrical configuration of the TPC planes (bipolar signal of crossing electrons in Induction plane, unipolar signal of collected electrons in Collection plane).
The raw pulse is converted in a LArSoft readable data format and associated to its trigger inside the Art-event (that corresponds to the spill, for us) [StandardFragmentToDigit module]. Next step is signal identification, noise filtering and reshaping [Calwire module]; then the pulse is converted into a "hit" characterized by its peak amplitude and coordinates in the wire-time plane [HitFinder module]. The offline procedure then uses the hits from both planes to fully reconstruct the ionizing tracks in the event, i.e. the space-coordinates of the hits associated to the track and the energy deposited at those coordinates [Cluster modules, Track modules....].

The offline reconstruction chain can be summarized in the following steps:

- Raw waveform treatment and noise filtering.

- Hit construction and identification.
- Clustering proximal hits and Two dimensional (2D) line reconstruction.
- Three dimensional (3D) track reconstruction and Vertex finding
- Calorimetric reconstruction of deposited energy.
- Track matching with the beamline detectors (Wire Chambers: track direction and incident particle momentum; ToF, Aerogel counters and μ Range Stack: particle identification).

4.4.2 Preliminary reconstruction of pion tracks in the TPC

Actually there is a huge effort of all the LArIAT collaboration to have each step of the whole reconstruction working properly, from the beamline auxiliary detectors beam track reconstruction, with PID and incident momentum measurement, as well as the TPC events reconstruction and eventually the matching between these two informations for a complete characterization of each beam particle that goes through the TPC LAr volume.

I am working in the development for LArIAT purposes and in a preliminary test of the reconstruction chain for the events in the TPC, from LArSoft existing modules. At this moment the TPC reconstruction chain is producing 3-D tracks for crossing particles and particles that experience an elastic and inelastic scattering.

The preliminary TPC event reconstruction chain is here summarized:

- Conversion from raw data to LArIATSoft readable data: FragmentToDigit module
- TPC wires signals - noise deconvolution: CalWireT1034 module
- TPC wires signals - hit finding: GaussHitFinderT1034 module (Each pulse on the wires, with an amplitude and time width over a defined threshold, is fitted with a gaussian function and if the χ^2 of the fit is within a defined value, a hit is associated to that pulse.)
- Hits clustering: DBClusterT1034 module (For each wire plane hits that are close to each other and have coherent amplitude values are grouped together in clusters.)
- Simple 3-D Tracking: SpacePointsT1034 module (Hits and clusters on the two views are matched if they fall within a certain time interval, then a 3-D point is reconstructed; collections of spacepoints are grouped into 3-D tracks.)

Two reconstructed pion tracks, with an elastic kink, in the TPC volume are here reported as an example of the status of the 3-D reconstruction for LArIAT events.

- Run 5835 spill 46: Positive polarity, 60A - low momentum selection (200 MeV/c - 700 MeV/c):
  From the ToF counters: ToF = 33 ns $\rightarrow$ PID: π^+ (See. Fig.2.7 in Chap.2)
  From the Wire Chambers: Incident Kinetic Energy $E^{kin}_{inc} \simeq 250$ MeV
  From the TPC 3-D reconstruction:
  Entering point in the TPC $\vec{x}_0 = (27.9423, 7.2, 0.46188)$ cm
  Interaction point [kink] $\vec{x}_1 = (18.4483, 8.0, 70.6677)$ cm
  The track length until the interaction point: $\mid \Delta\vec{x} \mid = 70.85$ cm. The Kinetic Energy at the Interaction point is here evaluated using the Bethe-Bloch energy loss formula, applied step by step for each point of the track, since the calorimetry modules haven't been reedited and updated for LArIAT data yet. $E^{kin}_{int} \simeq 87$ MeV. See Fig.4.17 and Fig.4.18.

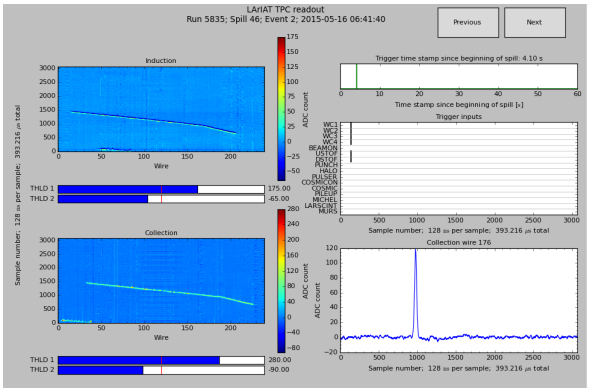

Figure 4.17: 2-D Event display: Run 5835 spill 46. pi^+ (low momentum) experiencing an elastic scattering in the TPC volume.

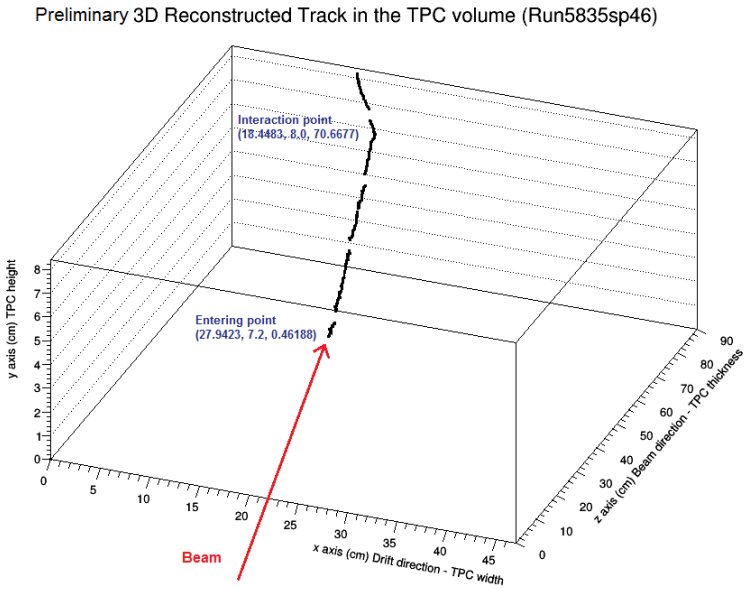

Figure 4.18: Preliminary 3-D reconstructed track for pi^+ elastic scattering event. Run 5835 spill 46.

- Run 5798 spill 7: Positive polarity, 100A - high momentum selection (500 MeV/c - 2.0 GeV/c) From the ToF counters: ToF = 32 ns $\rightarrow$ PID: π^+ (See. Fig.2.7 in Chap.2)
  From the Wire Chambers: Incident Energy $E_{inc}^{kin} \simeq 500$ MeV
  From the TPC 3-D reconstruction:
  Entering point in the TPC $\vec{x}_0 = (31.0324, 8.8, 0.46188)$ cm
  Interaction point [kink] $\vec{x}_1 = (25.7294, 11.6, 58.4278)$ cm
  The track length until the interaction point: $\mid \Delta\vec{x} \mid = 58.30$ cm. The Kinetic Energy at the Interaction point is here evaluated using the Bethe-Bloch energy loss formula, applied step by step for each point of the track, since the calorimetry modules haven't been reedited and updated for LArIAT data yet. $E_{int}^{kin} \simeq 351$ MeV.
  See Fig.4.19 and Fig.4.20.

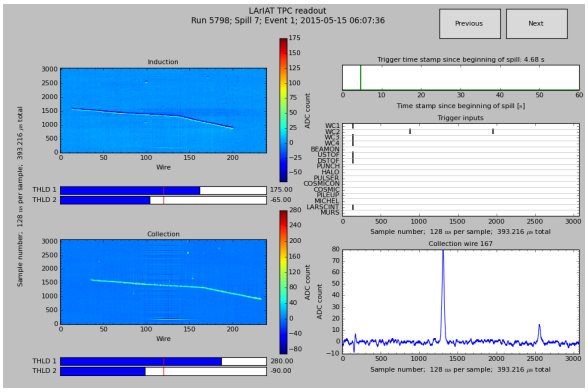

Figure 4.19: 2-D Event display: Run 5798 spill 7. pi^+ (high momentum) experiencing an elastic scattering in the TPC volume.

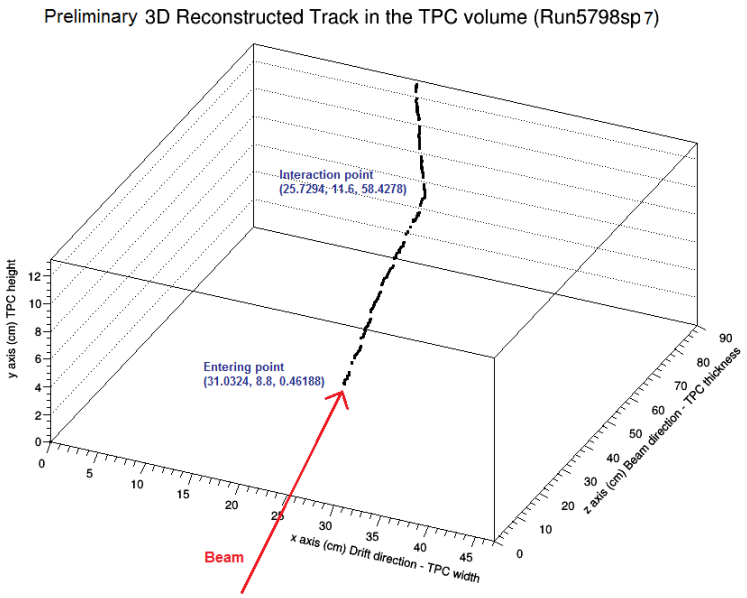

Figure 4.20: Preliminary 3-D reconstructed track for pi^+ elastic scattering event. Run 5798 spill 7.

As soon as we will have all the reconstruction steps working properly, for different interaction topologies, we could apply the "Sliced TPC" approach to real reconstructed tracks, with the energy deposit information from calorimetry modules and the point of interaction from the vertex finders, to calculate the total hadronic interaction cross section for charged pions in LAr (systematic errors need to be estimated).

Chapter 5

LArIAT Scintillation Light collection R&D: Front-end electronics for SiPMs

While collecting the ionization charge from the TPC, we aim to improve the energy resolution of the whole detector system, detecting the scintillation light produced in Liquid Argon too.
Actually two different light collection systems are mounted for first tests in the cryostat, two UV-sensitive PMTs and three SiPMs, as described in Chapter 2.
The idea is to figure out which of the two could have better performance in terms of timing, energy resolution and behavior in cryogenics.
I have been involved in the development and test of front -end electronics for SiPMs devices.

5.1 SiPM technology

The Silicon Photomultiplier (SiPM) is a semiconductor-based detector consisting in a high density matrix of diodes with a common output load.
Each diode is operated in a limited Geiger-Muller mode (Geiger Mode Avalanche Photodiode, GM-APD), in order to achieve gain at the level of 10^6 and comparable to PMTs. They have the capability of detecting signals of single photons.
The SiPM is a detection tecnology developed for counting photons in the wavelength range between 320 nm up to 900 nm (optical range) with a peak sensitivity at 440 nm. [66] [67] [68]

SiPMs are considered better to use in some circumstances due to their smaller size, lower operating voltage and insensitivity towards magnetic fields compared to PMTs. Furthermore, they have a higher photon detection efficiency (PDE).
The disadvantages compared to PMTs include especially noise phenomena such as the temperature-dependent dark noise, afterpulsing and optical crosstalk, which instead depends on overvoltage.

5.1.1 SiPM: Principles of operation

The SiPM is operated in the Geiger-Muller region, which means that it's inverse polarized at V_{bias} > than V_{bk} (junction breakdown voltage).
When a photon hits the active area of the device- a single pixel/Geoger Mode Avalanche Photodiode (GM-APD)-, producing a photoelectron, the latter will trigger an avalanche, while drifting to the electrode and traversing the high-field region.
The single pixel/GM-APD capacitance C_d, which depends on the pixel size, discharges from V_{bias} to V_{bk} with a time constant τ_d=R_d C_d (rise time), in which R_d is the equivalent diode series resistance; at the same time the external currents grows from 0 to I_{latch}=$\frac{\Delta V}{R_q}$, where ΔV= V_{bias}-V_{bk} is the junction over-voltage and R_q is the quenching resistor connected in series to the APD.
Then, when the number of carriers traversing the high-field region fluctuates to 0, the avalanche is quenched. It is necessary to use a proper quenching resistor to let the internal current decrease to a level such that statistical fluctuations may quench the avalanche (turn-off time).
So, C_d is charged fromV_{bk} to V_{bias} until there is no more current flowing, with a time constant τ_q = R_q C_d. The pixel/GM-APD 99% recovery time corresponds to $\approx 5\tau_q$.
The leading edge of the signal is much faster than trailing edge: τ_d « τ_q and turn-off mean time is very short (if R_q is sufficiently high, I_{latch} ≈ 10-20 μA).

In Eq.5.1 and 5.2, are shown the variation of over-voltage V_{over}(t) and the external current i_{ext}(t) of a **GM-APD - single SiPM pixel**, when a photon-induced avalanche is triggered.

$$V_{over}(t) = \Delta V[a(-e^{-\frac{t}{\tau_d}} + e^{-\frac{t}{\tau_q}}) + 1] \tag{5.1}$$

where ΔV depends on the V_{bias} applied to the SiPM and the value "a" depends on the ratio of τ_d and τ_q for the device. The equation 5.1 is plotted for the SiPM SensL MicroFB 60035 for room temperature behavior and shown in Fig. 5.1.

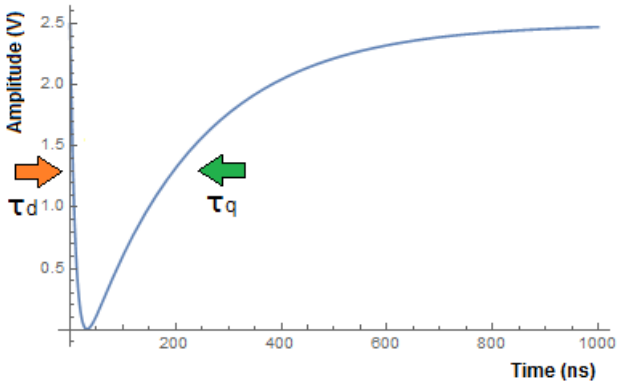

Figure 5.1: V_{over}(t) for SensL MicroFB 60035 at 300K ($\tau_d \simeq$ 10ns and τ_q = 210 ns) and ΔV = +2.5V

$$i_{ext}(t) = \frac{\Delta V}{R_q}(1 - e^{-\frac{t}{\tau_d}}) + \frac{\Delta V}{R_q}e^{-\frac{t}{\tau_q}} \tag{5.2}$$

Here we assumed $\frac{5\tau_d}{\tau_q}$ «1. The equation 5.2 is plotted for the SiPM SensL MicroFB 60035 for room temperature behavior and shown in Fig. 5.2.

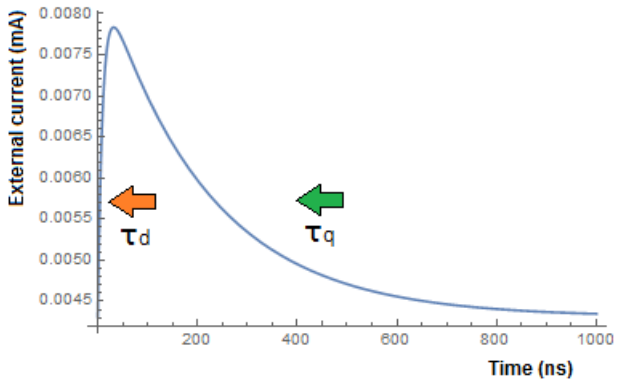

Figure 5.2: i_{ext}(t) for SensL MicroFB 60035 at 300K ($\tau_d \simeq$ 10ns and τ_q = 210 ns) and ΔV = +2.5V

Since the SiPM is an array of GM-APDs, each pixel outputs a pulse at the same amplitude when it detects a photon.The SiPM output current pulse is so the superimposition of multiple pixel pulses, as shown in Fig.5.3.
Each pixel ouputs only one pulse and this not vary with the number of incident photons; this means that SiPM output linearity gets worse as more photons are incident of the active area as well as when two or more photons enter one pixel.

When photons hit the SiPM at a particular timing, its output pulse height varies depending on the number of photons detected; otherwise when the timing at which light enters a SiPM is different, the output pulse would be the convolution of the single pixel response with the time distribution of the photons and the total number of photons detected within a certain time period can be estimated by integrating the SiPM output using an integrating amplifier. This feature would be discussed in Section 5.1.3.

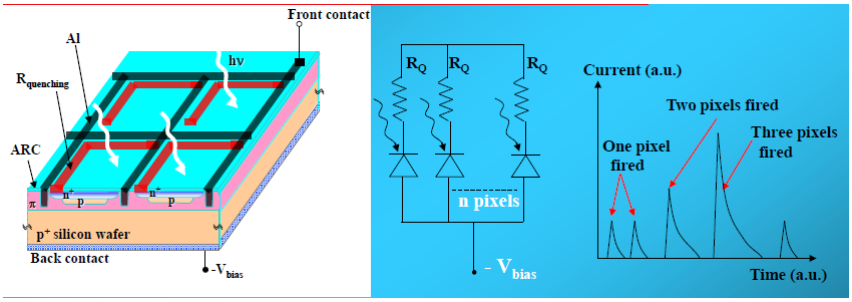

Figure 5.3: SiPM: Equivalent electric circuit and current signals of single photons.

It is possible to define a **Gain**, G for the SiPM, as the charge (Q) of the pulse generated from one pixel when it detects one photon divided by q_e, the electron charge. (See Eq.5.3):

$$G = \frac{Q}{q_e} = \frac{I_{latch}\tau_q}{q_e} = \frac{\Delta V}{R_q}\frac{\tau_q}{q_e} = \frac{\Delta V C_d}{q_e} \tag{5.3}$$

For example, for the SiPM SensL MicroFB 60035 at 300K: N_{pixels}=18980, C_{SiPM}=3400pF -> C_d = 0.18 pF; if ΔV= + 2.5 V, the expected gain G= 3 $\times$ 10^6.
For example, for the SiPM Hamamatsu Array S11828-3344M at 300K: C_d = 0.09 pF; if ΔV= 100 mV, the expected gain G= 7.5 $\times$ 10^5.

The SiPM gain is temperature dependent since APD breakdown voltage V_{bk}, present in ΔV, decreases quite linearly lowering the temperature. We can override this problem,

reaching same gain at different temperatures, varying V_{bias} too, such that ΔV still remains the same value, as the one used at room temperature for example.

Since the gain G is linear with the over-voltage (see Fig.5.4), it appears that increasing the bias voltage V_{bias} would result in better SiPM performance. However we have to take in account that noise effects, as dark counts and afterpulses, which will be described later, increase not linearly with bias voltage and it could affect the Photon Detection Efficiency (PDE) of the device.

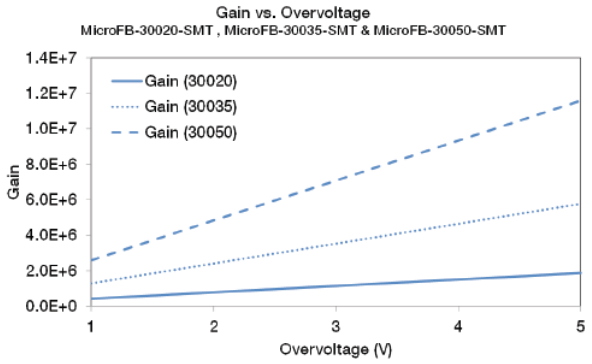

Figure 5.4: Single channel SensL Micro-FB series: Gain vs Overvoltage, for different pixel sizes - different C_d (20 μm, 35 μm, 50 μm) at room temperature (300 K) [77].

The SiPM efficiency can be described by the PDE parameter. The photon detection efficiency is the ratio of the number of detected photons to the number of incident photons that hit the device. It can be parametrized as shown in Eq.5.4 and in Fig.5.5 is shown the PDE dependence on photon wavelength and overvoltage.

$$PDE = \frac{\text{Number of incident photons}}{\text{Number of detected photons}} = QE \times P_{01} \times FF \tag{5.4}$$

where:
- QE(λ,T) is the quantum efficiency, the probability for a photon to generate a carrier that reaches the high filed region; it depends on the photon wavelength λ and on temperature T;
- P_{01}(λ,T, V_{bias}) is the avalanche triggering probability, the probability for a carrier traversing the high-field to generate the avalanche; it depends on photon λ, temperature and bias voltage V_{bias} applied (the higher the reverse voltage applied will result in the higher P_{01});
- FF is the geometrical fill factor, the ratio of the light detectable area to the entire pixel area, due to dead areas, like structures between the cells; the smaller the pixel size, the lower the FF factor.

The SiPM devices have internal noise sources:

- Dark counts: pulses triggered by non-photo-generated carriers (thermal/tunneling generation in the bulk or in the surface depleted region around the junction); these carriers are multiplied to constant signal level (1 pe), but the shape of the pulses induced by them is not distinguishable by photon-generated ones. The dark count rate varies with temperature, for a fixed gain:

$$DCR \approx T^{1.5} e^{-\frac{E_{act}}{2K_B T}}$$

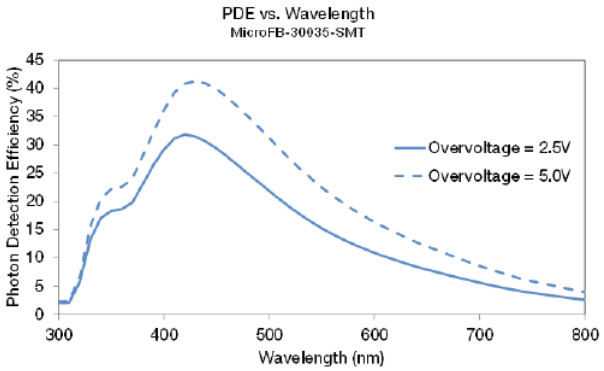

Figure 5.5: Single channel SensL Micro-FB series: PDE vs Wavelength, for different overvoltages at room temperature (300 K) for a 3 mm x 3 mm device (35 μm pixel) [77].

where E_{act} is the effective band gap, that at low temperature is smaller that the typical E_g value for silicon.

- "Optical" cross-talk: photo-generation during the avalanche discharge. Some of these photons can be absorbed in the adjacent cells possibly triggering new discharges. It strongly depends on ΔV: the higher the gain and the higher the carriers flux (current) during an avalanche the more the possibility that secondary photons are generated and detected by other pixels.

  $$P_{crosstalk} \approx \Delta V^2$$

  To reduce this effect an optical isolation between cells is made by trenches (V barriers) filled with opaque material and the device might be operated at low over-voltage.

- Afterpulse: carriers can be trapped by lattice defects during an avalanche and then released triggering another avalanche, that would appear in the signal as an additional pulse delayed in time; this noise effects depends on ΔV^2, since it increases for higher avalanche trigger probability and higher carrier flux during the avalanche. The device is only partially sensitive to after-pulsing during recovery, but recovery hides after-pulses (does not cancel them). For a fixed ΔV, the afterpulse probability increases with lower temperatures, because the characteristic time constants of the traps increases.

5.1.2 Variation of SiPM behavior with temperature

In a constant temperature environment, the overvoltage ΔV applied to a SiPM determines its operational characteristics such as gain and PDE. Because temperature is an important parameter affecting the opto-electrical characteristics of a p-n junction such as the width of the depletion region, the breakdown voltage, band-gap energy, resistivity, and more, the operation of a SiPM will be strongly affected by this parameter.
It is expected that a SiPM would improve its performance if operated at lower temperatures, since dark noise is attenuated, and it can be biased at lower voltage to achieve the same gain as room temperature since breakdown voltage decrease with low temperature.[69] [70] [71] [72]

Silicon diode junction **breakdown voltage** $V_{bk}(T)$ has an almost linear dependence on temperature until - 200°, see Eq.5.5. Breakdown voltage decreases at low temperatures due to larger carriers mobility. The change in breakdown voltage will obviously have an effect on overvoltage; in fact the junction is expected to have larger ionization rate for electric field fixed - fixed V_{bias} at lower temperatures.

$$V_{bk}(T) = A + B \times T(^{\circ}C) \tag{5.5}$$

For example, for SensL SiPMs the slope coefficient for the temperature dependence of V_{bk} provided in the datasheets for several device dimensions and pixel pitches is B = 21.5 $\frac{mV}{^{\circ}C}$. So, since V_{bk}(T=300 K)= 24.5 V, the expected breakdown voltage for the SensL MicroFB is expected to be $V_{bk}(T = 90K)$ = 21 V at LAr temperature.

Another example of the SiPM temperature dependence is the **recovery time of a pixel from avalanche,** τ_q. The characteristic time of the recovery is the R_qC_d time constant determined by the values of the junction capacitance C_d and of the quenching resistor R_q. For a given ΔV, temperature affects the width of the depletion region and, thus, C_d. It also affects the resistance of the quenching resistor R_q. Thus, the product of these two quantities can also change with temperature affecting the recovery time. (See Fig.5.6.) As the temperature decreases, the Boltzmann distribution implies a decreasing fraction of electrons in the conduction band and, thus, an increasing resistivity of the semiconductor. The first-generation passive quenching resistors were made from polysilicon; the resistivity of this material is strongly temperature dependent. The polysilicon resistor increases the resistance when cooled, so R_Q will increase and the recovery time too. The solution that has been adopted for second-generation passive quenching resistors is to use a metal alloy with high resistivity, which is less temperature dependent. (See Fig.5.7.) [1] The junction capacitance, C_d, also varies a bit with temperature, it increases with temperature.

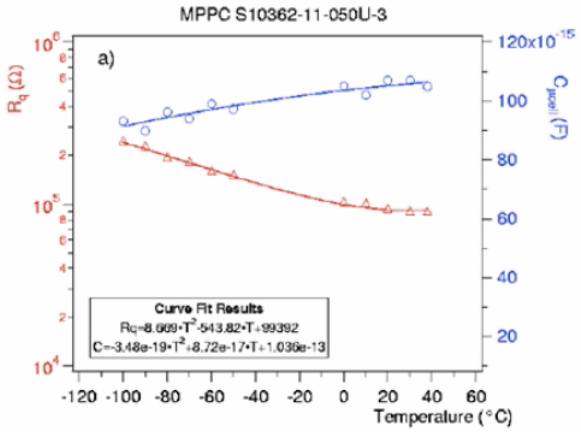

Figure 5.6: Temperature dependence of the polysilicon quenching resistance (red) and junction capacitance (blue) for Hamamatsu MPPC S10362.

[1] New generation Hamamatsu SiPMs have metal film quenching resistors, while SensL SiPM still have polysilicon resistors.

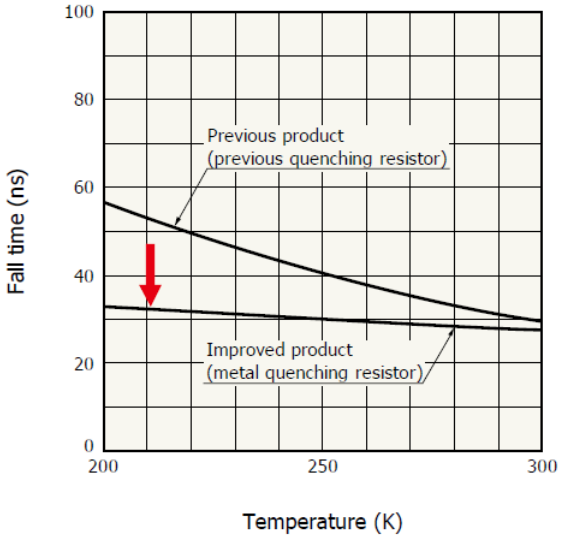

Figure 5.7: Hamamatsu MPPC: Recovery time vs. temperature (photosensitive area: 1 mm sq, pixel pitch 50 μm, typical example).[73]

5.1.3 SiPM response to LAr scintillation light

The direct SiPM response to LAr scintillation light can be considered as a convolution between the photon distribution S(t) (see Eq.1.21) and the impulsive current response of the device i_{ext}(t) (see Eq.5.2):

$$i_{SiPM}(t) = S(t) \otimes i_{ext}(t) \tag{5.6}$$

As discussed in Par.5.1.2, we should expect the quenching time τ_q at 90 K would be higher than the value at 300 K, because of the increasing value of the quenching resistor R_q at lower temperatures, especially if it is in polysilicon.
The analytic shape for the expected waveform for SiPM current read on scope 50 Ω load resistance is shown in Eq.5.7 and Fig.5.8 (assuming $\tau_d \ll \tau_q$ and negligible at a first order of approximation for the SiPM).

$$\begin{aligned} V_{out}(t) &= i_{SiPM}(t) R_L \\ V_{out}(t) &\approx -C_1 \frac{A}{\tau_F} e^{-\frac{t}{\tau_F}} - C_2 \frac{B}{\tau_S} e^{-\frac{t}{\tau_S}} + C_3 e^{-\frac{t}{\tau_q}} \end{aligned} \tag{5.7}$$

where τ_F ad τ_S are the characteristic time constants of LAr scintillation, A and B are the parameters linked with the different particle that crosses LAr volume, τ_q is the SiPM quenching time and parameters C_i (i=1,2,3) come from the convolution integral and depend on LAr time constants τ_F and τ_S, on the recovery time of the SiPM τ_Q and on the current to voltage conversion.
We can see from Fig.5.8 that the rising edge of the waveform has a strong dependence on parameters A and B, the fraction of scintillation light that is emitted from singlet and triplet excited states; thereby their value depends on the incident particle, so the V_{out} SiPM waveform in Eq.5.7 can be used to make Pulse Shape Discrimination and particle identification.[74]

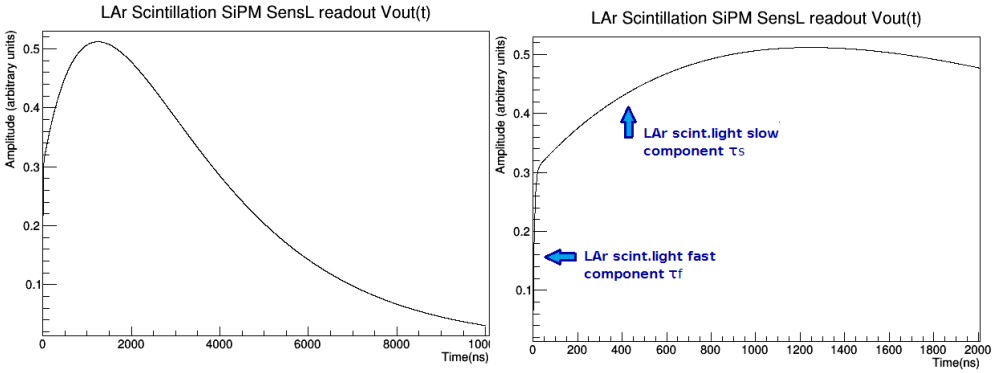

Figure 5.8: Expected V_{out}(t) read on the scope for SiPM SensL MicroFB 60035 at 90 K, for a MIP crossing LAr volume (A=0.3, B=0.7), assuming τ_q(T = 90 K) $\approx$ 2.5 μs (instead of 210 ns at 300 K) for the device. On the right: zoom on the rising edge shape of the signal V_{out}(t).

The event of a crossing particle exciting LAr which emits scintillations photons that are collected by the SiPM can be summarized as a series of photon-initiated avalanches in the SiPM microcells, with an early many-pe pulse from the fast decay of the singlet state followed later by the slow decay of the triplet state. So if we collect the direct SiPM waveform V_{out}(t), the information on the photon distribution would be present in the rising edge of signal, if the scintillation distribution $S(t)$ is not a δ(t) pulse as for LAr.
In this case, when photons hit the SiPM active area at different times, if we're interested in photoelectron counting we need to use a preamplifier - integrating step after the SiPM output.

If we consider adding a preamplification stage, its transfer function in the time domain is the one in Eq. 5.8, if the amplifier is operated in transimpedance inverting mode.

$$R_{PA}(t) = \frac{R_f}{\tau_f - \tau_D}(e^{-\frac{t}{\tau_f}} - e^{-\frac{t}{\tau_D}}) \tag{5.8}$$

where τ_F=R_f C_f is the feedback integration time (R_f and C_f are the feedback resistor and capacitor) and τ_D is the preamplifier response time.

The SiPM + preamplifier impulsive response function R_{SiPM}(t) for a single photoelectron is:

$$R_{SiPM}(t) \approx i_{ext}(t) \otimes R_{PA}(t) \tag{5.9}$$

Since multi photoelectron pulses represent a sum of single-pe pulses on different microcells that are produced within the SiPM response time τ_d, a waveform coming out from the preamplifier represents simple sums of single-pe pulses (and associated electronic noise) convolved with the SiPM's single microcell response function.
The voltage output signal from the preamplifier $V_{out,PA}(t)$ is so the sum along time of multiple SiPM integrated pulses R_{SiPM}(t) with different amplitudes, corresponding to the scintillation photons that hit the SiPM active area at different times, which follow the S(t) scintillation distribution.
In Fig.5.9, an example waveform collected by a SensL MicroFB 60035 + Preamplifier (SSP module - differential voltage amplifier) from a cosmic ray crossing LAr volume in TallBo experiment at Fermilab is shown. [75]

The leading edge of the signal would be the sum of the first pe pulses from the singlet decay, followed by a number of smaller pulses from the triplet decay.
The average signal over many $V_{out,PA}(t)$ waveforms collected for similar events, producing almost the same total number of photoelectrons (e.g. a cosmic muon crossing the LAr volume), would have approximately the shape of S(t), the scintillation time distribution.

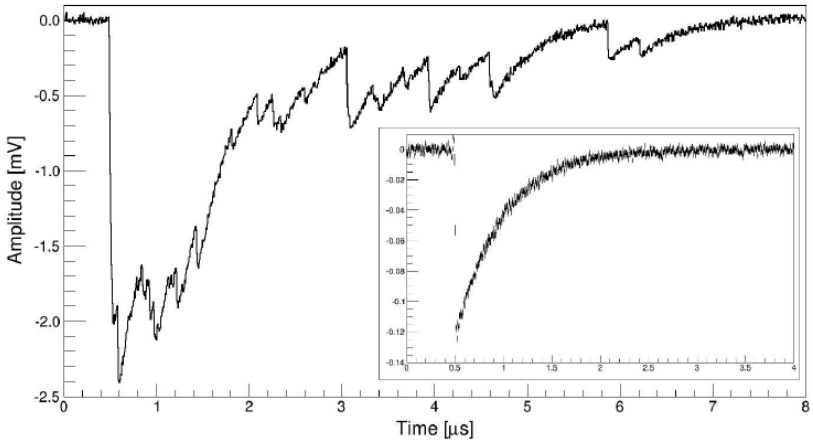

Figure 5.9: An example waveform from scintillation light generated by a single-track muon in LAr selected by the trigger in TallBo, recorded by SiPM. The early light multi-pe pulses and the subsequent few-pe pulses are sums of single pe pulses convolved with the SiPM's single microcell response function. Inset: Average single-microcell response for a SensL MicroFB 60035 in LAr.[75]

5.2 SiPMs in LArIAT

There is a great interest and effort in SiPM commercial production & development.
We have decided to use and test devices from different producers in LArIAT:

- Hamamatsu:
  - one output: fast response SiPMs (rise time: few ns, recovery time: 20-50 ns at room temperature, 300 K)
  - single channel and multichannel SiPMs
  - developing UV-sensitive SiPMs for LXe scintillation light (λ=178nm) collection; they might move on producing LAr scintillation light sensitive SiPMs too.

- SensL:
  - two outputs: standard output (calorimetric info) and **fast output**
  The SensL Fast Output is an interesting feature. It is the derivative of the internal fast switching of the pixel in response to the detection of a single photon (rise time: 300 ps - 1 ns, pulse width: 600 ps - 3 ns). The signal charge injected into the fast output ia a few % of the SiPM charge generated during the avalanche, but the pulse width is $\approx$ 100 times smaller than the standard output one. So the high current amplitude, combined with lower output capacitance, make the

device suitable for photon counting and timing purposes. (See Fig. 5.10)
- single channel and multichannel SiPMs

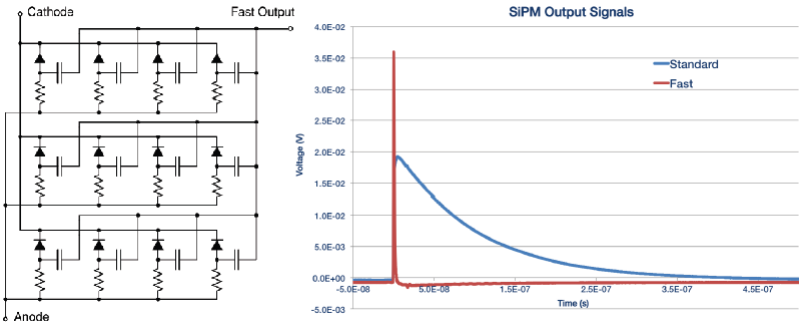

Figure 5.10: SensL SiPM Micro FB-series: Simplified microcell level schematic of the SiPM and standard output signal (blue) compared with fast output (red) for a 3mm x 3 mm SiPM illuminated with a 40ps laser pulse (Scope input = 50Ω). [77]

The SiPMs that are now used for detection of scintillation light in LArIAT are two Hamamatsu MPPC and one SensL.

The **Hamamatsu SiPM: MPPC Array S11828-3344M** [76] is a monolithic MPPC array of 16 channels anode output; each channel is connected to 3600 pixels, with 50 μm pixel pitch.
The effective photosensitive area is 3x3 mm^2 for each channel. The breakdown voltage is about +70 V at 300 K (room temperature). From the datasheet: FF=61.5%, PDE=50% at λ_{peak}= 440nm, dark current 1μA per channel (at 300 K), Gain=7.5 × 10^5.

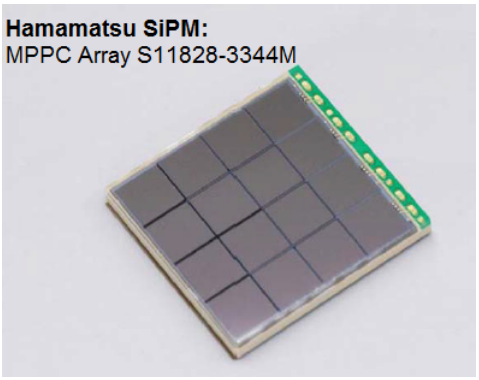

Figure 5.11: Picture of Ham.SiPM S11828-3344M.

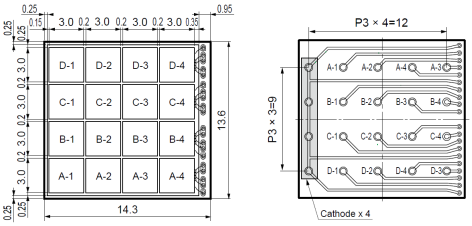

Figure 5.12: Ham.SiPM S11828-3344M Pixels and anode/cathode pads.

The **SensL MicroFB 60035** [77] is a 6x6 mm^2 single channel SiPM, with 35 μm pixel pitch . This SiPM has three pins, giving access to the fast output as well as the anode and cathode, and two other pins not connected.
The breakdown voltage is about + 24.5 V at 300 K (room temperature), with overvoltage range 1-5 V. From the datasheet: PDE= 31% (ΔV=+2.5 V) - 41% (ΔV=+5.0 V) at λ_{peak}= 420nm, dark current 10-24 μA (at 300 K), Gain= 3.0 $\times$ 10^6 and Fast Output Gain= 4.3 $\times$ 10^4 at ΔV=+2.5 V.

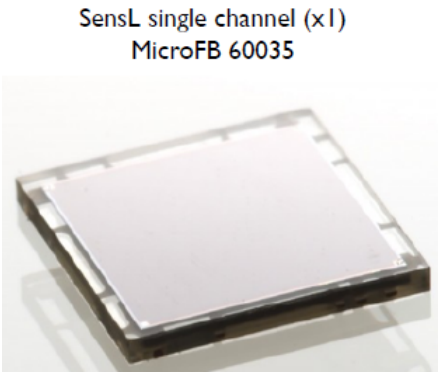

Figure 5.13: Picture of SensL MicroFB 60035.

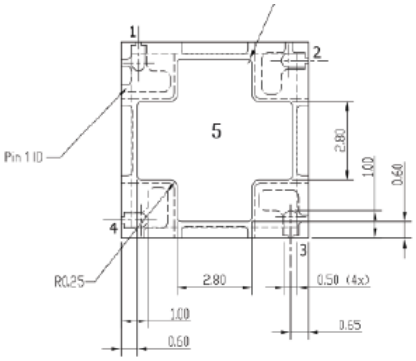

Figure 5.14: SensL MicroFB 60035 anode/cathode pads.

5.2.1 Bias and preamplification boards

The common approach fro SiPM front-end electronics consists in reading SiPM anode signals directly without a preamplification stage or with that stage put outside of the dewar, using warm electronics.
We decided to follow a new different way, reading SiPM signals with **front-end electronics** (amplification-integration step) **directly deployed in LAr** working at cryogenic temperatures.
So we would need cold electronics.

At that point the SiPMs voltage bias circuit and one stage of PreAmplification had to to be designed, produced and tested.
Together with Will Foreman (Univ. of Chicago), we designed the bias and preamplification circuit for these SiPMs.
We made a schematic design of the circuits using ExpressSCH software and then we made the project for the real circuits on a 4-layers Miniboard using ExpressPCB software. [78]
For the bias circuit we used high frequency filtering capacitors and a load resistor; then we collect the output signal from the detector by the anodes of the SiPM, connected together in parallel for the Hamamatsu Arrays.
We decided to use three different operational amplifiers for the three SiPMs we had, in order to see which one would give us the best signal amplification together with time response. The schematic designs of the three readout boards are here described and they are shown in Fig.5.15, Fig.5.16 and Fig.5.17.

For Hamamatsu arrays, we tried two different amplification schemes:

- SiGe MMIC amp (BGA616) [79] AC coupled to the detector,
- Traditional transimpedance op-amp in inverting mode (ADA4891) [80].

For SensL, we used the suggested circuit from the manufacturer provided manual:

- Traditional transimpedance op-amp in inverting mode (OPA656)[82]

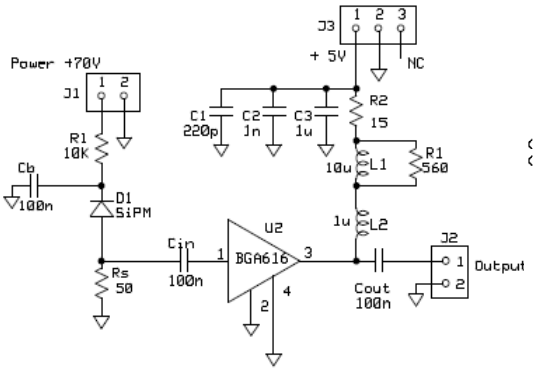

Figure 5.15: Schematic circuit for Hamamatsu SiPM + BGA616 [81].

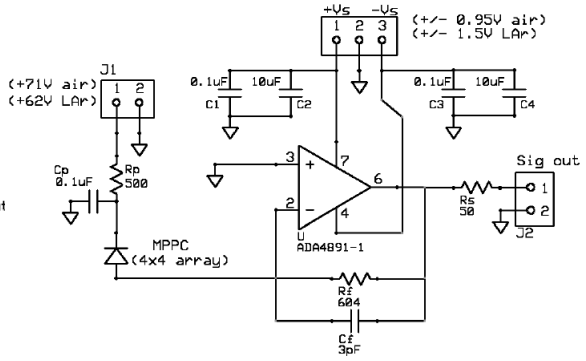

Figure 5.16: Schematic circuit for Hamamatsu SiPM + ADA4891

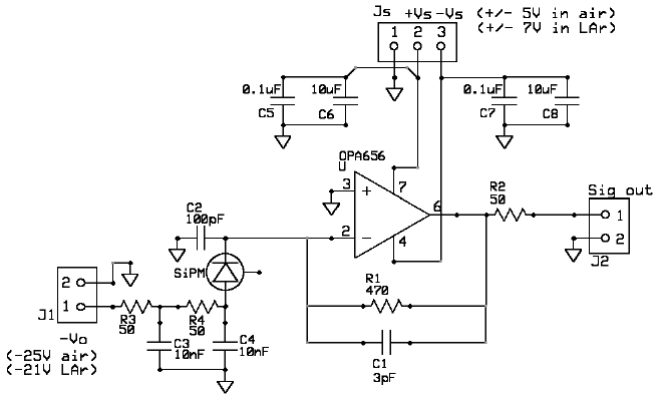

Figure 5.17: Schematic circuit for SensL SiPM + OPA656

Since the SiPMs with their front end boards had to be put inside the LAr cryostat, with F.Cavanna, E.Kearns, W.Foreman we chose stable capacitors and resistors that could work well even in cold temperatures, as in Liquid Argon (90 K).

When the PCB Miniboards we designed were ready, we had to solder all the electric components on them.
Because of the small size of all the components (resistors, capacitors, inductors, amplifiers) we made micro solderings by hand helped by a microscope to focus on the pads we have to put the pieces on.

The SiPMs were soldered via reflow station in order to have a good matching between the underside connection pins and the pads on the boards and the same time avoiding the risk of damaging the SiPM active surface. Reflow soldering is a process in which a solder paste (a sticky mixture of powdered solder and flux) is used to temporarily attach one or several electrical components to their contact pads, after which the entire assembly is subjected to controlled heat, which melts the solder, permanently connecting the joint. The goal of the reflow process is to melt the solder and heat the adjoining surfaces, without overheating and damaging the electrical components.
The soldering of each anode pad was then tested. For the Hamamatsu Arrays, they were covered with a black mask with a little hole with the dimensions of a single channel; after a single channel was selected, it was lighted the SiPM with a blue SMD LED (λ_{LED}= 470nm, comparable with the peak sensitivity wavelength for the Hamamatsu SiPM, λ_{peak}= 440nm (PDE= 50%)). The output voltage and the dynamic resistance were measured and, when the channel was fired with LED, they were less than in the case the LED was off, as expected is the soldering of the SiPM anode pins on the pads on the PCB board was well done.

Figure 5.18: Soldering station

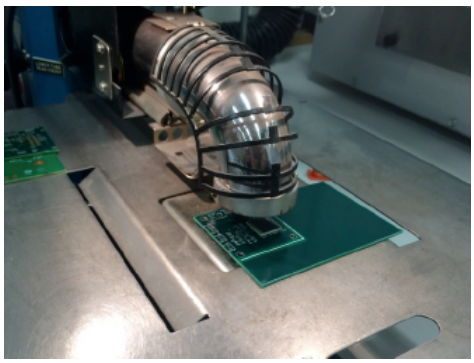

Figure 5.19: SiPM reflow station

5.2.2 Test of the boards coupled with BC-408 scintillator

The first test we did with the SiPMs boards was making an optical coupling between them and a BC408 plastic scintillator paddle and seeing the SiPM response to scintillation photons produced in the BC408 by crossing cosmic rays. This test was performed at room temperature (300 K).
The BC408 paddle was wrapped in reflective Al-Mylar and then in black tape, leaving opened only two windows for the SiPMs that were matched onto them with silicon optical grease. See Fig.5.20 and 5.21.

- Scintillator BC408:
  - Dimensions: 17 x 12 x 1 cm^3
  - LY(% Anthracene) = 64 (Anthracene,16500 $\frac{\gamma}{MeV}$)
  - λ=425 nm, scintillation light wavelength
  - λ_{att} =210 cm,attenuation lenght
- Reflective Al-Mylar covering:
  Reflectivity R_M = 94%

The coincidence of two PMTs coupled with scintillators was used as an external trigger for selecting cosmic muons. See Fig.5.22

Figure 5.20: Wrapping BC408 scintillator in Al-Mylar and black tape.

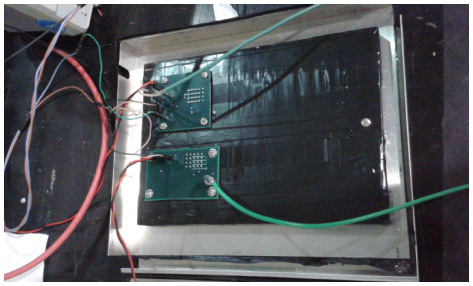

Figure 5.21: BC408 scintillator coupled with the two SiPMs.

The readout was done with digital scope Tektronix DPO5034 (2 GHz bandwidth, 10 GS/s-5Gs/s sample rate, advanced analysis and math capabilities).[84]
The estimate of single photoelectron response for the SiPM + BC408 paddle system, from the analytical calculation of the Light Yield (LY) of scintillation detector systems [83], is:

- Hamamatsu arrays (1.2x1.2cm^2): $\simeq$120 photoelectrons per passing muon in scintillator
- SensL (0.6x0.6cm^2): $\simeq$ 38 photoelectrons per passing muon in scintillator.

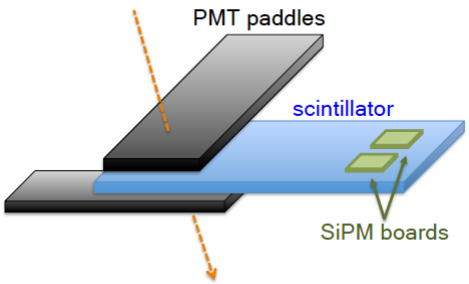

Figure 5.22: PMT paddles as trigger for Cosmic Rays crossing BC408 to which th SiPMs were coupled.

We collected pulse data from the scope (automated measurements of N samples and averaged waveforms) for the three SiPMs. The average waveforms from the three SiPM boards as a response to scintillation light produced by crossing muons are shown in Fig.5.23

A preliminary analysis of the shape of the waveforms we collected with the three different boards follows.
Since for the BC408 scintillator: τ_{rise} =0.9 ns, τ_{dec} = 2.1 ns, and these values are small compared to the SiPM response typical times, we can assume the time distribution of the photons in the BC408 scintillator S(t) as a Delta function S(t)=$\delta(t)$.
Then the SiPM + preamplifier impulsive response is R_{SiPM}(t), see Eq.5.9, with the nominal values (rise time, recovery time...) at 300 K.
The output signal $V_{out,PA}$(t) we expect from the preamplifiers should have almost the

same shape as the SiPM impulsive current response i_{ext}(t), see Eq.5.2, with higher amplitude, because of the feedback gain in the preamplifier circuit.

We can see in Fig 5.23 the BGA616 amplifier acts as a very fast and good integrator; the shape of the preamplified signal is quite close to the signal shape expected for Hamamatsu SiPM impulsive response i_{ext}(t) (Hamamatsu rise time $\tau_d \approx 5$ ns and recovery time $\tau_q = 50$ ns at 300 K); the amplitude corresponds to the number of photoelectrons produced by the collected photons for a crossing muon multiplied by the preamplifier gain.

The ADA4891 board appears to have a slower integrator response; in fact the rise time of the signal is higher than the Hamamatsu SiPM τ_d, while the fall time of the signal is reasonably comparable with τ_q of the Hamamatsu SiPM. The overall gain is lower than in the previous preamplification configuration.

The OPA656 preamplification stage on SensL SiPM apperas to act as a good integrator too, compared with the SensL SiPM expected i_{ext}(t) ($\tau_d \simeq 10$ ns and $\tau_q = 210$ ns at 300 K, see Fig.5.2). The preamplified signal is positive, since the SiPM direct signal that is driven into the preamplifier comes from the cathode pin (see Fig.5.17), instead of the anode as it's done for the Hamamatsu arrays, and so it's negative.

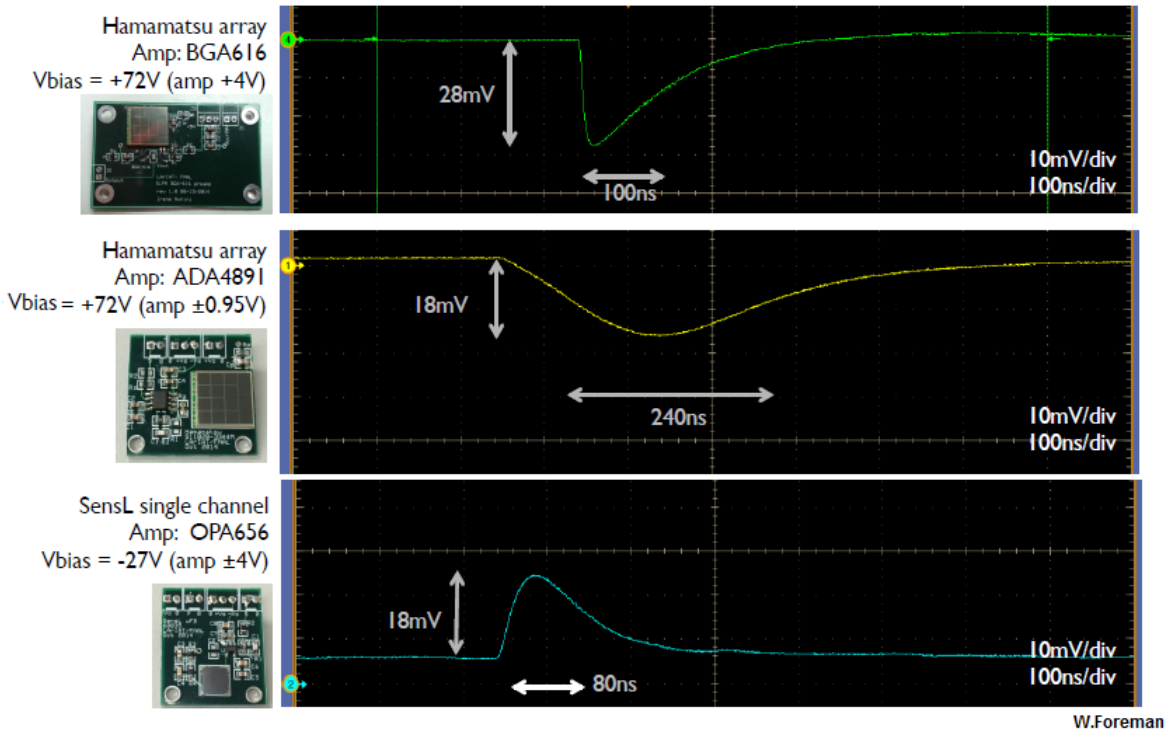

Figure 5.23: Average waveforms from SiPMs from CR signals in BC408 scintillator paddle.

5.2.3 Preliminary cold tests at Liquid N_2 Temperature

The second test we did with the SiPM boards was oriented to see their behavior at cryogenic temperatures.
The SiPMs were mounted on a holder and submerged in Liquid Nitrogen, at 77 K, a temperature close to the operating one of the LAr cryostat, facing down in the the dewar. Then we lighted the SiPMs with a pulsed blue LED. A fiber optic cable was attached to the LED pulser and brought down to the bottom of the dewar, a few cm in front of the SiPMs. (See Fig. 5.24)
The LED was Nichia NSPB300A - 3 mm blue, which was connected to a pulser electronic circuit, in which it was possible to select pulse width and light intensity.

While operating the SiPMs at that temperature, we figured out that they reached the avalanche region at less bias voltage than the nominal value at 300K as we were expecting, since V_{bk} decreases with lower temperature.

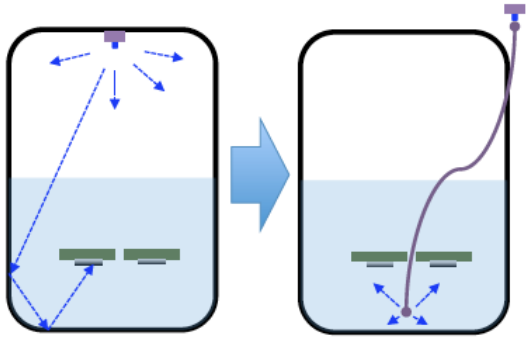

Figure 5.24: Schematics of SiPMs lighted by blue light from fiber optic in LN_2 dewar

We managed to obtain good signals from Hamamatsu ADA4891 board and SensL OPA656 board; instead we had problems with BGA616 board. We saw that even in cold, the gain was not rising and the noise was not suppressed for BGA616 board, as expected.

I found BGA616 amplifier works in Darlington configuration; the Darlington configuration is made by two bipolar transistors (BJT) with common collector and emitter.
The other two amplifiers are made with different electric technology:
- ADA4891 is a CMOS amplifier
- OPA656 is a voltage feedback operational amplifier with a FET-input stage.

I found that BJT technology has a worse behavior at LN_2 temperatures than MOSFET technology; basically in BJT transistors there is a strong decrease of the current gain at 77 K, because the bipolar transistor relies on thermal excitation of minority carriers to let conduction happen. Instead, CMOS technology is expected to work well at so cold temperature, because it is based on major carriers whose mobility is enhanced at lower temperatures.[85][86][87]
So the Hamamatsu SiPM was removed from BGA616 board and mounted onto one spare board with transimpedance inverting circuit with the OPA656 operational amplifier.

The **SensL SiPM board response in** LN_2 was characterized.
Many waveforms (data in ASCII format) of the SensL response to the pulsed LED that lightened the active area were collected with the digital scope Tektronix DPO5034.
An hit-finder C++macro was used to look for single photoelectron candidate pulses (using a rise-time cut, since the SiPM pulse rise time is expected to be almost 30 ns), define an integration window, calculate the "local" baseline per each pe candidate window, calculate the integral under those pulses and fill a SER histogram. See Fig.5.25; single photoelectron candidates have $\approx$ 1 mV amplitude for V_{bias} = - 26 V.
Single p.e. measurements (SER plots) for the SensL board at different bias voltages in liquid nitrogen were obtained, as shown in Fig.5.26 and 5.27.
The values in the x-axis are the integrals of amplitude of the pulses over time (V s). They need to be divided by scope load resistance R_L = 50 Ω to be converted in real charge Q (C).
Only the first 200 ns of the pulse for single pe candidates was integrated for the SER plots. To calculate the full integral out to 6 μs for those pulses, a single photoelectron average waveform was reconstructed. The estimate of what fraction of total charge was contained in 200 ns time window is : $Conv = \frac{\int_0^{6\ \mu s} V_{out,PA}(t)dt}{\int_0^{200 ns} V_{out,PA}(t)dt} = 2.8$, meaning $\approx$ 36 % of the total charge of each pulse is output int the first 200 ns of the SiPM response. The SER results were multiplied by this conversion factor to obtain the single pe pulse total integrated charge, see Eq.5.10.

$$Q = Conv \frac{\int_0^{200 ns} V_{out,PA}(t)dt}{R_L} \tag{5.10}$$

In the end the charge value Q corresponding to the single pe peak (and to the peaks spacing too) was converted in gain measurements, using Eq.5.3. See Table 5.1.

LN_2 results	V_{bias}	V_{bias}
	- 26 V	- 27 V
Single pe peak (nV s)	0.0749 $\pm$ 0.0003	0.0908 $\pm$ 0.0004
Single pe equivalent charge (nC) [converted]	0.00421 $\pm$ 0.00002	0.00508 $\pm$ 0.00002
Gain estimation	2.6 x 10^7	3.2 x 10^7

Table 5.1: Table of the SER results for SensL SiPM in LN_2. The subsequent peaks, corresponding to multiple photoelectrons, are fitted with a multiple gaussian distributions. The first peak ($\approx$ 0 Vns) corresponds to noise. The parameter p1 of the fit is the mean of the 1 pe gaussian distribution; it is also assumed as the peaks separation and corresponds to a single photoelectron equivalent charge.

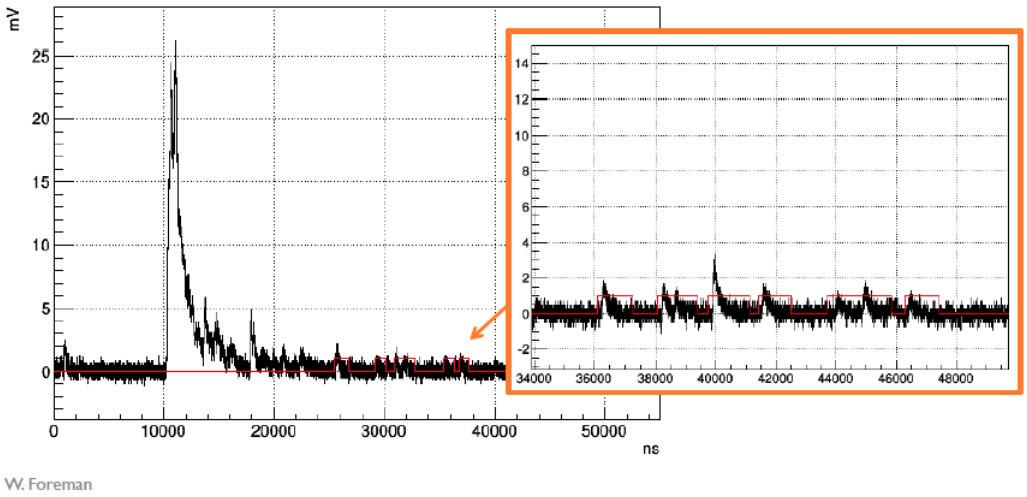

Figure 5.25: SensL waveform when lightened by blue pulsed LED and submerged in LN_2. Wide window in which the HitFinder operates (from 25 μs) and the single pulse windows.

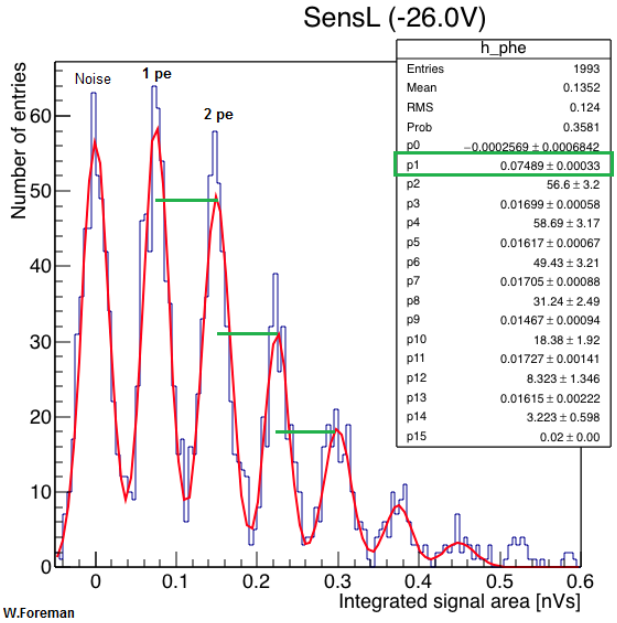

Figure 5.26: SER plot for SensL V_{bias} = - 26 V in LN_2.

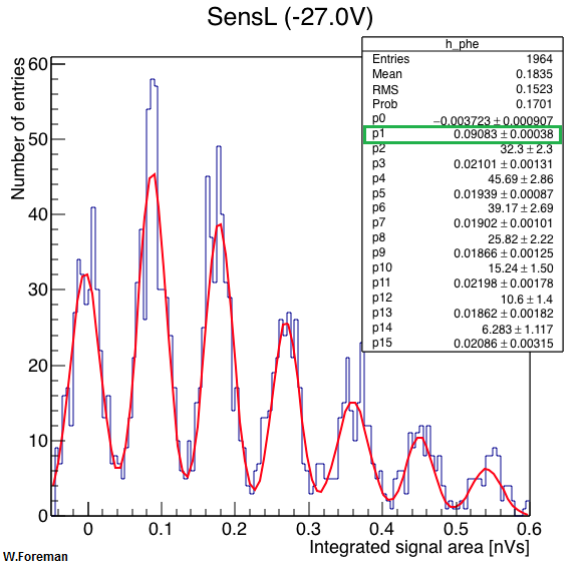

Figure 5.27: SER plot for SensL V_{bias} = - 27 V in LN_2.

5.2.4 Response of the SiPM boards in LAr

LArIAT's light collection system consists of an array of two PMTs and three SiPMs, as described in Ch.2 2.4. The optical devices are mounted on an internal flange of the cryostat and deployed in Liquid Argon. They sit behind the wire planes of the TPC. The assembled system mounted on the holder before being installed in the cryostat is shown in Fig.2.11.
During data collection from LArIAT first runs we have been able to see signals from the SiPMs boards deployed in LAr in the cryostat.
The aim is to characterize the SiPM boards response to LAr scintillation light and to get calibrations for them using photoelectrons in the tails of scintillation signals.

SensL board in LAr: Preliminary characterization with cosmics
The response of the SensL board was firstly tested with Cosmic Rays inducing scintillation in LAr.

Using the COSMICON Trigger (see Cosmic paddles position in Ch.2 Fig.2.5), cosmic muons that cross the TPC along the diagonal, Δx $\approx$ 100 cm, have been selected. These particles are expected to deposit almost 200 MeV energy and produce $\approx$ 8 x 10^6 scintillation photons while crossing the TPC volume.

The amount of scintillation light that would be collected by the optical devices depends on the TPB efficiency in wavelength shifting, on the fraction of area covered by the optical devices over the whole boundary surfaces of the TPC and on the SiPMs (and PMTs) intrinsic efficiencies.

- **SensL SiPM direct response to LAr scintillation light**
  The first study I've done was the characterization of the shape of the **direct SiPM signal**, without the preamplification stage.
  The SensL was biased at -26 V, 5 V overvoltage.
  Several SensL waveforms of Cosmic Triggers (COSMICON trigger) have been collected by the v1751 Waveform Digitizer module (board1 Ch4 for the SensL SiPM) (1 Gsample/s sample frequency; 7.168 μs and 14.336 μs time window). For fixed sampling windows, an averaged waveform with its associate error was computed from the collected waveforms. Since the baseline in V1751 board collected waveforms was not zero, each single waveform was firstly corrected subtracting its own baseline. To calculate the baseline the samples in the first 2 μs before the signal rising edge have been fitted with a linear dependence, with slope parameter close to zero. Then the averaged waveform was reconstructed.
  In Fig.5.28 a single waveform for a cosmic in LArTPC volume collected by v1751 module is shown, while in Fig.5.29 there is the averaged waveform (number of collected waveforms N_{wfm}=100). The collected SensL SiPM direct signals are negative, since for the SensL device we're reading out the signal from the cathode pin instead of the anode (see Fig.5.17).

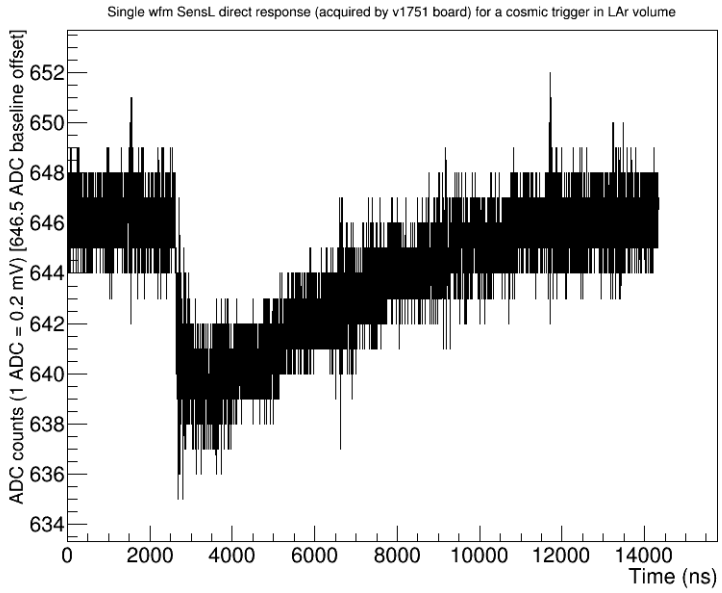

Figure 5.28: Single waveform for SensL SiPM direct response to LAr scintillation light produced by a cosmic trigger in the LArTPC volume. The waveform has been collected with v1751 Waveform Digitizer board.

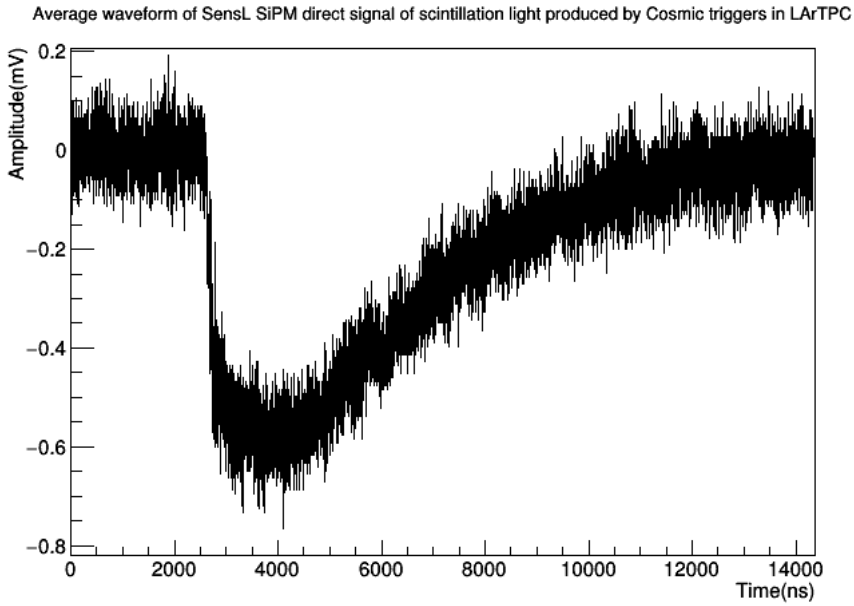

Figure 5.29: Average waveform for SensL SiPM direct response to LAr scintillation light produced by a cosmic trigger in the LArTPC volume. (Baseline offset corrected and amplitude converted from ADc values to mV)

The averaged waveform in Fig.5.29 is expected to have almost the shape of the V_{out}(t) signal in Eq.5.7.
For a more accurate study of shape of the SensL direct response average waveform to scintillation photons produced in LArIAT TPC by crossing cosmics, we should take in account for a few more things.
Firstly, since we're shifting the wavelength of scintillation photons to optical using TPB coating, we have to take in account also for the intermediate time constant $\tau_I = 34$ ns introduced by this reflector on the light distribution S'(t), see Eq.1.23.
Moreover, we are collecting photons that could be produced very far from the optical detector, since the TPC active volume is not small and the scintillation photons can travel inside the TPC and experience multiple reflections before reaching the photodetectors sensitive area. For this reason the real photon distribution that is detected by the photodetectors is the convolution of the "ideal" scintillation photon distribution S'(t) and a gaussian distribution G(t) which takes in account for the time spread of the photons from their production time and their collection time.
This appears to affect the ideal distribution in terms of a smearing of the fast and intermediate scintillation components under the gaussian shape. The expected photon distribution S"(t) that would be detected in the LArTPC is shown in Eq.5.11 and Fig.5.30.

$$\begin{aligned} S''(t) &= G(t,\sigma_{LC}) \otimes S'(t) \\ G(t,\sigma_{LC}) &= \frac{1}{\sigma_{LC}\sqrt{2\pi}} e^{-\frac{t^2}{2\sigma_{LC}^2}} \end{aligned} \tag{5.11}$$

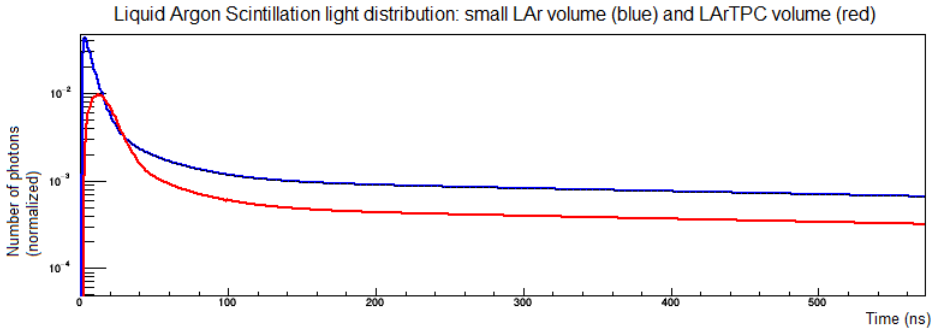

Figure 5.30: Expected scintillation photons distribution S"(t) (red curve) that would be detected in the LArTPC volume. The photons time spread σ_{LC} for the gaussian distribution G(t) has been assumed σ_{LC}=10 ns (from LArIAT PMT's preliminary results). The blue curve corresponds to the "ideal" scintillation photon distribution S'(t).

So the averaged waveform from the SiPM associated with the scintillation light produced by a charged particle (as a cosmic) crossing the LAr TPC volume and then collected by the photodetector is expected to have the shape of the one shown in Fig.5.31. The analytic expression is the convolution of the scintillation signal S"(t) and the impulsive (single pe) current response of the device i_{ext}(t), see Eq.5.12 and Fig.5.31.

$$V_{out} \approx S''(t) \otimes (i_{ext}(t) R_L) \tag{5.12}$$

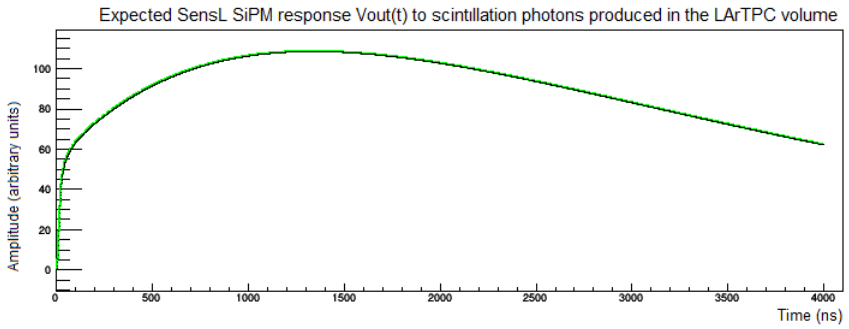

Figure 5.31: Expected SensL SiPM waveform V_{out}(t) for scintillation photons produced by a MIP in the LArTPC volume and then collected by the SiPM. The values that have been used: σ_{LC} =10 ns (from LArIAT PMT's preliminary results), τ_q=2.5 μs.

In Fig.5.32, the expected SensL SiPM waveform in Eq.5.12, with inverted polarity, has been superimposed to the average waveform for SensL SiPM direct response to LAr scintillation for a cosmic trigger in the LArTPC volume in Fig.5.29.
We can observe there is a pretty good agreement between the real average SensL SiPM waveform and this expected shape of the signal, that has be obtained taking in account for the LAr scintillation photons distribution, for the time spread of the light collection in the TPC and for the expected SensL SiPM features in cryogenic environment.
Next step to better characterize this shape of the SensL SiPM signal and its parameters would be to use the analytic expression of the expected waveform in Eq.5.12 directly as a fit function for the average waveform collected for cosmics (Fig.5.29).

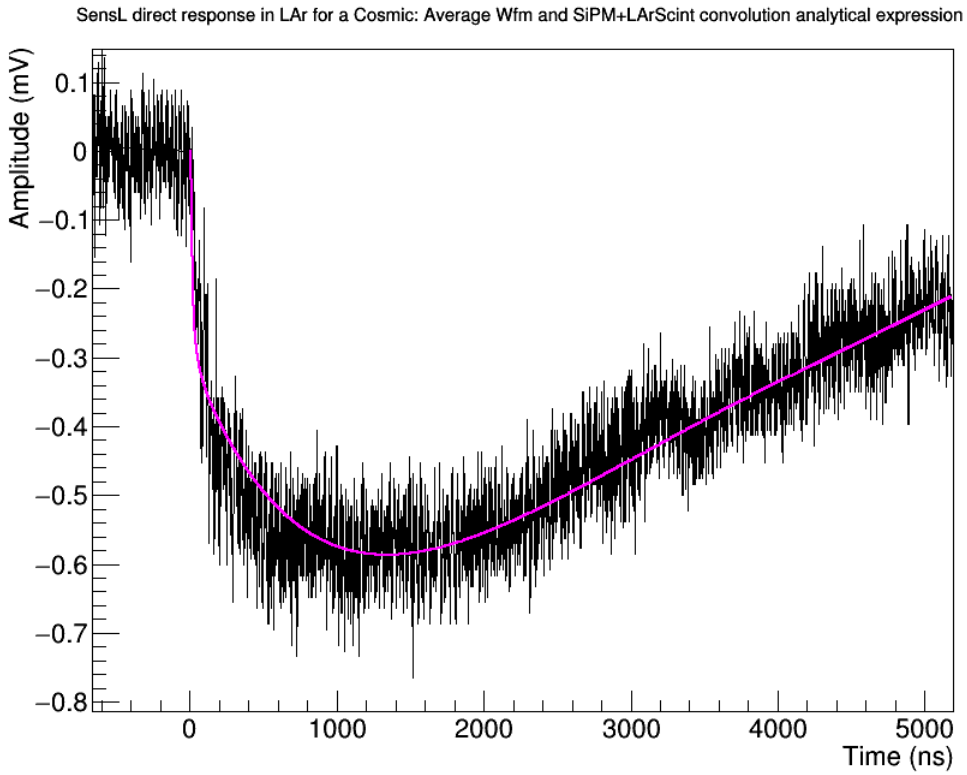

Figure 5.32: Average SensL SiPM waveform and expected signal from Eq.5.12 superimposed (Magenta curve) for scintillation photons produced by a MIP in the LArTPC volume and then collected by the SiPM. The first 5 μs of the signal are reported, to better show the rise time features of the signal: a fast component, mainly linked to the gaussian distribution of the light collection in the TPC, and a slow component due to LAr late light emission.

- **SensL SiPM + OPA 656 response to LAr scintillation light**
  After this preliminary characterization of the direct SensL SiPM response to LAr scintillation light, we've powered on the operational amplifier and collected many waveforms from cosmic triggers (COSMICON trigger).
  We've done some preliminary studies. The aim was making the average waveform of these signals, to extract the LAr scintillation time dependence from that as well as studying the tails of each single signal to look for single photoelectrons to have a calibration of the device in LAr.

  The SensL SiPM was biased at -26 V (and -25 V, -27 V) and the OPA656 amplifier was biased at $\pm$ 8 V.
  In Fig.5.33 a single waveform for a cosmic in LArTPC volume is shown, while in Fig.5.34 there is the averaged waveform (number of collected waveforms N_{wfm}=100).

  In the single waveform in Fig.5.33 we can see multiple peaks with different amplitudes. The leading edge of the signal is expected to correspond to the number of scintillation photons that are produced and collected in the first few ns (fast light photons that hit the SiPM microcells within almost the time response of the SiPM). In the first microseconds, other multiple photoelectrons pulses are present, which correspond to the contribution of all the three components of the scintillation (τ_F, τ_S, τ_I) convolved with the collection time in the TPC. Then in the tail of the signal only single photoelectron pulses, due to LAr scintillation late light, are expected; eventually 2 photoelectron pulses, due to crosstalk, can be present.

  The average signal for cosmic triggers, in Fig.5.34, has actually a shape that is consistent with S"(t) scintillation light time distribution, discussed before (see Eq.5.11) considering the TPB wavelength shifting effect and the time spread of the light collection inside the TPC volume). There is a quite sharp peak in the first 100 ns, due to SiPM response, light collection time spread and fast and intermediate scintillation components, and slow exponential component, which is mainly dominated by the late late LAr scintillation component but is affected a bit by the long recovery time of the SiPM at 90 K.

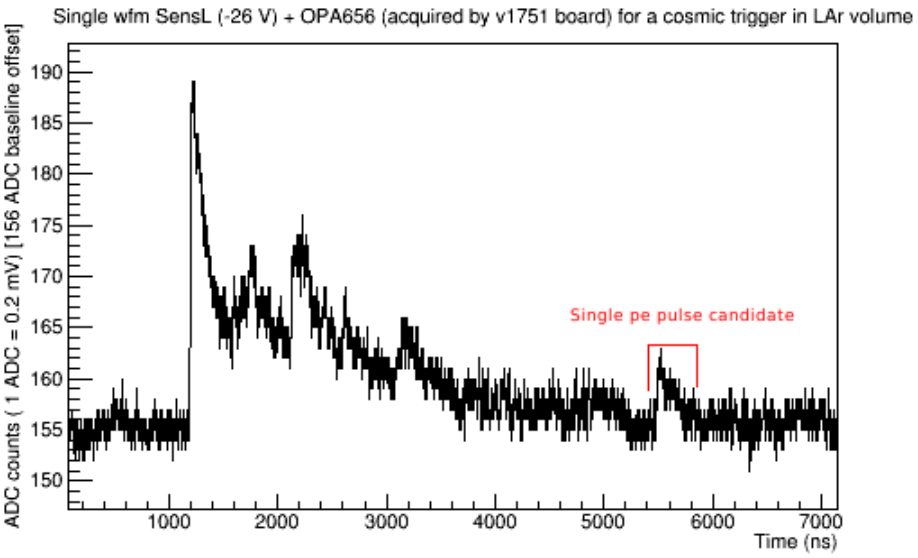

Figure 5.33: SensL (V_{bias}= - 26 V) + OPA656 single waveform for Cosmic Trigger. Single photoelectron pulse candidate on the tail is marked with red line.

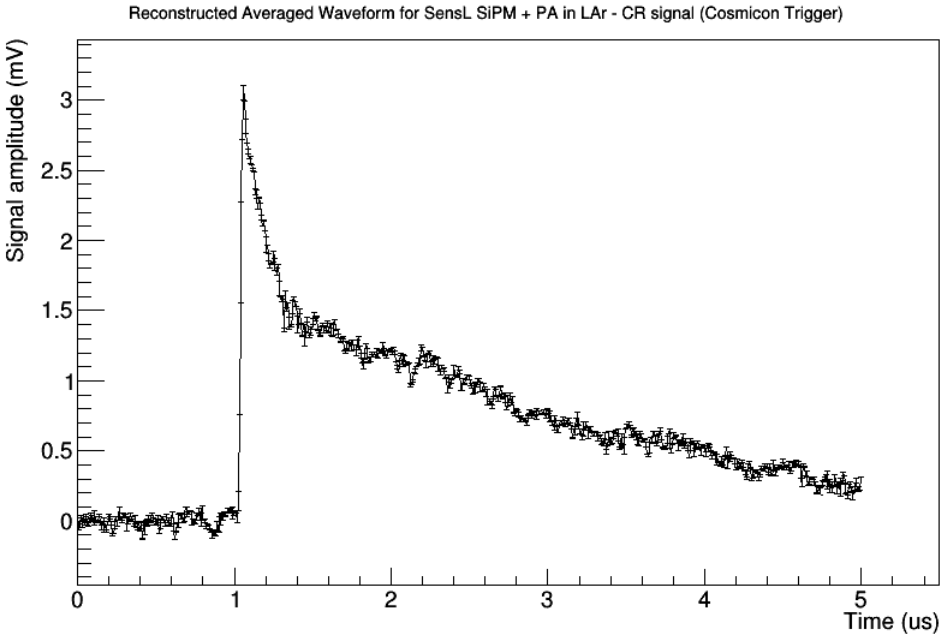

Figure 5.34: SensL (V_{bias}= - 26 V) + OPA656 average waveform for Cosmic Triggers.

Lately we've tried to get out an estimate of the **single photoelectron response** of the SensL SiPM + OPA656 in LAr (90 K) to compare with the results in LN_2 (77 K).

The SiPM was biased at -27 V and the amplifier was powered at ± 8 V; we've chosen to bias the SiPM at a higher voltage, expecting to see single photoelectrons pulses emerging more easily from baseline noise.
Almost 1000 waveforms were collected with Tektronix DPO5034 scope for different triggers, since we're looking for single photoelectron pulse candidates in the signal's tails.
Each waveform was corrected for its baseline offset and converted the amplitude from ADC counts to mV. An hit-finder C++ code was used to look for single photoelectron candidate pulses along the amplified signal's tails.
The pulse finding starts 8 μs later than the trigger - leading edge peak of the signal- to be sure to catch only LAr late light single photons. Since the expected single photoelectron signals were small and comparable with the baseline noise band and fluctuations, a rise time cut has been added, since the SiPM pulse is expected to get to its maximum in almost 30 ns, and a fall time check. A 200 ns integration window for each pulse candidate was defined and then the integral under those pulses was calculated and the value of this area was used to fill a SER histogram.
With this time window (very late signals, later than 8 μs from the trigger) and these selection criteria on the pulse, only the single pe peak is expected (and maybe a possible 2 pe peak due to crosstalk), since the noise fluctuations would not pass the selction criteria on the shape of the pulse. The SER plot obtained for the SensL SiPM in LAr is shown in Fig.5.35.

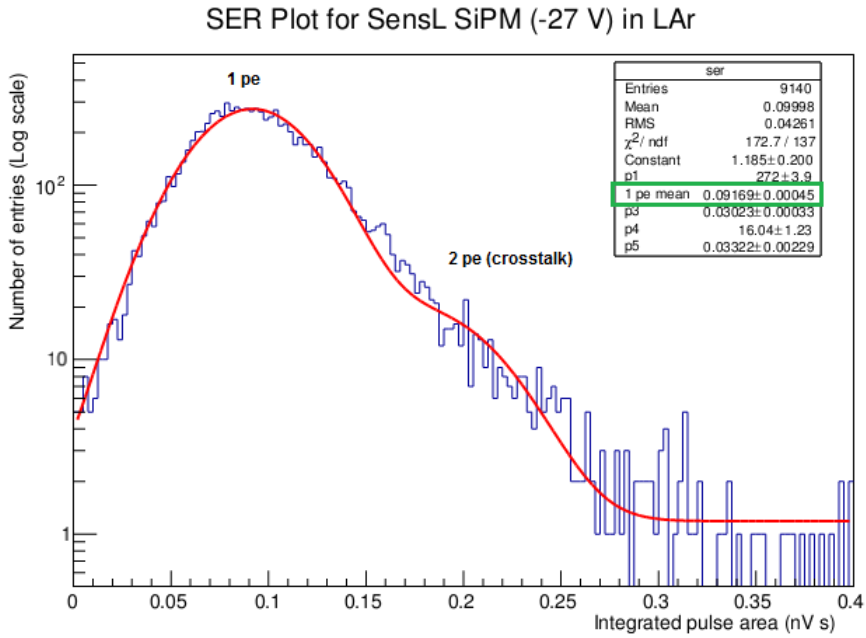

Figure 5.35: SER plot for SensL (V_{bias} = - 27 V) + OPA656 in LAr. (Y axis is reported on Log scale)

Since only the first 200ns of each single p.e. window were integrated (as it was done for the tests in LN_2), we need to convert the integrated area in this window into the value of the total integrated area over a whole single pe pulse (see Eq.5.10). The conversion factor found from LN_2 tests was $Conv \approx 2.8$.
The SER plot has been fitted with a double gaussian distribution, to look for the single pe and eventually for a 2 pe peak, due to crosstalk.
In Table 5.2 the SER plot fit results are reported.

LAr results	V_{bias}
	- 27 V
Single pe peak (nV s)	0.0917 ± 0.0004
Single pe equivalent charge (nC) [converted]	0.00513 ± 0.00002
Gain estimation	3.2 x 10^7

Table 5.2: Table of the SER results for SensL SiPM in LAr. The parameter "1 pe mean" of the fit is the mean of the single pe gaussian distribution; it is also assumed as the peaks separation and corresponds to a single photoelectron equivalent charge.

The single pe equivalent charge and the gain estimation for the SensL SiPM (V_{bias} = - 27 V) in LAr and in LN_2 are in extremely good agreement. See Table 5.1 and 5.2. A different setup for providing and collecting single or multiple photoelectrons (pulsed LED in a LN_2 dewar and LAr late scintillation photons in the LArTPC volume) does not affect the evaluation of the single pe SiPM response as well as a $\approx$ 10 K temperature difference does not change the overall SensL SiPM gain.

Moreover we can have an estimate of the **crosstalk effect** in the SiPM from the 2 pe peak amplitude, compared with the single pe amplitude. The percentage of the ratio of the two of them is almost 7 % (ΔV = + 5.0 V for V_{bias} = -27 V in LAr); this appears to be a reasonable crosstalk estimate, compared with the crosstalk nominal values for the SensL MicroFB 60035 given in the datasheet (7% for ΔV = + 2.5 V and 14% for ΔV = + 5.0 V at room temperature 300 K), especially considering that the crosstalk probability has a slight reduction at low temperatures, due to a lower PDE for the wavelength of the crosstalk photons produced during the avalanche.[69]

From the integral over the average SensL (V_{bias} = -26 V) + OPA656 waveform, in Fig.5.34, and the single pe pulse charge, we can have an estimate of the average number of photoelectrons/photons detected by the SiPM in the LArTPC for a crossing muon and so the **SiPM Light Yield in the LArTPC**.

The total area under the reconstructed signal in Fig.5.34 is $\approx$ (3.4 ± 0.2) nVs; we have to take in account that here we've reconstructed only the first 4 μs of the real pulse, which would probably last almost 3 μs more. A preliminary estimate of the total charge under the SensL+ OPA656 average cosmic ray signal is thus: (4.5 ± 0.5) nVs.
The SER results in LAr we have are for the SiPM biased at -27 V, while the average waveform has been made on signals collected when the SiPM was biased at -26 V.
Since it's clear there is a complete agreement between SER results for the SensL in LAr and LN_2, we can assume the single pe pulse area in LAr at V_{bias}= - 26

V as (0.0749 ± 0.0003) nVs, the value obtained for LN_2 . So it looks like the crossing cosmic events yield ≈ 25 pe on the SensL.

It appears this result from the cosmic event is consistent with early LY results from the ETL PMT. Taking area and QE into account, the ETL PMT should see 37 times more light than the SensL SiPM. From integrating the multiple photoelectron ETL pulses, Will's estimate of ETL LY in LArTPC volume is ≈ 4 pe/MeV, which would predict the SensL's LY to be 4/37 of the ETL value:

$$LY_{SensL} \approx 0.10\text{pe/MeV (from ETL/SiPM estimate)}$$

From SensL + OPA656 integrated area result:

$$LY_{SensL} = 25 \text{ pe } / \text{ 200 MeV (crossing muon)} = 0.12 \text{ pe/MeV}$$

There is a pretty good agreement.
A preliminary estimate of the total LY of all the optical systems in LArIAT (two PMTs and the three SiPMs) from MC simulations was ≈ 50 pe/MeV. The expected fraction of this value due to the SensL SiPM was 0.25 pe/MeV, which is almost factor two higher than the preliminary LY_{SensL} value obtained experimentally; probably there are some leaks and some screening, especially due to the TPC wire planes, in the real experimental setup that were not completely taken in account in the light collection system simulation.

5.3 The ongoing development: Matrices of SiPMs

After the first tests with the SiPM boards in LN_2 temperature and while waiting for LArIAT run and first results in LAr, we started thinking about how to improve LAr scintillation light collection efficiency with SiPM devices.

At the moment there is a lot of R&D in several research groups to carry out matrices of SiPMs for light detection.
This should be a goal also for other LAr short-baseline experiments, like SBND [88]. In SBND the full LAr volume is planned to be surrounded by a scintillation light collection system. One proposal is to use cryogenic UV-PMTs, which are very expensive and very sensitive to the environmental conditions (temperature, humidity, power supply stability...) and to magnetic fileds. If we could demonstrate that we can manage to have matrices of SiPMs which can cover the same area as PMT photocatode (2"-3" diameter) and could still have good timing and charge resolution with proper readout electronics, the SBND project might switch their light collection plans from PMTs to SiPMs.

Development of SiPMs matrices should be a useful and interesting prospect, because, despite the small dimensions of single SiPMs, we can obtain large active detection surfaces by using several of these in a grid and we do not have to deal with increasing noise effects as crosstalk and dark noise, maintaining good timing and charge resolution which depend on single SiPM capacitance (small SiPM area - small capacitance).

Before moving to the design of readout layout for SiPMs matrices, we compared the possibility of using single channel SiPMs or SiPM Arrays devices. Eventually we have decided to use **SiPM Arrays** for filling the matrix, instead of single channel SiPMs, for

large total active area for each device but less capacitance (small single channel area). [89]
In Fig.5.36 there is a schematic representation on how we can move from a single channel SiPM to a SiPM matrix that can have an active area comparable with a PMT photocathode (2"-3" diameter).

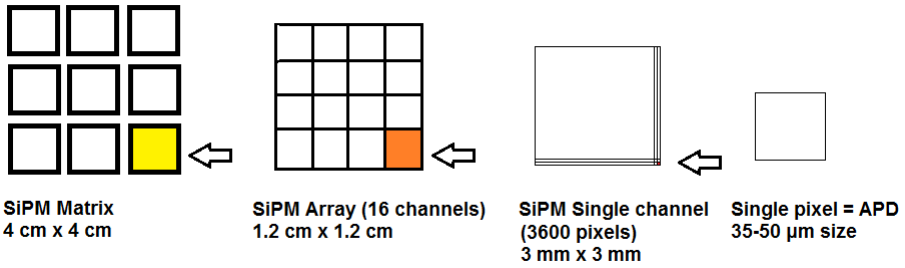

Figure 5.36: Schematic representation in scale: from single pixel (Avalanche Photodiode) to a SiPM Matrix.

At this point it has been necessary to figure out which kind of front-end electronics layout should be suitable for us to read all the signals coming from the SiPMs matrix. If we sum up together all the anodes of the channels of SiPM Arrays in the matrix ad then amplify that signal, we'd have higher

$$C_{det} = \Sigma_i C^i_{ch}$$

So we could use for the standard output amplifiers with less bandwidth but in this way we loose the time features of the SiPM signal (higher rise time of the signal, difficulties in pulse shape discrimination without the preamplification stage and difficulties in photon counting) and we can expect a worsening in charge resolution - $\frac{S}{N}$ ratio.
Otherwise we can amplify each single channel; that would need very many amplifiers (we should expect that all of them have exactly the same behavior) and could make the board design complicated, but would get good timing and charge resolution.
Therefore we have to find a compromise towards these two solutions.
This is the reason why we have designed several readout configurations to test, as described in next paragraph.

5.3.1 SiPMs Arrays and front-end electronics

After having decided to go for SiPM arrays, we have chosen the **SensL SiPM ArrayC-30035-16P** [90] [91].
The ArrayC-30035-16P-PCB is composed of 16 individual 3mm SMT sensors arranged in a 4 × 4 array. The single pixel (APD) dimension is 35 μm. Each channel is made by 4774 microcells- pixels; it has 3 × 3 mm^2 active area, while the channel pitch is 4.2 mm. The board size is 16.6 × 16.6 mm^2.
Connections to each channel are provided by a 40-way DF17(2.0)-40DP-0.5V(57) connector. This connector mates with the DF17(3.0)-40DS-0.5V(57) receptacle. The 16 SiPM channels have all substrates (cathode for C-Series sensors) connected together to form a common I/O. Each individual fast output and standard I/O (anode) are routed to its own output pin. The 40-way connector provides connections as follows:

- 16 x fast output
- 16 x standard I/O (anode)
- 8 x common I/O (cathode)

In Fig.5.37 are shown the signal connections at the channel level in the SMT Arrays and in Fig.5.38 the SensL SiPM ArrayC-30035-16P is shown.

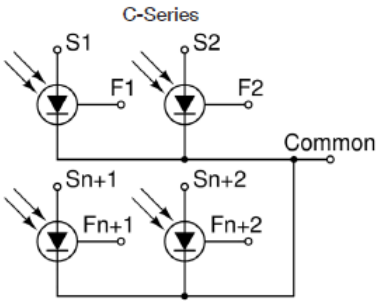

Figure 5.37: Signal connections at the channel level in the SMT Arrays: SensL SiPM Array C-Series [90].

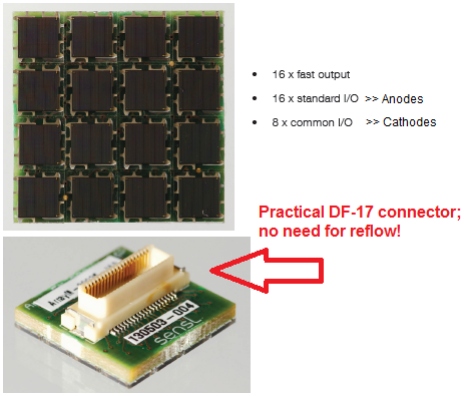

Figure 5.38: SensL SiPM ArrayC-30035-16P [91].

For MicroC-series SensL SiPMs, the nominal V_{bk} is 24.2-24.7 V, the recommended overvoltage is 1.0-5.0 V, the peak wavelength λ_{peak}=420 nm.
For 3 mm channels at room temperature (300 K): the photon detection efficiency PDE at λ_{peak} = 31 % (Δ V = + 2.5 V), 41 % (Δ V = + 5.0 V), the Gain is 3 $\times$ 10^6 (Δ V = + 2.5 V), the fast output rise time is 0.6 ns, the microcell recovery time τ_q is180 ns, the anode to cathode capacitance C_{ch}=850 pF (Δ V = + 2.5 V). [92]

One of the reasons we've chosen these devices is because they have that practical DF-17 connector that would make easy to match the SiPM on the PCB readout board without having to follow the reflow procedure. This connector is supposed to work well at LN_2 temperature; we aim to test and verify this.

As we did for Hamamatsu SiPM arrays and for the SensL single channel SiPM, there are actually deployed in LAr cryostat, we've designed **dedicated front-end electronics** that would be supposed to work in cryogenics for these SensL Arrays too.
In Fig.5.39 there is a schematic representation of a simplified readout circuit for the SensL Array C-series we've designed. The standard output- anode (for each channel)

is read with a transimpedance inverting circuit (with ADA4981-1 operational amplifier [80]) which acts as a fast integrator on the SiPM current signals. The fast output, which is referred to the cathode substrate to which we apply the bias voltage $+V_b$, needs C_0 capacitor to be referred to the ground and it's not amplified, but we use a transformer T1 for impedance matching for driving the signal out along the wires.

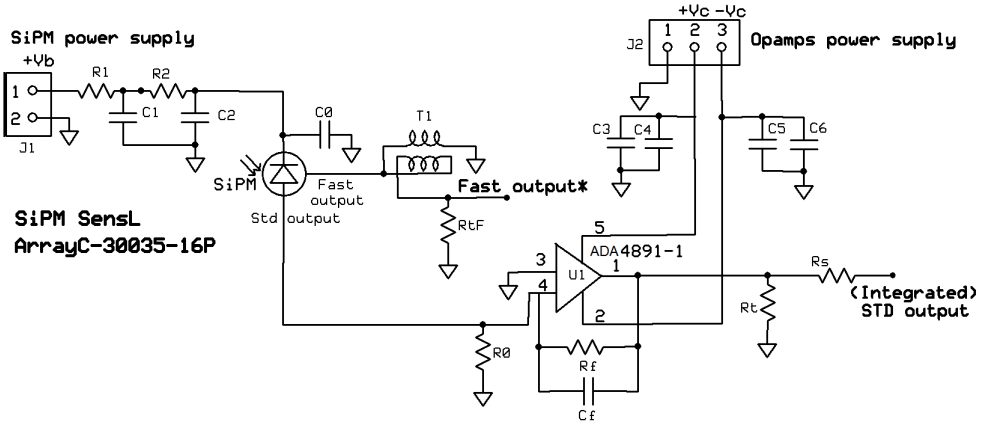

Figure 5.39: Simplified schematic readout circuit for SensL SiPM ArrayC-30035-16P

We've realized four readout configurations to characterize SiPM array response (std and fast output) and noise contribution to the signal for these different layouts.
Two of them are for a single array (see Fig.5.40):
- All channels std outputs summed up and then amplified (and all channels fast outputs are summed up)
- 4 channels (each row) std outputs summed up, then amplified (4 amplifiers) and the four outgoing signals are summed up (and all channels fast outputs are summed up).
The other two are for a "prelimary" $3\times$ 1 matrix of SiPM arrays (3 rows, 1 column) (see Fig.5.41):
- All channels std outputs summed up and amplified for each SiPM array (3 amplifiers) and then the three outgoing signals are summed up (and all channels fast outputs are summed up then driven to the transformer for each SiPM array)
- 4 channels (each row) std outputs summed up, then amplified (12 amplifiers) and the twelve outgoing signals are summed up (and 8 channels fast outputs for each SiPM array are summed up then driven to the transformer).

W.Foreman and I have designed the PCB Miniboards with these readout layouts for the SiPM Arrays using the ExpressPCB Software [78]. The Miniboards have been produced and the components have been mounted on them. In Fig.5.42 and Fig.5.43 the ultimated Miniboards are shown.

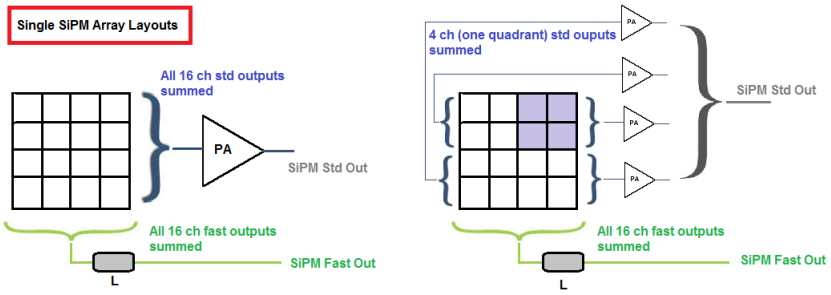

Figure 5.40: Single SiPM Array readout configurations.

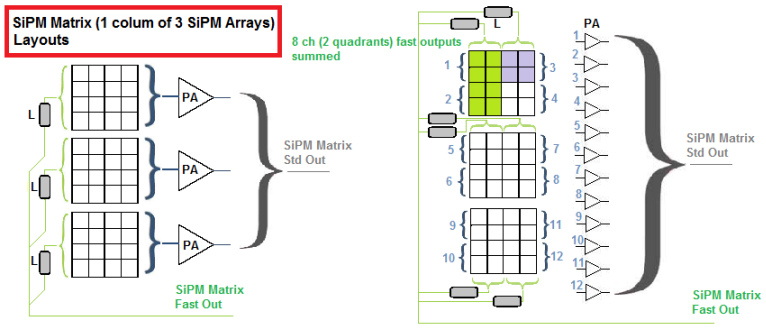

Figure 5.41: 3 × 1 Matrices of SiPM Arrays readout configurations.

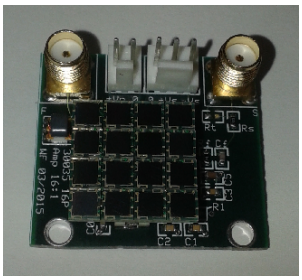

Figure 5.42: Ultimated Single SensL Array C-series readout Miniboard.

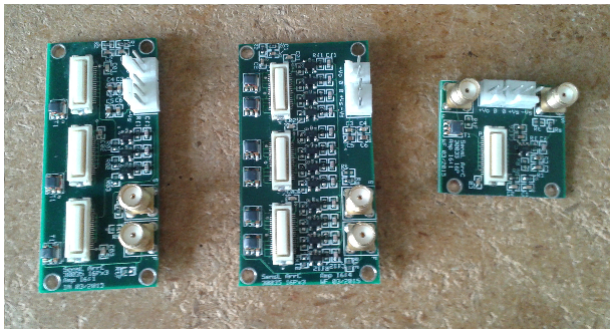

Figure 5.43: The other three ultimated SensL Array C-series Miniboards. The one at right would host a Single Array. The other two would host three SensL Arrays each one (3 × 1 matrix).

5.3.2 Next step: cold tests with a Cryocooler

The plan for the upcoming summer would be to test these boards at cryogenic temperatures.
The boards will be set in a Cryocooler, that could make us test them at several temperatures in vacuum, and then they will be lightened by a pulsed blue LED, driven from outside to inside the cryostat through an optical fiber. In Fig.5.3.2 there is a schematic representation of the experimental setup we planned for the SiPM boards cold tests and in Fig.5.3.2 there is a picture of the cold tests experimental stand we have settled up already in the laboratory.

Our aim is to characterize the SiPM Arrays/Matrices response at cold temperatures (time features, single photoelectron calibration, signal to noise ratio...).
The "preliminary" measurements that are planned to be made in the summer are:

- Breakdown voltage temperature dependence,
- Dark state characterization (SiPM not lightened) at several temperatures,
- Crosstalk and Afterpulse on the SiPM signal (without preamplification stage) at different V_{bias} for fixed temperatures, e.g LAr temperature,
- SiPM single photoelectron response with and without powering on the preamplification stage at several temperatures, especially LAr temperature 90 K $\rightarrow$ Gain vs T, Gain vs V_{bias},
- Timing performances of the different readout configurations at several V_{bias},

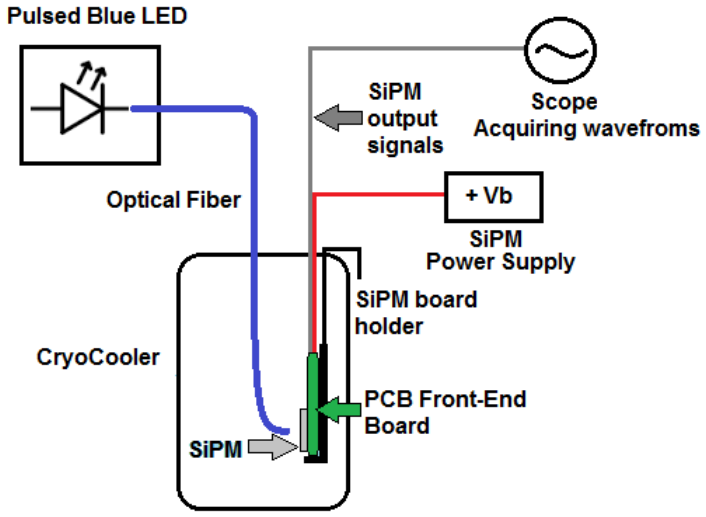

Figure 5.44: Cold tests setup for the SiPM Arrays Miniboards: a schematic view.

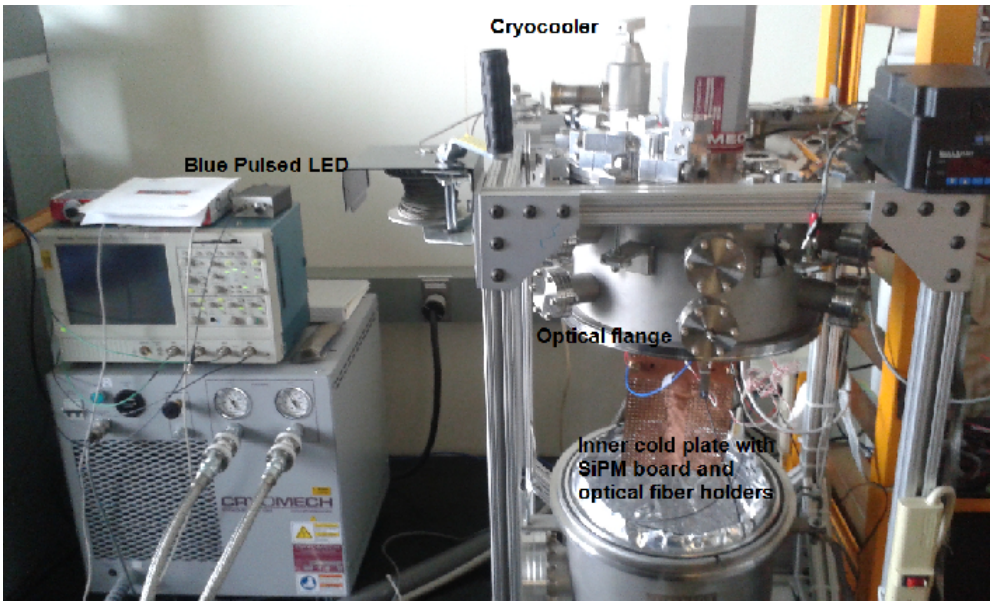

Figure 5.45: Cold tests setup for the SiPM Arrays Miniboards: the test stand in WH14.

Summary:
The results of this project and studies for SiPM dedicated cold electronics to collect LAr scintillation signals in the TPC can be here summarized:

- We designed and produced three front-end readout boards for two Hamamatsu SiPM Arrays (MPPC Array S11828-3344M) and one single channel SensL SiPM (MicroFB 60035). We tested them coupled to a plastic scintillator at room temperature (300 K) on cosmic signals. Then we did a few tests in Liquid Nitrogen (77 K) to see firstly the reliability of our custom designed cold front-end electroincs and we did a preliminary gain characterization of one of the boards, the SensL SiPM board. The three SiPM boards were deployed in LAr (90 K) inside LArIAT TPC cryostat.

- As soon as LArIAT experiment has been fully operational, by the end of April 2015, we planned a characterization of the three SiPM boards response to LAr scintillation light and a comparison with the PMTs results. A preliminary study has been done for the SensL board, for direct signals and preamplified signals of cosmic muons crossing the TPC LAr active volume.

- The ongoing development for LArIAT 2nd Run involving light collection and especially SiPMs is related to the possibility to make SiPM matrices that could cover the same area as a PMT photocathode. Four cold-readout boards have been designed and produced, for SensL SiPM single Arrays and Matrices too. Tests of these boards in a cryocooler with a pulsed LED, to characterize signal time and noise features and device gain are planned for this upcoming summer.

Conclusions

LArIAT experiment is part of LArTPC program for Neutrino Physics at Fermilab. The main goal is the optimization of the offline algorithms for Particle IDentification and calorimetric reconstruction for Liquid Argon detector technology, both TPC wires signals and LAr scintillation light collection. LArIAT experiment aims to measure the main properties of charged particles interactions in LAr in an energy range (0.2 - 2.0 GeV) comparable with the energy spectrum of the same particles when produced in a (ν,Ar) interaction, for neutrino energies E_ν of few GeV, typical of the SBN and LBN programs. The TestBeam provides a controlled environment to produce and select particles of several species, momentum and charge (mainly pions $\pi^\pm$, protons p, muons $\mu^\pm$, electrons $e^\pm$, kaons $K^\pm$...). It is possible to develop and validate the off-line software analysis tools for TPC signals for PID (Particle IDentification), calorimetric measurements and 2-D and 3-D event reconstruction without relying solely on simulations. The LArIAT experiment is actually running at the Fermilab TestBeam Facility and the 1st Run, with data acquisition for the TPC, lasted from 30th April 2015 to 4th July 2015.

During my stay in Fermilab I have worked on the two main topics of my Thesis: a MC study of pion interactions in LAr and a subsequent application on real reconstructed data and an hardware oriented task, i.e. the development of dedicated front-end electronics for SiPMs in LAr. Meanwhile I have been actively involved in the commissioning of the TPC and the auxiliary detectors. Moreover I have been involved in preliminary analysis and hardware improvement for the raw data collection during the first weeks of the Run: ToF studies, Trigger conditions, Light collection system noise studies...

Charged pions $\pi^\pm$ are produced in a noticeable number in (ν, Ar) interactions for neutrino energies of few GeV and this is the reason why they have been chosen as one of the main components of the charged particle TestBeam for LArIAT experiment.
The study of charged pion interactions in Ar has been the main topic of my Thesis, a software oriented task.
I worked on a MC simulation of charged pion interactions in Liquid Argon target and on the development of a routine to evaluate the total interaction cross section that could be later applied to real data.

A prediction of the total hadronic interaction (π,Ar) cross section dependence on the kinetic energy of the pion has been produced from "thin target" simulations with two different MC generators (Geant4 and Genie). I compared the MC predictions for LAr and other targets with the available cross section experimental data in two different energy regions (in the Delta resonance region, 130 MeV-150 MeV, and at 900 MeV pion kinetic energy). It appears the two MC generators pretty well reproduce the π total and reaction cross section at high energy and for several targets, while they give slightly different predictions for the total cross section in the Delta resonance region, probably they simulation models for elastic interactions need to be tuned better.

The LArIAT TPC active volume consists however in a "thick target" for charged pion interactions. To estimate the charged pion cross section on Ar from the experimental data acquired in LArIAT, we developed a new offline analysis method, the "Sliced TPC" approach, that makes use of the fine granularity and of the high resolution (spatial and calorimetric) of the LArTPC. We did a comparison at MC simulation level between ($\pi^\pm$, Ar) cross section results in a thin target and in a thick target, the last treated

with the method previously described. The comparison has validated the "Sliced TPC" method for a high accuracy and statistical precision measurement of the ($\pi^{\pm}$, Ar) cross section with the LArTPC acquired data in LArIAT experiment.

Next step will be applying the "Sliced TPC" approach to reconstructed tracks from LArIAT TPC acquired data to get out an evaluation of charged pion-Ar nucleus cross section. Since we have ended the LArIAT 1st Run in the first days of July 2015, the analysis is actually in progress. The offline event reconstruction and analysis runs in LArIATSoft environment; there is a huge effort of all the collaboration to have each step of the reconstruction working properly, from the beamline auxiliary detectors beam track reconstruction, with PID and incident momentum measurement, as well as the TPC events reconstruction and eventually the matching between these two informations for a complete characterization of each beam particle that goes through the TPC LAr volume. I have worked in the development and test of the reconstruction chain for events in the TPC, from LArSoft modules. At this very moment the TPC reconstruction chain is producing 3-D tracks for crossing particles and particles that experience an elastic and inelastic scattering; the shower reconstruction code need to be ported in our framework, as well as the modules for 3-D interaction vertex finding and the modules for the calorimetric reconstruction along each track need to be adapted for out LArTPC readout configuration. As soon as we will have all the reconstruction steps working properly, we could apply the "Sliced TPC" approach to real reconstructed tracks, with the energy deposit information from calorimetry and the point of interaction from the vertex finders, to calculate the total hadronic interaction cross section for charged pions in LAr (systematic errors need to be estimated).

In addition to the collection of the ionization charge from the TPC, the detection of the scintillation light produced in LAr is an actual point of interest, both for its trigger function for TPC events collection and for the possibility to use also this information to improve the energy resolution of this detector technology. LAr scintillation light wavelength is in the VUV region (128 nm), so it's necessary to use wavelength shifters, since the prevalent light detectors are sensitive to optical photons; in LArIAT each side of the TPC is covered with TPB coated foils, which shifts the light scintillation wavelength to blue photons (428 nm). Actually two different light collection systems have been implemented in LArIAT cryostat, two PMTs and three SiPM readout boards.

The development and test of cold front-end electronics for SiPM devices that have been deployed in the TPC cryostat to collect LAr scintillation light has been the second topic of my Thesis, a hardware oriented task.
We have designed, produced and tested (at room temperature 300 K and in LN_2 77 K) three different preamplification boards with dedicated cold electronics for two Hamamatsu SiPM Arrays and one single channel SensL SiPM. Then we have mounted them on the cryostat optical flange and deployed in LAr behind the TPC wire planes.
I have made a preliminary characterization of the SensL SiPM response to LAr scintillation light with and without the preamplification stage active on the board. The shape of SensL direct response to LAr scintillation light keeps memory in its rising edge of the scintillation light distribution, convoluted with the light collection time spread. The preamplified signal is higher in amplitude and faster; it reproduces multiple and single photoelectron pulses. The average waveform for signals collected with similar trigger conditions (e.g. cosmic trigger) has a shape comparable with the scintillation time distribution and its area corresponds to the average number of photoelectrons that are collected by the SiPM for that trigger. Studying the single photoelectrons pulses, due to LAr late light, in the signal's tails we had a preliminary estimate of the SensL

gain in LAr for a fixed bias voltage, which was consistent with the results obtained in LN_2 for the same voltage. A more complete characterization of all the three SiPMs response in LAr and the comparison with PMTs results is planned for this summer.

Moreover the ongoing development for light collection for LArIAT 2nd Run is related to the possibility to make SiPM matrices that could cover the same area as a PMT photocathode. I have been involved in the design and production of four cold-readout boards for SensL SiPM Arrays. Tests and characterization of the response of these boards in cryogenics are planned for this upcoming summer.

Acknowledgements

I take this opportunity to express gratitude to my supervisor Dott. Flavio Cavanna for sharing expertise, and sincere and valuable guidance.
I am also grateful to Dott. Oscar Adriani who supported and encouraged me during each step of this thesis experience abroad.

I wish to express my sincere gratitude to Fermilab Institution, for hosting me for this thesis experience. My sincere thanks go to the Neutrino Division, especially Regina Rameika and Steve Brice, and the Technical Division, especially Emanuela Barzi, for providing me with all the necessary facilities for the research and for the stay in Fermilab, Us.
I also place on record a thank you to Università degli Studi di Firenze, which gives the students the opportunity to be involved in thesis projects in international collaborations abroad.

I place on record, my sincere thank you to the LArIAT collaboration especially, for trusting young students, like me, giving them the opportunity to be an active part of the experiment and making them feel a completing part of the collaboration.
I am grateful to Jen Raaf and Brian Rebel, who are LArIAT experiment spokespeople together with Flavio; they gave me support and attention during the whole period of the thesis.
I am also grateful to Hans Wenzel for his help and the time he spent with me working on Geant4 simulations.
I want to place a special thank you to the "light collection group", Will Fo., Pawel and Andrzej, I've worked with in designing the SiPM readout boards and making our preliminary studies of the response of these devices in cryogenic environment.
I also thank Roberto, Jonathan and Tingjun for their help and their suggestions in doing my first steps in LArSoft framework and being an independent developer of the code needed for the analysis of the LArIAT TPC data.
I would like to express sincere thanks to Jason and Johnny, that have been always very willing to give support about data acquisition, lend a hand for our tests in the beamline and have always a word to make you laugh.
There are many more people I want to thank: Ornella, Will Fla., Elena, Ryan, Flor .... I really had a great experience working with all of the "LArIATers". I would like to thank all of them for their help, their suggestions and the time spent with me in Wilson Hall offices and at the TestBeam.
I place on record, my thank you to Steve Dytman, for his help on pion studies and Genie predictions, to the people from MicroBooNE experiment, as Bruce Baller for the time spent in helping me to understand the reconstruction chain in LArSoft framework, and to the technicians, as Albert Dyer, who gave me suggestions and help during my thesis project, especially with the SiPM assembling and tests.
I wish to express a thank you to Giorgio Bellettini and Simone Donati, that supported me for coming back here for my thesis after the Summer Student experience I had last year. Moreover I want to thank to all the people from Fermilab that worked for providing me the accomodation and the facilities from my stay in Fermilab, Us.

I want to thank the very nice guys I met here in Fermilab and here around that have shortly become good friends of mine. Thanks to Marco, Cecilia, Luigi and Omar who have been like a funny weird family for me here. Thanks to Giulia, Margherita, Giuseppe, Diana and all the other nice people I met and I spent time with.

I want to state that I am extremely grateful to my parents, Andrea and Tiziana, for the unceasing encouragement and support through this venture. Even if we were more than 7000 km far from each other, they manage to "give me energy" to keep going doing my best during this thesis period in the US. I want to thank my sisters, Noemi and Olivia, that trusted me and support my effort in pursuing my thesis goal in a place so far from them; they also managed to steal me a sunrise, a laugh, when we had our calls. I am grateful to all of my family too, my grandparents (Augusto and Giulietta and the ones that I know are looking at me and giving me protection from the bright stars in the sky, Gemma and Vasco), my aunts Cristina and Vanna, my uncle Enrico and all the close relatives that strongly supported my choice to come to the Us, Fermilab, for my thesis project because they all thought it was a great possibility to challenge myself as a physics student and as a person.

I want to thank all my friend at home, that cheered for me and always make me laugh when we had our "Skype conference calls"; thanks to Jessica, Alessandro, Selene, Marco, Valentina, Samira, Giulia, Alessia, Maria, Niccolò, Marco L. and all of them. Thanks also to my "poletto" friends that always kept me updated on the news of the Polo Scientifico's life and shared with me worries and expectations for our thesis projects and our future PhD studies: Giulia F., Rita, Jacopo, Miriam, Klejdja, Giacomo, Lorenzo L., Lorenzo F., Giulia A. and all of them. I want to thank Alessio, Alfredo and Marco, from our "beware of σ_{rr}" group that supported me, especially the first months when I had to deal with the terrible snowy and freezy cold in the Us.

I also place on record, my sense of gratitude to one and all, who directly or indirectly, have lent their hand in this venture.

Bibliography

[1] W.Pauli, *Open letter to the group of radioactive people at the Gauverein meeting in Tübingen.*; Zürich, Dec.4, 1930

[2] F.L.Wilson, *Fermi's Theory of Beta Decay*, American Journal of Physics Vol.36 Num.12; December 1968

[3] C. L Cowan Jr., F. Reines, F. B. Harrison, H. W. Kruse, A. D McGuire ,*Detection of the Free Neutrino: a Confirmation*, Science 124 (3212) pp 103–104; July 20, 1956

[4] G. Danby, J-M. Gaillard, K Goulianos, L. M. Lederman, N. Mistry, M. Schwartz and Z. Steinbergert, *Observation of high-energy neutrino reactions and the existence of two kinds of neutrinos*, Phys.Rev.Letters Vol.9 Num.1; July1, 1962

[5] DONUT collaboration , *Observation of tau neutrino interactions*, Physics Letters B 504 pp 218–224; January 2001

[6] The MINOS Experiment and NuMI Beamline, http://www-numi.fnal.gov/index.html

[7] The DUNE Experiment and LBNF Beamline, http://www.dunescience.org/

[8] D.A.Harris, *Oscillation Measurements with Calorimeters: Why Does NuINT Matter?*, Nuclear Physics B (Proc.Suppl) Vol.139 pp.33-38; 2005

[9] BooNE, Booster Neutrino Experiment, http://www-boone.fnal.gov/

[10] B.Z.Hu on behalf of the Daya Bay collaboration, *Recent Results from Daya Bay Reactor Neutrino Experiment*, Moriond 2015 EW session; 14 May 2015

[11] *Evidence for Neutrino Oscillations from the LSND Experiment* ,http://www.aps.org/units/dnp/research/lsnd.cfm

[12] F.Cavanna, *NuInt: Neutrino Interactions in the Intermediate energy range*, Nuclear Physics B (Proc. Suppl.) Vol.139 pp 9–1; 2005

[13] K.Jaeger, *Performance of the Argonne 12-Foot Bubble Chamber*, Argonne National Laboratory; March 1974

[14] C.Rubbia, *The Liquid-Argon Time Projection Chamber: a new concept for neutrino detectors*, CERN EP Internal Report 77-8; 16 May 1977

[15] D.R.Nygren *The Time Projection Chamber- A new 4π detector for charged particles*, PEP 144; 1976

[16] W.R.Leo *Techniques for Nuclear and Particle Physics Experiments*, Springer-Verlag, 2nd Revised Ed. 1994

[17] ICARUS Collaboration, *ICARUS: a proposal for the Gran Sasso Laboratory*, INFN/AE-85/7 (1985) and following publications (http://icarus.lngs.infn.it/)

[18] A.Bettini et al., *The ICARUS liquid argon TPC: a complete imaging device for particle physics*, Nucl. Instrum. Methods in Physics Research A Vol.315 pp 223-228; 1992

[19] ICARUS, Imaging Cosmic And Rare Underground Signals, http://icarus.lngs.infn.it/index.php

[20] F.Arneodo et al., *Performance of the 10 m^3 ICARUS liquid argon prototype*, Nucl. Instrum. Methods in Physics Research A Vol.498 pp 292–311; 2003

[21] F.Cavanna, *L'esperimento ICARUS*, L'Italia al CERN, INFN - LNF; 1995

[22] A.Ereditato and A.Rubbia, *Ideas for future liquid Argon detectors*, Nuclear Physics B (Proc. Suppl.) Vol.139 pp 301-310; 2005

[23] ArgoNeuT: Mini LArTPC Exposure to Fermilab's NuMI Beam ,http://t962.fnal.gov/

[24] C.Anderson et al., *The ArgoNeuT detector in the NuMI low-energy beam line at Fermilab*, JINST 7 P10019; October 2012

[25] ArgoNeuT collaboration, R.Acciarri et al., *First Measurement of Neutrino and Antineutrino Coherent Charged Pion Production on Argon*, Phys. Rev. Lett. 113; August 2014

[26] MicroBooNE collaboration, H.Chen et al., *Proposal for a new experiment using the booster and NuMI neutrino beamlines: MicroBooNE*, Fermilab Proposal-0974, Fermilab; 2007

[27] MicroBoone Experiment, http://www-microboone.fnal.gov/

[28] M.Antonello, F.Arneodo, A.Bueno, F.Cavanna, D.Garcìa-Gàmez, S.Navas-Concha, O.Palamara, G.Piano Mortari, E.Segreto, *Analysis of Liquid Argon Scintillation Light Signals with the ICARUS T600 Detector*, ICARUS-TM/06-03; July 2006

[29] *LArIAT FNAL website*, http://lariat.fnal.gov/index.html

[30] F. Cavanna, M. Kordosky, J. Raaf, B. Rebel and LArIAT collaboration, *LArIAT: Liquid Argon In A Testbeam*; June 2014

[31] *LArIAT/T-1034: Liquid Argon TPC In A Test beam, TSW - Technical Scope of Work for the 2013 FERMILAB Test Beam Facility Program*; February 2013.

[32] *FTBF*, http://www-ppd.fnal.gov/FTBF/

[33] A.M. Szelc, *The LArIAT light readout system*; September 2013

[34] LArIAT Collaboration, *Results from Scintillation Light Detection Test at University of Chicago*; April 2014

[35] WArP Collaboration, R.Acciarri et a., *Demonstration and Comparison of Operation of Photomultiplier Tubes at Liquid Argon Temperature*, Journal of Instrumentation 7 P01016; 26 Sep 2011

[36] Hamamatsu Photonis, R11065 data sheets (2009)

[37] Electron Tube, ETL-D750 data sheets (2006)

[38] LArIAT Online Wiki, https://redmine.fnal.gov/redmine/projects/lariat-online/wiki

[39] CAEN V1495 board, datasheet

[40] CAEN V1751 Waveform digitizer, datasheet

[41] T.Ericson ans W.Weise, *Pions and Nuclei*, Oxford University Press,1988

[42] G.L.Shaw, *Pion-Nucleon Scattering*, John Wiley and Sons - Interscience, 1969

[43] T.S.H.Lee et R.P.Redwine, *Pion-Nucleus Interactions*, Annual Review of Nuclear and Particle Science Vol.53, pp 23-63; 2002

[44] A.S.Clough et al., *Pion-nucleus total cross sections from 88 to 860 MeV*, Nuclear Physics B76, pp 15-28; March 1974

[45] A.S.Carrol et al., *Pion-nucleus total cross sections in the (3,3) resonance region*, Phys.Rev. C Vol.14 Num.2, pp 635-638 ; August 1976

[46] D.Ashery, *Pion nucleus reactions*, Nuclear Physics A354 pp555c-576c; 1981

[47] D.Ashery et al., *True absorption and scattering of pions on nuclei*, Phys.Rev. C Vol.23 Num.5; May 1981

[48] B.W.Allardyce et al., *Pion reaction cross sections and nuclear sizes*, Nuclear Physics A209 pp 1-51; March 1973

[49] L.M.Saunders, *Electromagnetic production of pions from nuclei*, Nuclear Physics B7 pp 293-310; Febrary 1968

[50] R.D.Ransome, *Pion Absorption and Re-Scattering*, Nuclear Physics B (Proc. Suppl.) Vol.139 pp 208–212; February 2005

[51] B.Kotlinski et al., *Pion absorption reactions on N,Ar and Xe*, Eur. Phys. J. A9 pp 537-552; October 2000

[52] P.W.Hewson, *Charge exchange in nuclei following pion inelastic scattering*, Nuclear Physics A133 pp 659-672; January 1969

[53] *Particle Data Book*, Ch.27 "Passage of particles through matter", Revised January 2012 by H. Bichsel, D.E. Groom and S.R. Klein

[54] *Geant4*, http://geant4.cern.ch/

[55] S.Agostinelli (GEANT4 Collaboration), *Geant4 - a simulation toolkit*, Nucl. Instrum. Methods A 506 (2003) pp 250-303

[56] J.Allison (GEANT4 Collaboration), *Geant4 developments and applications*, IEEE Trans. Nucl. Sci. 53 No. 1 (2006) pp 270-278

[57] *Root - An Object Oriented Data Analysis Framework*, https://root.cern.ch/

[58] Geant4 Validation database, http://g4validation.fnal.gov:8080/G4WebAppNG

[59] A.Heikkinen, N.Stepanov, J.P.Wellisch, *Bertini intra-nuclear cascade implementation in Geant4*, Computing in High Energy and Nuclear Physics, pp 24-28; March 2003

[60] D.H.Wright, M.H.Kelsey, *The Geant4 Bertini Cascade*, SLAC

[61] Geant4 MaterialDatabase, http://geant4.cern.ch/UserDocumentation/UsersGuides/ForApplicationDeveloper/html/apas08.html

[62] *GENIE Neutrino Monte Carlo Generator*, http://www.genie-mc.org/

[63] *art: A Framework For New, Small Experiments at Fermilab*, http://mu2e-docdb.fnal.gov/

[64] Liquid Argon Software (LArSoft) project, https://cdcvs.fnal.gov/redmine/projects/larsoft/wiki

[65] LArIAT offline software, https://cdcvs.fnal.gov/redmine/projects/lardbt/wiki#Offline-Software-Analysis

[66] G.Collazuol, *The SiPM Physics and Technology- a Review* , LAL Orsay, June 2012

[67] A.Para, *Silicon PM's: Novel Photodetectors*, Fermilab; June 2014

[68] S.S. Piatek, *Physics and Operation of an MPPC*, Hamamatsu Corporation & New Jersey Institute of Technology; February 2014

[69] G.Collazuol, *SiPM behavior at low temperatures*, IPRD 2010 Siena; June 2010

[70] S.E.Walker, B.Rossi, G.Fiorillo, *Cryogenic Testing of SiPM's*, Darwin Conference; January 2015

[71] S.E.Walker, *Temperature Dependence of Resistance and Breakdown Voltage For Silicon Photomultipliers (SiPM)*, GSSI Presentation

[72] N. Dinu, C. Bazin., V. Chaumat, et. al., *Temperature and Bias Voltage Dependence of the MPPC Detectors*, IEEE Nucl.Sci. Symp. Conference Record; 2010

[73] *Hamamatsu MPPC modules, Technical Information*

[74] N.Canci et al., *Liquid Argon Scintillation Read-out with Silicon Devices*, LIDINE 2013 Conference - LIght Detection In Noble Elements, Fermilab

[75] D. Whittington and S. Mufson, *Scintillation Light from Cosmic-Ray Muons in Liquid Argon*, Indiana University; July 2014

[76] *Hamamatsu Monolithic MPPC array in SMD package, S11828-3344M*, datasheet

[77] *SensL Single Channel MicroFB 60035*, datasheet

[78] *ExpressPCB Software*, http://www.expresspcb.com/index.htm

[79] *BGA 616, Silicon Germanium Broadband MMIC Amplifier*, Infineon Technologies; datasheet (2011)

[80] *ADA4891-1, Low Cost CMOS, High Speed, Rail-to-Rail Amplifier*, Analog Devices; datasheet (2013)

[81] J.M.Yebras, P.Antoranz,J.M.Miranda, *Optical Engeneering, Strategies for shortening the output pulse of SiPM*, July 2012

[82] *OPA656, Wideband, Unity-Gain Stable, FET-Input Operational Amplifier*, Texas Instruments; datasheet (2008)

[83] E.Segreto, *An analytic technique for the estimation of the light yield of a scintillation detector.*; August 2012

[84] Tektronix Mixed Signal Oscilloscopes DPO5000B Series Datasheet

[85] P.Pereira,S.valtchev et al.,*Power electronics performance in cryogenics environment*; Journal of Physics: Conference Series 97 (2008)

[86] F.Torres,J.Pastrana at al., *Low temperature characterization of CMOS operational amplifier ICs*; 1996

[87] K.Hayashi, K.Saitih et al., *A current to voltage converter for cryogenics using a CMOS operational amplifier*; Journal of Physics: Conference Series 150 (2009)

[88] Short-Baseline Near Detector (SBND), http://sbn-nd.fnal.gov/index.html

[89] *SensL SiPM Arrays*, www.sensl.com/downloads/ds/PB-ArraySMT.pdf

[90] *SensL Array-SMT User Manual*, www.sensl.com/downloads/ds/UM-ArraySMT.pdf

[91] *SensL C-series SiPM User Manual*, www.sensl.com/downloads/ds/UM-MicroC.pdf

[92] *SensL C-series SiPM Datasheet*, www.sensl.com/downloads/ds/DS-MicroCseries.pdf